

EPA-R2-74
January 1975

FLOW ESTABLISHMENT AND INITIAL ENTRAINMENT OF
HEATED WATER SURFACE JETS

by

Heinz Stefan,
Loren Bergstedt,
and
Edward Mroska

St. Anthony Falls Hydraulic Laboratory
University of Minnesota
Minneapolis, Minnesota

Grant R 800 435
Program Element 1BA032

Project Officer:

Mostafa A. Shirazi

Thermal Pollution Branch
Pacific Northwest Environmental Research Laboratory
USEPA, Corvallis, Oregon 97330

Prepared for

OFFICE OF RESEARCH AND MONITORING
U.S. ENVIRONMENTAL PROTECTION AGENCY
Washington, D.C. 20460

ABSTRACT

Mathematical models to predict water temperature distributions resulting from heated water surface discharges usually consider three subregions of the flow field: (a) an outlet region or zone of flow establishment (ZFE), (b) a zone of fully established jet flow, and (c) a far field with mostly passive dispersion. Of these three regions, zone (b) can be treated mathematically most readily using integral techniques; zone (c) requires input specifying mean flow and turbulence of the ambient flow field; and zone (a) depends essentially on the geometry of the outlet and the discharge characteristics in terms of the velocity and temperature of the water.

The results of an experimental study dealing with zone (a) are reported. The discharge channel had a rectangular cross section and led into a deep, wide reservoir. The aspect ratio (width-to-depth ratio) of the channel, the volumetric discharge rate, and the discharge temperature were varied. A cross-flow was imposed in some of the experiments.

The length of the zone of flow establishment, x_0 or s_0 , was measured in terms of mean excess temperature, mean velocity, and turbulence intensity along the trajectory. The length, x_0 or s_0 , was related to channel aspect ratio A , outlet densimetric Froude number F_0 , and cross-flow-to-jet velocity ratio R . Total volumetric flow rates during flow establishment were established as a function of distance along the jet axis and related to A and F_0 . The results are useful either for extension of existing mathematical models of fully developed heated water surface jets or for verification of mathematical models of the zone of flow establishment.

CONTENTS

	<u>Page</u>
Abstract	ii
List of Figures	iv
List of Tables	viii
Acknowledgments	ix
SECTION I -- CONCLUSIONS	1
SECTION II -- RECOMMENDATIONS	6
SECTION III -- INTRODUCTION	7
SECTION IV -- ZONE OF FLOW (RE-)ESTABLISHMENT	9
SECTION V -- EXPERIMENTAL FACILITY AND DATA ACQUISITION	16
Basic Equipment	16
Adaptation of Experimental Facility for Cross-Flow Experiments	22
SECTION VI -- EXPERIMENTAL RESULTS	27
Pilot Studies	27
Main Experiments: Straight Jets	37
Length of Zone of Flow Establishment (ZFE)	37
Photographs of Surface Flow	37
Water Temperature Data	43
Time-Averaged Water Temperatures	43
Fluctuating Water Temperature Components	55
Velocity Data	70
Time-Averaged Velocities	70
Fluctuating Velocity Components	76
Volumetric Flow Rates and Entrainment	76
Main Experiments: Curvilinear Jets	85
Photographs of Flow Features	85
Trajectories	85
Length of Zone of Flow Establishment (ZFE)	87
SECTION VII -- ANALYTICAL EXPRESSIONS FOR ESTABLISHMENT LENGTH AND INITIAL FLOW RATES	101
Length of Zone of Flow Establishment	101
Initial Entrainment for Straight Jets	107
References	110
Resulting Publications	112
Past Publications Relating to the Subject	112
Symbols and Units	113
<u>Appendix A</u> - Isotherms $T = \text{constant}$ and $\delta T = \text{constant}$ in Vertical Sections along Jet Axis or Perpendicular to It, $A = 2.4$, $A = 9.6$, $R = 0$	115
<u>Appendix B</u> - Isotherms $T = \text{constant}$ and $\delta T = \text{constant}$ and Isovels $V = \text{constant}$ in Vertical and Horizontal Sections, $A = 2.4$, $R = 0.41$	132

FIGURES

<u>No.</u>		<u>Page</u>
1a	Schematic showing zone of flow establishment (ZFE) near a surface outlet	10
1b	Streaklines illustrating the surface flow pattern and flow establishment - $A = 1.0$, $R = 0$, $F_o = \infty$, Exposure = $1/5$ sec	11
2	Temperature and velocity distributions at the beginning and end of the zone of flow establishment (schematic)	12
3a	Schematic of experimental tank	17
3b	Schematic diagrams showing evolution of temperature and velocity measuring and recording systems in the course of the investigation	18
4a	Schematic of adaptation of experimental tank for crossflow experiments	23
4b	Experimental tank	25
4c	Crossflow velocity profiles	26
5a	Surface centerline temperature versus axial distance, semicircular outlet, low F_o	28
5b	Surface centerline temperature versus axial distance, semicircular outlet, high F_o	29
6	Definition of zone of flow establishment for non-buoyant, fully submerged jets	31
7	Schematic showing range of alternative values of x_o depending on definition	32
8a	x_o/d_o versus F_o at $T = 0.98, 0.95, 0.90,$ and 0.80 and $A = 2.0$ (semicircular pipe, positive buoyancy)	34
8b	x_o/d_o versus F_o at $T = 0.98$ and visual observations, $A = 2.0$ (semicircular pipe, negative buoyancy)	35
9	Horizontal spreading angle, ϕ_o , of free shear zone recorded photographically	36
10a	Streaklines illustrating surface flow patterns - $A = 1.0$, $R = 0$, Exposure = $1/10$ sec	38

FIGURES

<u>No.</u>		<u>Page</u>
10b	Streaklines illustrating surface flow patterns - $A = 2.4$, $R = 0$, Exposure = $1/5$ sec	39
10c	Streaklines illustrating surface flow patterns - $A = 9.6$, $R = 0$, Exposure = $1/5$ sec at $F = \infty$ and $1/10$ sec at $F = 3.0$	40
11	Boundaries of visible core region for $A = 1.0, 2.4, \text{ and } 9.6$ and various F_0	41
12	x_0/d_0 versus F_0 at $A = 1.0, 2.4, \text{ and } 9.6$ as determined from photographs of surface tracers	42
13	Sample of time-averaged water temperatures along jet axis - $A = 2.4, F_0 = 2.2, 3.8, 3.9, 6.4, \text{ and } 15.8$	44
14a	x_0/d_0 versus F_0 at $T = 0.98, 0.95, 0.90, \text{ and } 0.80$; $A = 1.0, R = 0$	46
14b	x_0/d_0 versus F_0 at $T = 0.98, 0.95, 0.90, \text{ and } 0.80$; $A = 2.4, R = 0$	47
14c	x_0/d_0 versus F_0 at $T = 0.98, 0.95, 0.90, \text{ and } 0.80$; $A = 4.8, R = 0$	48
14d	x_0/d_0 versus F_0 at $T = 0.98, 0.95, 0.90, \text{ and } 0.80$; $A = 9.6, R = 0$	49
15a	x_0/d_0 versus F_0 at $T = 0.85$; $A = 1.0, 2.4, 4.8, \text{ and } 9.6$; and $R = 0$	50
15b	x_0/d_0 versus F_0 at $T = 0.90$; $A = 1.0, 2.4, 4.8, \text{ and } 9.6$; and $R = 0$	51
15c	x_0/d_0 versus F_0 at $T = 0.95$; $A = 1.0, 2.4, 4.8, \text{ and } 9.6$; and $R = 0$	52
16a	δT versus x/d_0 along jet axis at $A = 1.0$ and $R = 0$	57
16b	δT versus x/d_0 along jet axis at $A = 2.4$ and $R = 0$	58
16c	δT versus x/d_0 along jet axis at $A = 4.8$ and $R = 0$	59
16d	δT versus x/d_0 along jet axis at $A = 9.6$ and $R = 0$	60

FIGURES

<u>No.</u>		<u>Page</u>
17a	x_o/d_o versus F_o at $\delta T = 0.02$; $A = 1.0, 2.4, 4.8,$ and 9.6 ; and $R = 0$	62
17b	x_o/d_o versus F_o at $\delta T = 0.04$; $A = 1.0, 2.4, 4.8,$ and 9.6 ; and $R = 0$	63
18a	δT versus y/d_o perpendicular to jet axis at $A = 1.0,$ $x/d_o = 1.7,$ $R = 0,$ and $F_o = 2.2, 3.5,$ and 6.5	65
18b	δT versus y/d_o perpendicular to jet axis at $A = 1.0,$ $x/d_o = 3.5,$ $R = 0,$ and $F_o = 2.2, 3.5,$ and 6.5	66
18c	δT versus y/d_o perpendicular to jet axis at $A = 2.4,$ $x/d_o = 2,$ $R = 0,$ and $F_o = 2.2, 3.8,$ and 15.8	67
18d	δT versus y/d_o perpendicular to jet axis at $A = 9.6,$ $x/d_o = 2,$ $R = 0,$ and $F_o = 2.1$ and 4.1	68
19	Spreading angle and width of free shear zone at $\delta T = 0.01$ and 0.02 for $A = 1.0, 2.4,$ and 9.6 ; $x/d_o = 2$ and $R = 0$..	69
20a	x_o/d_o versus F_o at $V = 0.95, 0.90,$ and 0.80 ; $A = 1.0$; and $R = 0$	71
20b	x_o/d_o versus F_o at $V = 0.95, 0.90,$ and 0.80 ; $A = 4.8$; and $R = 0$	72
20c	x_o/d_o versus F_o at $V = 0.98, 0.95, 0.90,$ and 0.80 ; $A = 9.6$; and $R = 0$	73
21	x_o/d_o versus F_o at $V = 0.9$; $A = 1.0, 4.8,$ and 9.6 ; and $R = 0$	74
22a	x_o/d_o versus F_o at $\delta V = 0.05, 0.075,$ and 0.10 ; $A = 1.0$; and $R = 0$	77
22b	x_o/d_o versus F_o at $\delta V = 0.075$ and $0.10,$ $A = 4.8,$ and $R = 0$	78
23a	Q/Q_o versus x/d_o at $A = 1.0$ and $R = 0$	79
23b	Q/Q_o versus x/d_o at $A = 4.8$ and $R = 0$	80
23c	Q/Q_o versus x/d_o at $A = 9.6$ and $R = 0$	81

FIGURES

<u>No.</u>		<u>Page</u>
24	Q/Q_0 versus x/d_0 for fully submerged, non-buoyant two- and three-dimensional jets	82
25	Q/Q_0 versus A at $F_0 = 1.8$, $F_0 = 3.4$, and $F_0 \rightarrow 0$; $x/d_0 = 10$; and $R = 0$	83
26	Photograph of vortex formation near the outlet at $A = 2.4$, $F_0 = 3.46$, and $R = 0$	84
27	Photographs of discharge into a crossflow at $A = 2.4$, $R = 0.41$, and $F_0 = 25.4$ and 2.8	86
28	Typical centerline plume trajectory at $A = 4.8$, $R = 0.41$, and $F_0 = 3.25$	88
29a	Plume trajectory at $A = 1.0$, $R = 0.41$, and $F_0 = 3.2$ and ∞	89
29b	Plume trajectory at $A = 2.4$, $R = 0.41$, and $F_0 = 3.2$ and ∞	90
29c	Plume trajectory at $A = 4.8$, $R = 0.41$, and $F_0 = 3.2$ and ∞	91
30a	Observed trajectories, $A = 1.0, 2.4$, and 4.8 ; $F_0 = 3.3$ and ∞ ; and $R = 0.41$	92
30b	Trajectories based on maximum velocity, $A = 1.0, 2.4$, and 4.8 ; $F_0 = 3.3$ and ∞ ; and $R = 0.41$	93
31	s_0/d_0 versus A at $F_0 = 3.2$, $R = 0.41$, and $T = 0.95$, $0.90, 0.85, 0.80, 0.70$, and 0.60	95
32	s_0/d_0 versus A at $F_0 = 3.2$, $R = 0.41$, and $\delta T = 0.02$, $0.03, 0.05, 0.07$, and 0.10	96
33a	s_0/d_0 versus A at $F_0 = 3.2$, $R = 0.41$, and $V = 0.90$, $0.85, 0.80, 0.70$, and 0.60	97
33b	s_0/d_0 versus A at $F_0 = \infty$, $R = 0.41$, and $V = 0.90$, $0.85, 0.80, 0.70$, and 0.60 \.....	98
34	Photograph of dye patterns near the outlet of a discharge into a crossflow - $A = 2.4$, $F_0 = \infty$, $R = 0.41$	100
35	n Versus K	105
36	γ Versus T	106

TABLES

<u>No.</u>		<u>Page</u>
1	Standard Deviations of x_o/w_o and x_o/d_o as given in Figs. 14a, b, and d	53
2	Establishment Lengths x_o for Non-Buoyant, Fully Submerged Jets	54
3	Comparison of Computed and Measured x_o/d_o Values	54
4	Equivalent Values of T and δT	61
5	Ratios of x_o Values, $(x_o)_{temp} / (x_o)_{vel}$, derived from Temperature and Velocity	73

ACKNOWLEDGMENTS

Besides the authors, a number of research assistants and personnel of the St. Anthony Falls Hydraulic Laboratory participated in this study. The contribution, in the early phases of the experiments, made by Manousos Katsoulis (now with the Minnesota Pollution Control Agency) and the assistance provided by C. Shanmugham in the reducing and plotting of the data are acknowledged. Dr. J. M. Killen and J. Ferguson provided very essential help in the development and construction of the data acquisition systems. Shop help was provided by J. Vandenberg and F. Thomas under the supervision of F. Dressel. The manuscript was prepared for publication by Shirley Kii, editorial assistant. The authors wish to express their gratitude to all these people.

Dr. Mostafa A. Shirazi of the Thermal Pollution Branch, Pacific Northwest Environmental Research Laboratory, acted as Project Officer. His input was helpful in orienting the study toward those goals which seemed most appropriate and timely. The authors are also indebted to him for his review of the manuscript of the report.

SECTION I

CONCLUSIONS

1. Mathematical modeling of the zone of flow (re-)establishment (ZFE) of heated water surface jets has been found to be difficult because of the complex dependence on outlet geometry, discharge velocity, buoyancy, and ambient currents. Laboratory experiments have therefore been conducted to provide more observations and data on flow patterns, temperatures, and flow velocities in the ZFE and some distance beyond. From this information, relationships giving the length x_0 of the ZFE, the volumetric flow rates $Q(x)$ versus distance, and the initial spreading angle ϕ_0 have been derived. The independent variables were outlet aspect ratio A , outlet densimetric Froude number, and crossflow ratio R . The relationships provided can be used to improve water temperature predictions in the vicinity of heated water surface outlets.
2. In water temperature modeling, the length, x_0 or s_0 , of the zone of flow establishment of heated water surface jets--also called the outlet zone, core region, or zone of flow re-establishment--can be defined in several different ways.
 - a. One can arbitrarily decide that the ZFE terminates where the time-averaged surface temperature on the jet axis reaches a certain magnitude relative to the outlet temperature.
 - b. On a log-log plot of axial surface temperature versus distance one can extrapolate backwards from the fully established flow data to the outlet temperature level line to define x_0 . For buoyant surface jets the procedure is not easily applicable, because the data do not plot on a straight line.
 - c. One can arbitrarily decide that the ZFE terminates where significant changes in turbulence intensity of temperature or velocity occur along the jet axis.

Depending on the definition used, the value of x_0 varies significantly, as is shown schematically in Fig. 7. It is the authors' judgment that the 90 per cent level of time-averaged water temperatures

measured along the centerline trajectory of the jet represents an acceptable and realistic choice for the length of the ZFE, designated in this report by x_o for straight jets and by s_o for curvilinear jets. However, results at the 80, 95, and 98 per cent levels will also be reported for comparison.

3. Actually, four different flow regions characterize the zone of flow establishment. Going downstream, using water temperature (flow velocity) on the axis (main trajectory) of the surface jet as an indicator, the four regions are

- a. The channel region (prior to discharge), characterized by completely uniform water temperatures and usually a fully developed velocity profile.
- b. The core region just beyond the end of the channel, characterized by constant water temperatures and velocities with time (no fluctuating components) along the jet axis.
- c. The turbulent transition region, in which water temperatures or velocities fluctuate intermittently, but turbulent shear layers growing from the outer edge of the jet have not yet completely penetrated each other.
- d. The fully developed jet region, which is characterized by the internally fully developed turbulence field, resulting in the similarity of temperature and velocity distributions in cross sections perpendicular to the jet axis.

The lengths of regions (b) and (c) are not the same in terms of temperature or velocity, because mass and momentum are transported differently in the shear layers. Practical definitions of the length of the ZFE usually incorporate (b) plus a portion of (c).

4. The dependence of x_o/d_o or s_o/d_o on the independent variables A (= aspect ratio of the rectangular discharge channel), F_o (= outlet densimetric Froude number), and R (= crossflow velocity ratio) has been investigated. Of the parameters A , F_o , and R , the aspect ratio A has the largest influence. It was found, from data obtained for $A = 1$, $A = 2.4$, $A = 4.8$, and $A = 9.6$, that for

straight jets ($R = 0$) the relationship

$$\frac{s_o}{d_o} = K A^n$$

with $n = 0.46$ and $K = 6.0$ gives a first estimate of s_o/d_o at the 90 per cent level of time-averaged temperature concentration. The accuracy is on the order of ± 25 per cent.

A significant deviation from the relationship given above was found for $A = 2.4$. This is attributed to a secondary motion when the aspect ratio is favorable (i.e., near 2). However, the aspect ratio is not a sufficient indicator for such secondary motion. A semi-circular outlet channel ($A = 2.0$) did not show the same effect as a rectangular one ($A = 2.4$) (see Figs. 8a and 14b). Many prototype channels are designed with an aspect ratio near 2, and the question therefore deserves further attention.

5. The values of K and n in the above equation actually depend on the temperature level T at which s_o/d_o is defined. For $1.0 \leq T \leq 0.8$ a second approximation equation was found by non-linear curve-fitting. It is of the form

$$\frac{s_o}{d_o} = (16.0 - 12.8 T)^{1.2} A^{(0.85 - 0.44T)}$$

A further refinement and extension of the equation includes the dependency of s_o/d_o on R . Values of R examined experimentally were $R = 0$ and $R = 0.41$. The s_o/d_o values were found to be approximately 1.4 times larger for the straight jet ($R = 0$). The crossflow effect was expressed in the form of a coefficient $\exp(\eta R)$ incorporated in the right-hand side of the equation. η was found to be on the order of -0.9 .

The dependence of s_o/d_o on F_o is complex. Values of F_o from 2 to 15 were experimentally investigated. In some cases there is almost no dependency of s_o on F_o . In others a significant dependency does exist. A function of the form $1 + \frac{\epsilon F_o + \beta}{\exp(\delta F_o)}$ has been used to match the data, but it has been found to be only partially satisfactory. The approximate values of the coefficients

ϵ , β , and δ are 0.5, -1.5, and 0.4 respectively. This function has a maximum at $F_o = 1/\delta - \beta/\epsilon = 5.5$.

6. The complete empirical equation proposed for s_o/d_o on the basis of the available data is of the form

$$\frac{s_o}{d_o} = (16.0 - 12.8 T)^{1.2} A^{(0.85-0.44T)} \exp(-0.9 R) \left(1 + \frac{0.5 F_o - 1.5}{\exp(0.4 F_o)}\right)$$

The values of the coefficients were initially derived from graphs and were improved upon using non-linear fitting. The equation was derived from experimental data covering the following flow conditions: $1.0 \leq A \leq 9.6$, $0 \leq R \leq 0.41$, $2.0 \leq F_o \leq 15$, $0.8 \leq T \leq 0.98$.

7. Except for very small aspect ratios ($A < 2$), it was observed that the shear in the vertical shear layer and the piercing of cold water from the bottom to the surface impose significant limitations on the length of the ZFE, at least for straight jets. Horizontal mixing appears secondary. The vertical mixing is presumably by large eddies and sometimes breaking internal waves.
8. Surface flow patterns did not provide realistic information on the length of the ZFE except for narrow outlet channels.
9. Total volumetric flow rates Q were computed from measured velocities. Values of Q increase with distance x from the outlet. The rate of increase can be measured by comparing total volumetric flow rates $Q(x)$ with the initial flow rate Q_o . The ratio $Q(x)/Q_o$ was found to depend more on aspect ratio A than on outlet Froude number F_o . The increase in total flow rate with increasing distance from the outlet was cast into a form which would give a power law increase of volumetric flows with the exponent depending on aspect ratio,

$$\frac{Q}{Q_o} = 1 + m_1 \left(\frac{x}{2d_o}\right)^{m_2(A)} \left[1 - \frac{n_1}{(n_2)^{F_o}}\right]$$

Using data for straight jets near the outlet and within $1.8 \leq F_o \leq \infty$ and $1.0 \leq A \leq 9.6$ only, non-linear fitting gave

$$\frac{Q}{Q_o} = 1 + \left[0.087 \left(\frac{x}{2d_o}\right)^{\frac{2.35 + .75A}{0.90 + A}}\right] \left[1 - \frac{0.52}{F_o^{0.41}}\right]$$

10. In jets with crossflow, large eddies with nearly vertical axes near the surface but bent over into the crossflow and reaching large depths are the most outstanding mixing mechanism (Fig. 34). Flow rates have not been computed for jets in crossflows.
11. The spreading of a heated surface jet near the outlet is known to depend on the densimetric Froude number at the outlet. A spreading angle can be defined and related to measurements and observations on the water surface. Referring to the definition of ϕ_o shown in Fig. 9 and using photographs (streaklines) of surface tracer particles contained in the receiving tank to show the edge of the jet, an empirical equation for ϕ_o was derived having the form

$$\phi_o = \frac{225 + 10 F_o}{2.25 + F_o} \quad \text{for } F_o \geq 1.0$$

In a previous study³, a tracer (lycopodium powder) was added to the discharged warm water rather than to the tank. Using the edge of the tracer cloud to measure the angle ϕ_o yielded much larger values of ϕ_o . The results from Ref. 3 can be given in the form

$$\phi_o = \frac{360 + 18 F_o}{2 + F_o} \quad \text{for } F_o > 0$$

The reason for the difference is that streaklines of tracers introduced in the ambient water show that portion of the flow field in which velocities are significant and therefore essentially identify the inner region of the actual jet; by contrast, an outward spreading dye pattern will more likely show the outer edge of the shear layer. This has significance for dye and drogue studies near prototype outfalls.

12. Froude number effects on the length of the ZFE, the volumetric flow rate, and the initial spreading angle were significant over the range of Froude numbers investigated ($0 \leq F_o \leq 15$). It would appear, therefore, that F_o values must be larger than 15 to eliminate buoyancy effects within the ZFE.

SECTION II
RECOMMENDATIONS

1. It is recommended that the experimental data and conclusions of this study be used to verify existing mathematical models for water temperature prediction in heated water surface plumes. The empirical relationships can be incorporated into such models.
2. It is recommended that empirical relationships similar to those derived for the length of the ZFE and the volumetric flow rate also be developed for the width and the depth of the heated surface jet within the outlet region. Sufficient data are available.
3. It is recommended that experiments similar to the ones described be conducted with discharges over sloping bottoms and different angles of discharge into the crossflow. The effects of these two parameters on the ZFE need further investigation.
4. It was found that at channel aspect ratios near 2, initial dilution of effluents is particularly strong at Froude numbers near 7.0, but quite sensitive to the shape of the channel (rectangular versus circular). It is recommended that studies be initiated to determine the optimum shape of surface outlet channels and the beneficial effects of artificially induced secondary motion on the initial dilution.

SECTION III

INTRODUCTION

Analytical, numerical models for predicting temperature distributions resulting from surface discharges of cooling water into lakes and reservoirs have been developed with increasing refinement over the past several years. The models of Stolzenbach and Harleman¹, Motz and Benedict², Stefan, Hayakawa, and Schiebe³, Prych⁴, and Shirazi and Davis⁵ can be cited. All these models are for steady-state jet flow; an integral technique is used to describe the simultaneous flow of mass, momentum, and heat along the main trajectory of the jet. The interaction with ambient water and the atmosphere is described through various coefficients for turbulent mass exchange, entrainment, friction, surface heat transfer, and other processes. Most of the models give a picture of the temperature field near a surface outfall of cooling water which appears to be realistic. It is uncertain, however, whether the models can predict actual temperature distributions with the accuracy which would be desirable in view of the stringent temperature standards set by federal and state agencies. Temperature predictions made by the models are inaccurate for a number of reasons, including (a) inadequate formulations of the fundamental equations (e.g., similarity of temperature and velocity profiles), (b) inadequate numerical values of the coefficients used (e.g., for turbulent entrainment from ambient currents), and (c) inadequate match between a real outfall situation and its idealized version as used in the mathematical model.

Following classical, semi-empirical jet flow theories, mathematical models of heated water surface jets consider separately a zone of flow establishment and a fully established flow region. The zone of flow establishment (ZFE), or more accurately, re-establishment, forms a transition from the wall-shear-controlled flow in the outlet channel or pipe to the free-shear flow in the receiving open body of water. There is a lack of adequate information on the length of the zone of flow establishment and the initial entrainment rates in the vicinity of the

outfall and their relationship to outlet design and the operational characteristics of the discharge flow. It was for this reason that an experimental study was conducted to obtain such information. The authors have felt for some time that theoretical treatment of the ZFE would be difficult because of the three-dimensional and transitory character of the flow field. For this reason, only the fully established jet flow was considered for mathematical modeling (see Stefan, Hayakawa, and Schiebe³). The information provided through the study described herein can now be used to determine where the fully established flow region begins and what the volumetric flow rate at that point will be. This information can be incorporated in the mathematical model to provide a realistic picture of the temperature and flow field downstream of the cooling water outfall.

SECTION IV

ZONE OF FLOW (RE-)ESTABLISHMENT

The outlet region of a cooling water surface discharge usually forms the transition from a channel flow to a free-jet flow as shown schematically in Fig. 1a for discharge from a shallow rectangular channel into a deep pool. The initial core region and the shear layer, as they appear on the water surface, are shown in Fig. 1b. It is noteworthy that the free-shear layer grows from the edges of the channel toward the center of the jet. The zone of flow establishment or re-establishment ends when the free-shear layer has reached the centerline or main trajectory of the jet. This point will be designated by x_0 (straight jets) or s_0 (curvilinear jets). Whether it is caused by the vertical growth of the free-shear layer, as shown schematically in Fig. 2, or by the lateral growth is irrelevant to the definition of x_0 and s_0 , but important for an understanding of the dependency of x_0 and s_0 on the independent variables.

A zone of flow establishment is common to all jet flows. A detailed description of it was given for circular, neutrally buoyant, submerged jets by Albertson, Dai, Jensen, and Rouse⁶, among others. A theoretical analysis of the zone of flow establishment for fully submerged, round, buoyant jets was made by Hirst⁷ using the integral technique.

The heated water surface discharge is a buoyant half-jet due to the presence of the water surface; in addition, the orifice from which the discharge is released is often non-circular, and a cross-flow may be superimposed. Some consideration was given to the zone of flow establishment in existing models. Information on its length was collected and synthesized by Shirazi⁸. It was concluded, however, that not enough information was available for adequate description and modeling of this zone. An experimental investigation was therefore undertaken to determine the characteristics of the flow inside and outside of the

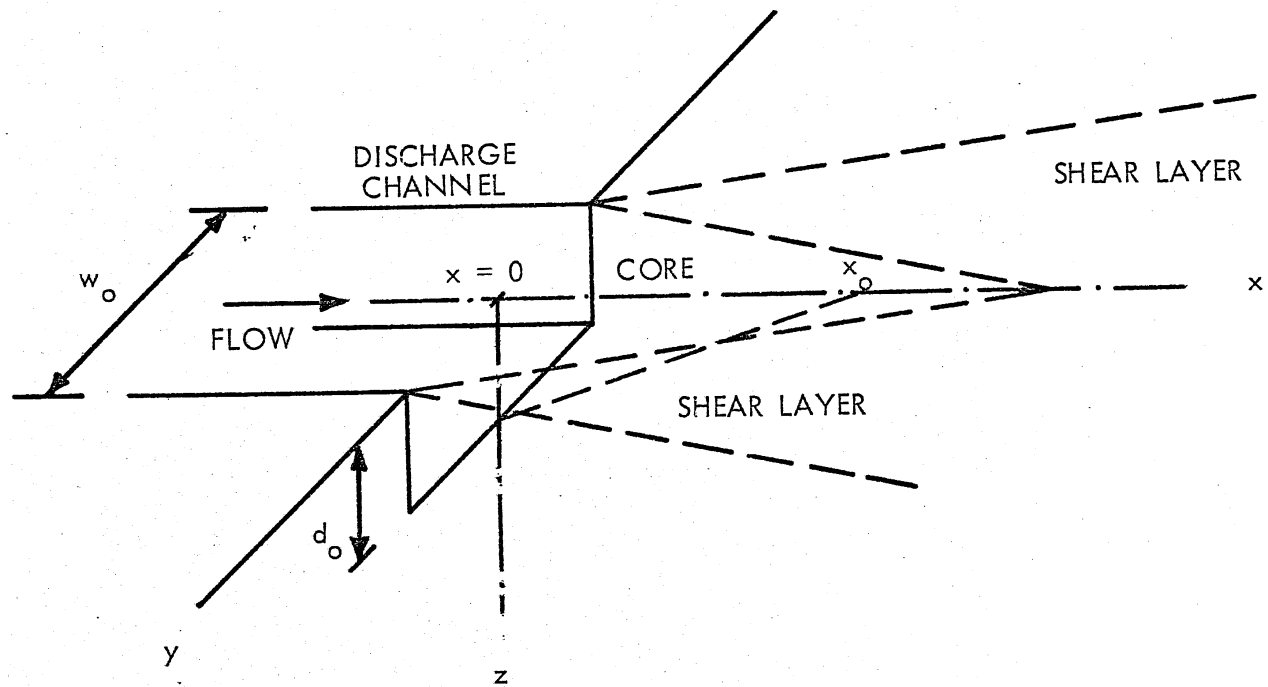


Fig. 1a - Schematic showing zone of flow establishment (ZFE) near a surface outlet

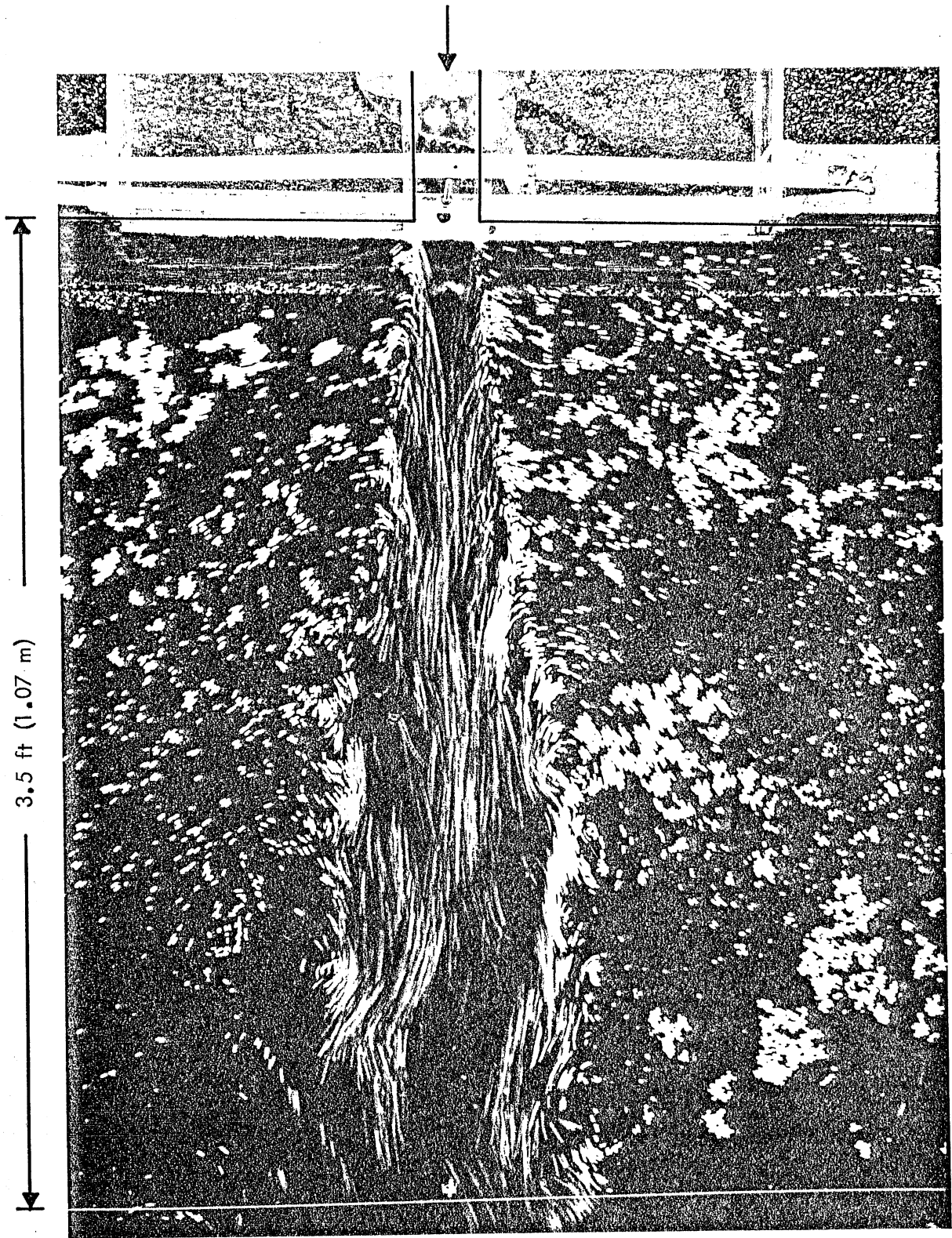


Fig. 1b - Streaklines illustrating the surface flow pattern and flow establishment -
 $A = 1.0$, $R = 0$, $F_o = \infty$, Exposure = $1/5$ sec

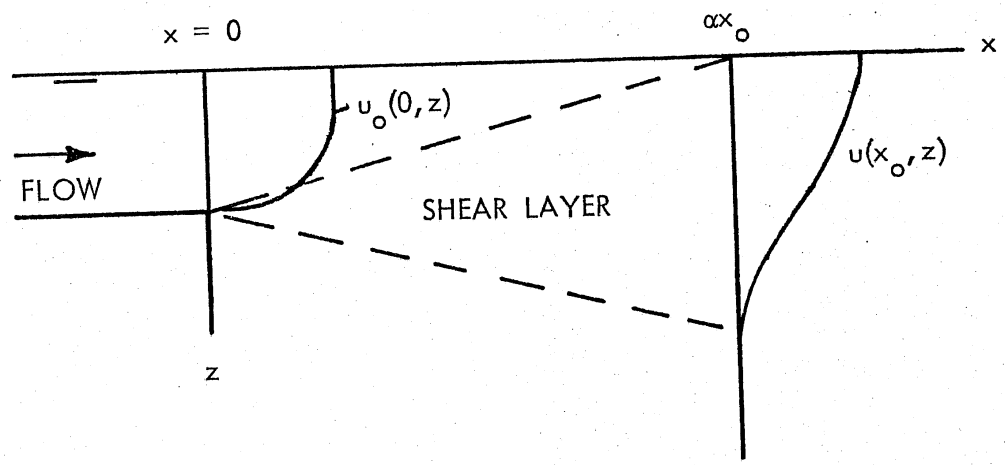
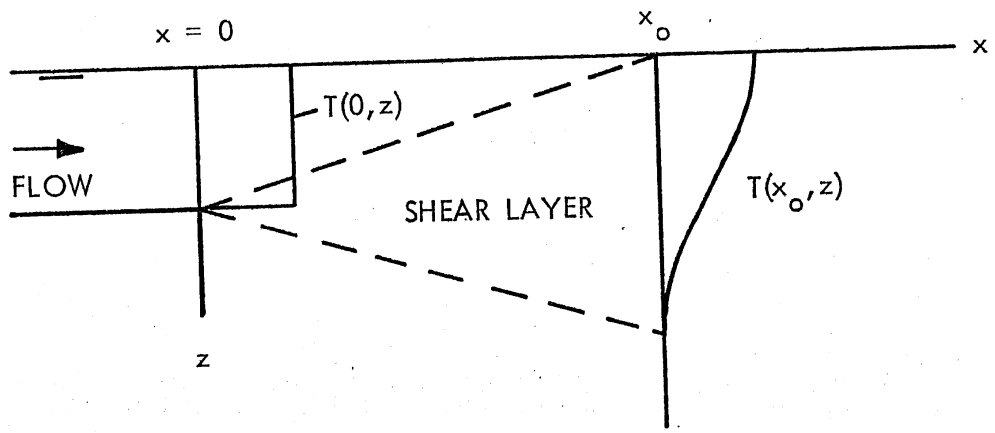


Fig. 2 - Temperature and velocity distributions at the beginning and end of the zone of flow establishment (schematic)

zone of flow establishment in heated water surface jets. Specifically, the length of the zone of flow establishment, the mechanism of dilution, and the amount of dilution were investigated. The information was obtained using measurements of time-averaged temperature distributions, turbulent temperature fluctuations, time-averaged velocity distributions, turbulent velocity fluctuations, and flow visualization.

Discharges from rectangular channels into deep bodies of water as shown schematically in Fig. 1a were investigated exclusively. The independent variables were the channel width, w_o ; the discharge rate, Q_o ; the temperature differential at the outlet, $T_o - T_a$, where T_o is the discharge temperature at the outlet and T_a is the ambient water temperature in the lake or reservoir; and the ambient cross-flow velocity, U_a , past the outlet. The primary dependent variables measured were local water temperatures $T_l - T_a$ or flow velocities U , from which all other information was derived, including the length of the ZFE, x_o or s_o , and the entrainment expressed in terms of the flow rate Q . The flow rate Q was obtained by integration of local velocities over an area perpendicular to jet trajectory.

The independent variables were grouped into the following dimensionless parameters:

Aspect ratio:

$$A = w_o/d_o \quad (1)$$

Outlet densimetric Froude number:

$$F_o = \frac{U_o}{\sqrt{\frac{\Delta \rho_o}{\rho_o} g d_o}} \quad (2)$$

Outlet Reynolds number:

$$Re_o = \frac{U_o d_o}{\nu_o} \quad (3)$$

and cross-flow velocity ratio:

$$R = U_a / U_o \quad (4)$$

In the four equations above,

d_o = depth of rectangular discharge channel

U_o = average discharge velocity $Q_o / (w_o d_o)$

$\Delta \rho_o = \rho_a - \rho_o$ = density differential between the density of the ambient (cold) water, ρ_a , and that of the discharged warm water, ρ_o

g = acceleration of gravity

ν_o = kinematic viscosity of the water at the discharge

The dependent variables were also reduced to dimensionless forms, including the following:

Excess temperature ratio for time-averaged temperatures:

$$T = \frac{\bar{T}(x,y,z) - T_a}{T_o - T_a} \quad (5)$$

Excess temperature ratio for fluctuating temperature components:

$$\delta T = \frac{\sigma_T(x,y,z)}{T_o - T_a} \quad (6)$$

Time-averaged velocity ratio:

$$V = \frac{\bar{U}(x,y,z)}{U_{m,o}} \quad (7)$$

Fluctuating velocity component ratio:

$$\delta V = \frac{\sigma_V(x,y,z)}{U_{m,o}} \quad (8)$$

In the above relationships,

$\bar{T}(x,y,z)$ = a real, time-averaged local water temperature value

$\sigma_T(x,y,z)$ = standard deviation of the fluctuating water temperature component at location (x,y,z)

$\bar{U}(x,y,z)$ = time-averaged local water velocity

U_{m_0} = maximum velocity at the outlet

$\sigma_V(x,y,z)$ = standard deviation of the fluctuating water velocity component

When values of T , δT , V , or δV were plotted versus location, the dimensions x,y,z were normalized using x/d_0 , y/d_0 , z/d_0 , or s/d_0 , where d_0 is the outlet depth. From the above information the following relationships were specifically sought:

- a) The length of the zone of flow establishment, x_0/d_0 or s_0/d_0

$$\frac{x_0}{d_0} = f_1(A, F_0, R, Re_0) \quad (9)$$

- b) The dilution

$$\frac{Q(x)}{Q_0} = f_2(A, F_0, R, Re_0) \quad (10)$$

SECTION V

EXPERIMENTAL FACILITY AND DATA ACQUISITION

BASIC EQUIPMENT

The experimental facility consisted of a tank 40 ft (12.2 m) long, 16.5 ft (5.0 m) wide, and 1.5 ft (0.46 m) deep, thermally insulated all around and with an instrumentation carriage riding on top. The heated water was discharged from a rectangular channel with a maximum width of 2.32 ft (0.71 m) and a depth of up to 0.25 ft (0.076 m). A round stainless-steel pipe 0.369 ft (0.112 m) in diameter was used in some preliminary experiments. The outlet was placed at right angles to the wall of the tank. Average discharge velocities ranged from 0.1 to 1.5 ft/sec (0.03 to 0.5 m/sec) and temperature differentials from 5 to 30°F (3 to 17°C). Figure 3a shows the overall dimensions of the tank. Maintaining an unstratified stagnant pool while injecting heated water at the surface is very difficult. A manifold withdrawal pipe placed across the tank 27 ft (8.25 m) from the outlet was used for the purpose. More water was removed than was injected. To compensate for the difference and replenish the cold water volume constantly, a feeder system at the downstream end of the tank was used. A constant water level was maintained in the tank using an overflow weir (Fig. 3a).

Velocities and temperatures in the flowfield near the outlet were measured with several types of sensing devices which are schematically represented in Fig. 3b:

- a) Single YSI thermistors, types 427 and 406, with time constants of 0.5 and 2.5 seconds respectively;
- b) Rakes of YSI thermistors of the same types carrying eleven sensors at 0.5 inch (0.0127 m) vertical intervals;
- c) TSI hot film current meter, VT 1630T, 0 - 3 fps (0 - 0.9 m/s), threshold velocity approximately 0.05 fps (0.015 m/s);
- d) Delft propeller current meter, propeller diameter 15 mm, range 1 to 120 cm/sec.

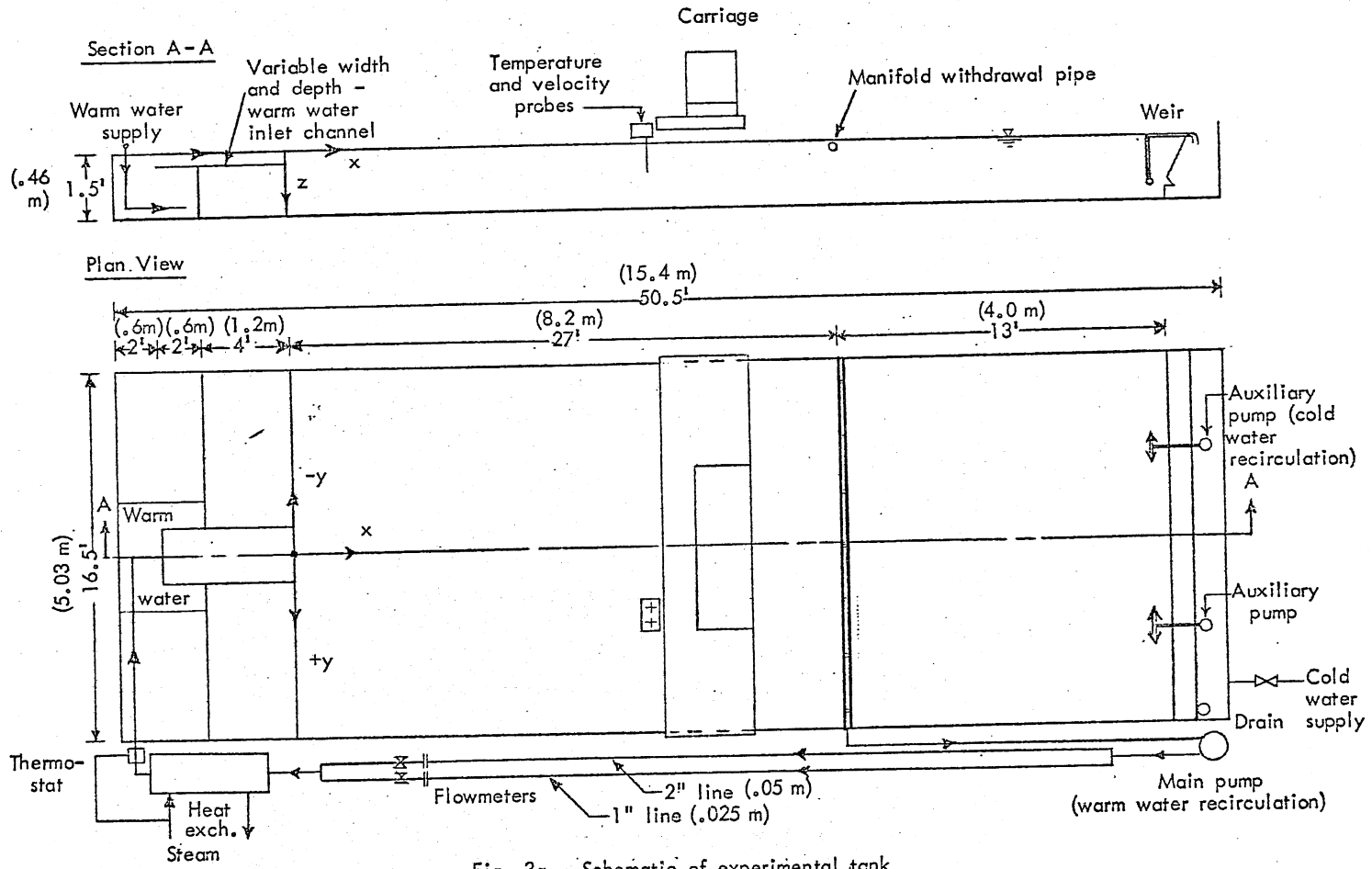
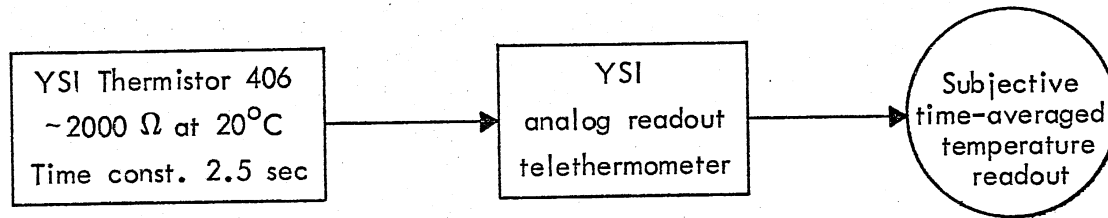
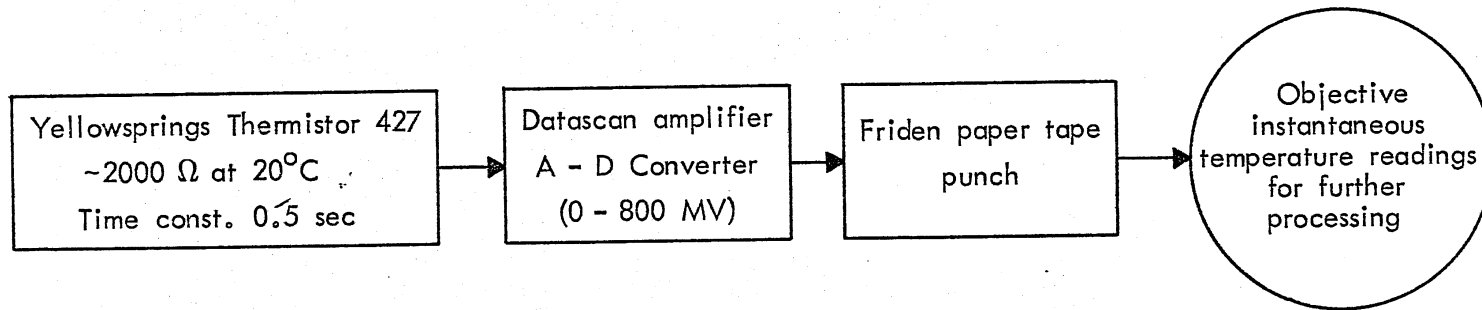


Fig. 3a - Schematic of experimental tank

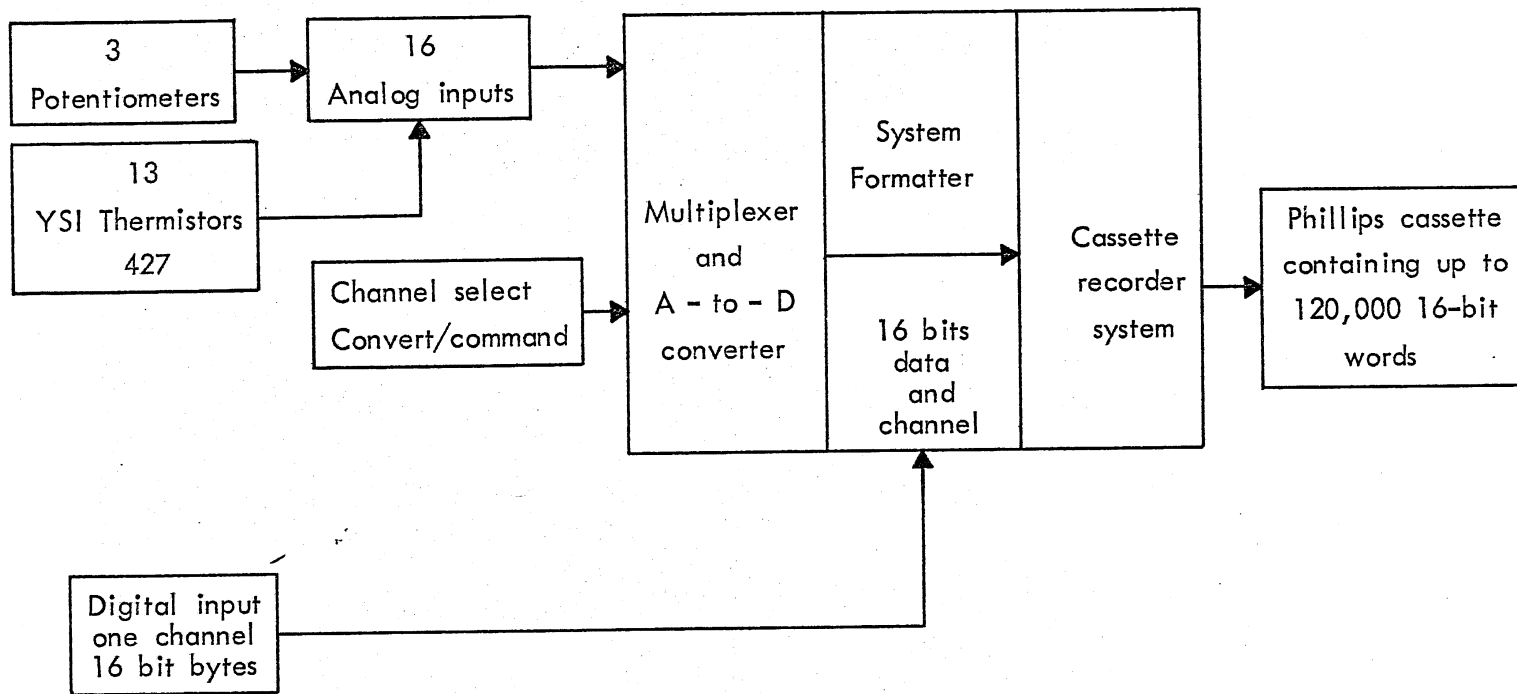


(a) Preliminary temperature measuring instrumentation



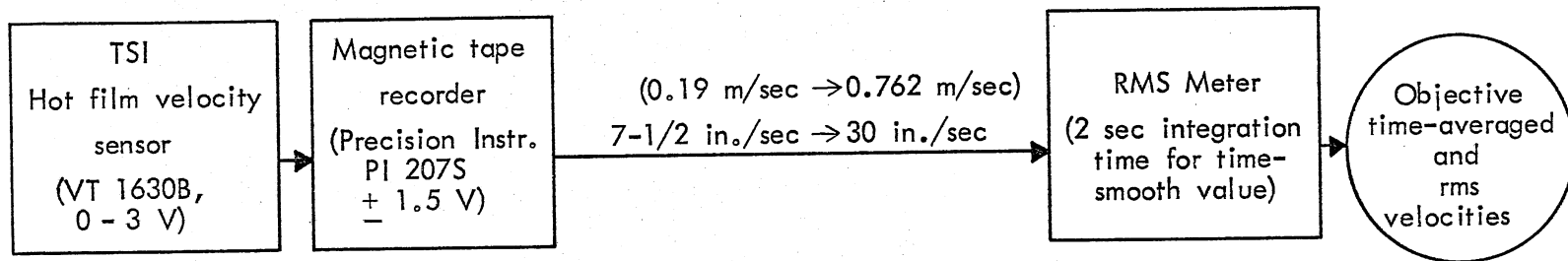
(b) Intermediate temperature measuring instrumentation

Fig. 3b - Schematic diagrams showing evolution of temperature and velocity measuring and recording systems in the course of the investigation



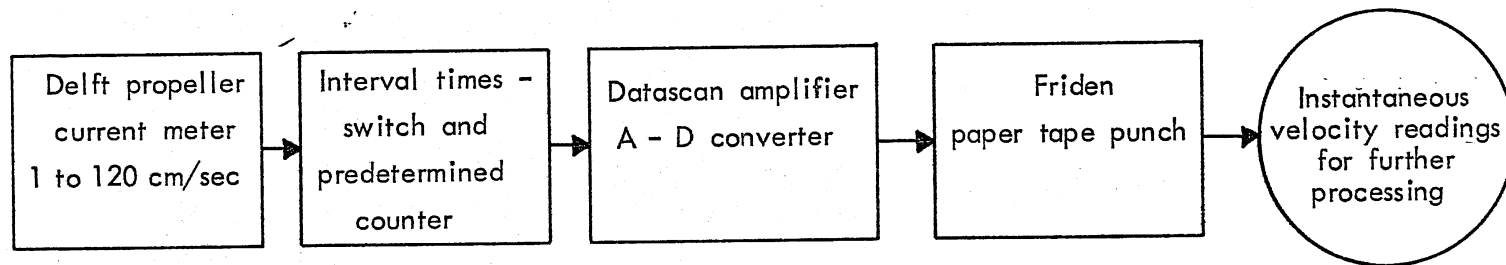
(c) Temperature data-logger system functional block diagram, System LPS-16

Fig. 3b (continued) - Schematic diagrams showing evolution of temperature and velocity measuring and recording systems in the course of the investigation



(d) Intermediate velocity measuring instrumentation

20



(e) Velocity data recording system

Fig. 3b (continued) - Schematic diagrams showing evolution of temperature and velocity measuring and recording systems in the course of the investigation

These sensors were used interchangeably.

Several types of metering and recording devices were used, including

- a) YSI direct readout telethermometer;
- b) Direct readout Delft current meter;
- c) Datascan A/D converter linked to a Friden model 2, 8-column paper punch;
- d) A DATEL digital data logging system LPS-16.

The Datascan/Friden system had only one channel. It was used initially to record individual temperatures and later to record velocity readings. Peripheral information could be added manually to the paper tape.

The DATEL system scans and records 16 data points in digital form on a cassette tape. One sweep of all 16 channels requires approximately two seconds. The DATEL system was used primarily to record turbulent temperatures sensed by the thermistor rake in the outlet region, where the mixing of the effluent with ambient water is rather intense. The data acquisition system was programmed to take three consecutive samples. Each sample contained 15 individual measurements at each point. Therefore a total of 45 individual measurements were obtained over a 90-second period at each location. The following parameters were recorded on the 16 channels of the data acquisition system:

- a reference warm water outlet temperature, T_o
- a reference cold water (tank) temperature, T_a , taken at a point with coordinates $x = d_o$, $y = w_o + 2d_o$, $z = d_o$
- the x , y , and z coordinates of the topmost temperature sensor of the rake.

Prior to the sampling, auxiliary integer input giving experiment number and date were recorded on the cassette. During the processing of the data, additional identifiers for channel depth d_o , channel width w_o ,

outlet densimetric Froude number F_o , and Reynolds number Re_o (computed during the processing) are added to the output.

Raw data recorded on magnetic or paper punch tape were processed on a Raytheon 703 data storage and processing unit. The first step was a conversion of recorded digital values to real temperatures or real velocities as required. The necessary calibration curves had been obtained prior to the experiments.

Although temperature sensors were of the YSI 400 interchangeable series, each sensor used was calibrated individually. The calibration curves were nearly linear, and third order polynomials were found to fit the calibration data in the useful range of 45 to 95°F (7 to 35°C) to within 0.2°F (0.1°C).

Velocities were sampled at a rate of 50 measurements per minute. Fifty individual measurements were taken at each location. It was verified that the sampling period was long enough. The response of the Delft current meter to turbulent velocity fluctuations has been investigated by Schuyf¹⁵. Velocity fluctuations with frequencies up to 2 Hz can be recorded with little damping.

The velocity calibration was linear, and conversion of the raw data was therefore quite easy.

Temperatures as well as velocities are turbulent in major portions of the outlet region. From the sample data, all of which were obtained under steady flow conditions, time-averaged values and standard deviations were calculated. For this computation, 45 individual data points were available at each location. With time constants on the order of 0.5 seconds, the sensors used were capable of sampling all the lower frequencies present in the large-size, low-velocity flow field.

ADAPTATION OF EXPERIMENTAL FACILITY FOR CROSS-FLOW EXPERIMENTS

To generate a cross-flow in front of the discharge channel, two manifold systems were installed as shown in Fig. 4a. The cross-flow was produced by upstream discharge from one manifold and downstream withdrawal

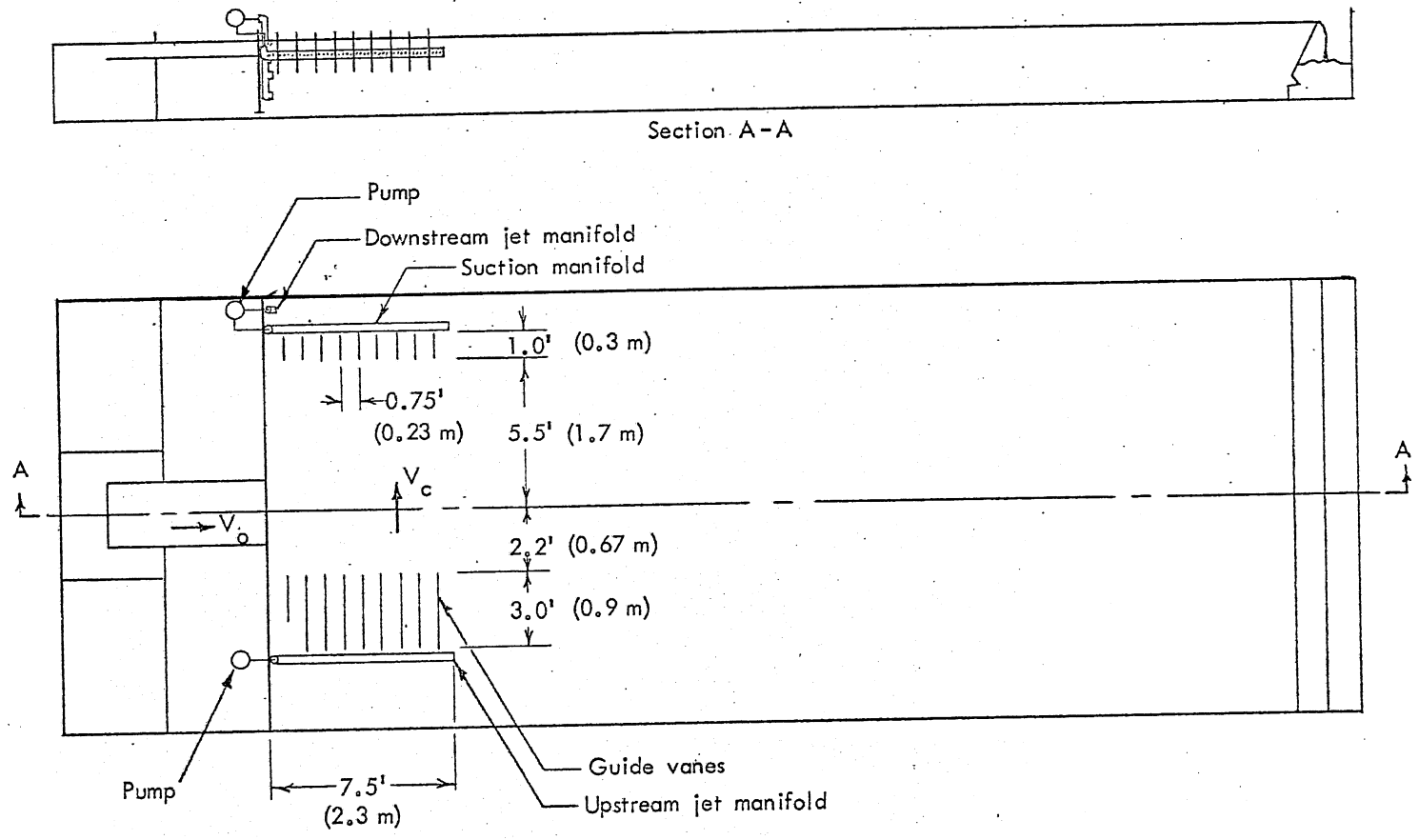


Fig. 4a - Schematic of adaptation of experimental tank for crossflow experiments

through the other. A large vortex was generated in the tank. The flow past the outlet channel was straightened with the aid of a series of guide vanes spaced at nine-inch (23 cm) intervals. A view of the plume in a cross-flow, looking down the discharge channel, is given in Fig. 4b. An average cross-flow velocity $\bar{U}_a = 0.22$ fps (0.067 m/sec) was applied in all experiments. Local deviations from this average were by up to ± 0.06 fps, as is shown in Fig. 4c. The average discharge velocity was maintained at $U_o = 0.53$ fps (0.162 m/sec), giving $R = 0.41$. The upstream velocity profile had a gradient with depth as shown in Fig. 4c. This is typical of wind-driven lake currents as well as gravity flows. The average cross-flow turbulence level measured at a distance $y/d_o = 3.1$ upstream from the axis of the outlet channel and averaged over a depth $0 < z/d_o < 1.0$ and a distance $0 < x/d_o < 28.8$ was 26 per cent in all experiments. The outlet depth d_o was 0.243 ft (0.074 m).

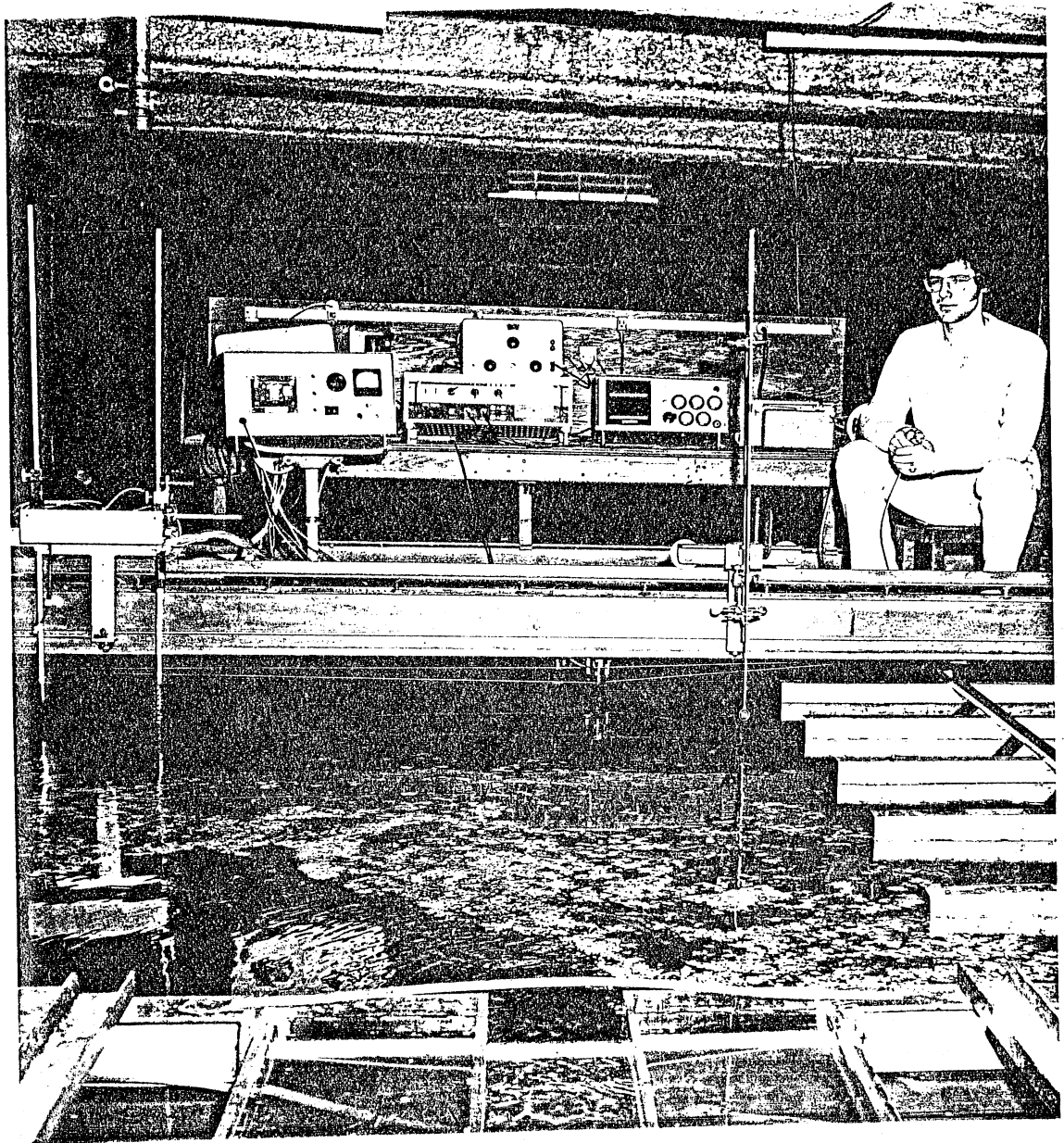
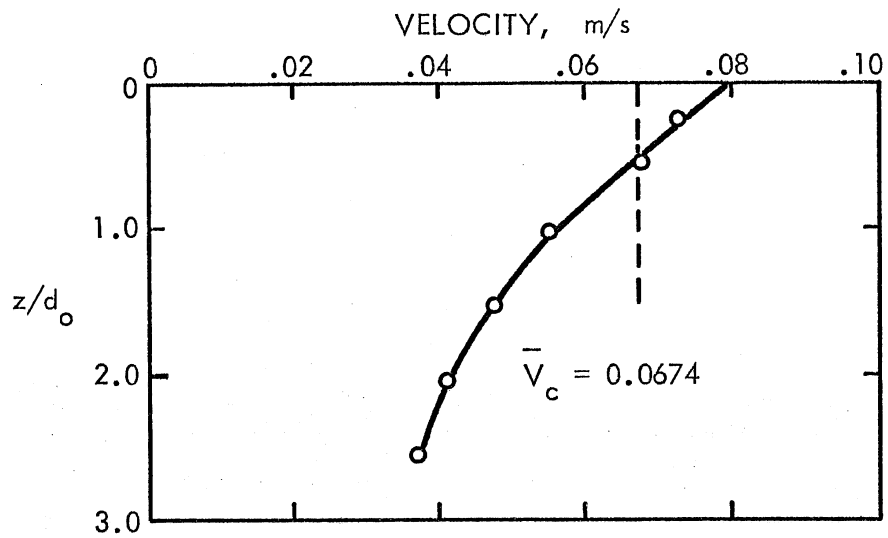


Fig. 4b - Experimental tank. Heated water discharge channel in foreground. Crossflow from right to left. Thermistor rake (left) and current meter (right) suspended from carriage. Instrumentation consisting of (from left to right) Datel data acquisition unit, current meter readout, timer (top), A-D converter and paper tape punch



Average vertical velocity profile at $y/d_o = 3$

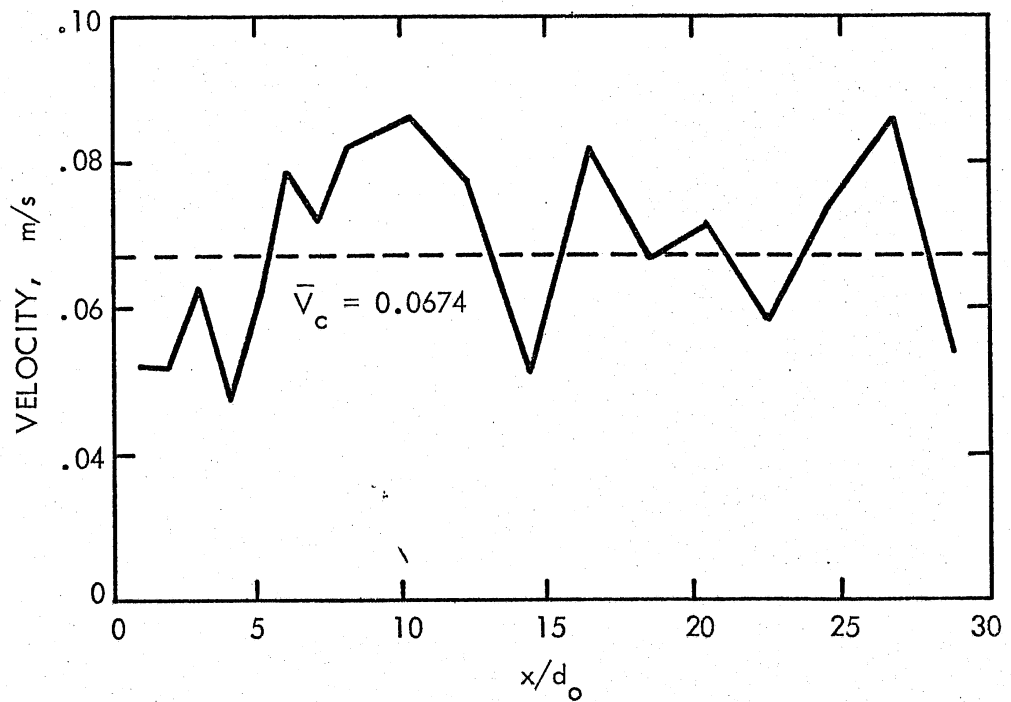


Fig. 4c - Crossflow velocity profiles

SECTION VI

EXPERIMENTAL RESULTS

PILOT STUDIES

Before the investigation described herein was begun, two series of pilot studies were conducted. A circular pipe, 4.4 inches (0.112 m) in diameter, flowing half full was used as an outlet channel. In the first series of experiments, water temperatures along the axis of the surface jet were measured with a slow response thermistor (time constant ≈ 2 sec). In the second series, overhead photographs of surface tracers were made.

In Figs. 5a and 5b the temperature results are reported in terms of normalized excess temperatures above ambient versus axial distance. Results have been plotted separately for low ($F_o < 4$) and high ($F_o > 7.5$) Froude numbers to draw attention to the significant differences between the results in these two categories. The differences are that (a) a decrease in axial temperatures occurs closer to the outlet for low densimetric Froude numbers than for high Froude numbers and (b) the rate of temperature decrease with distance is higher for the higher Froude numbers. The densimetric Froude numbers shown are based on the maximum depth d_o of the outlet channel.

No physical reason for the difference was discovered at the time of the experiments. It will be shown later that the buoyancy-induced lateral spread of the plume enhances the vertical breakthrough of the free shear zone if the aspect ratio w_o/d_o of the discharge channel is small. This reduces the establishment length. On the other hand, higher outlet Froude numbers are associated with higher discharge velocities and higher turbulence and hence more rapid dilution of the discharge. A dependency on Reynolds numbers, if it exists, could not be established because Reynolds numbers could not be varied over a wide enough range.

For circular, fully submerged, non-buoyant jets the length of the zone of flow establishment is generally accepted as 6.2 times the diameter. This value was established by backward extrapolation from

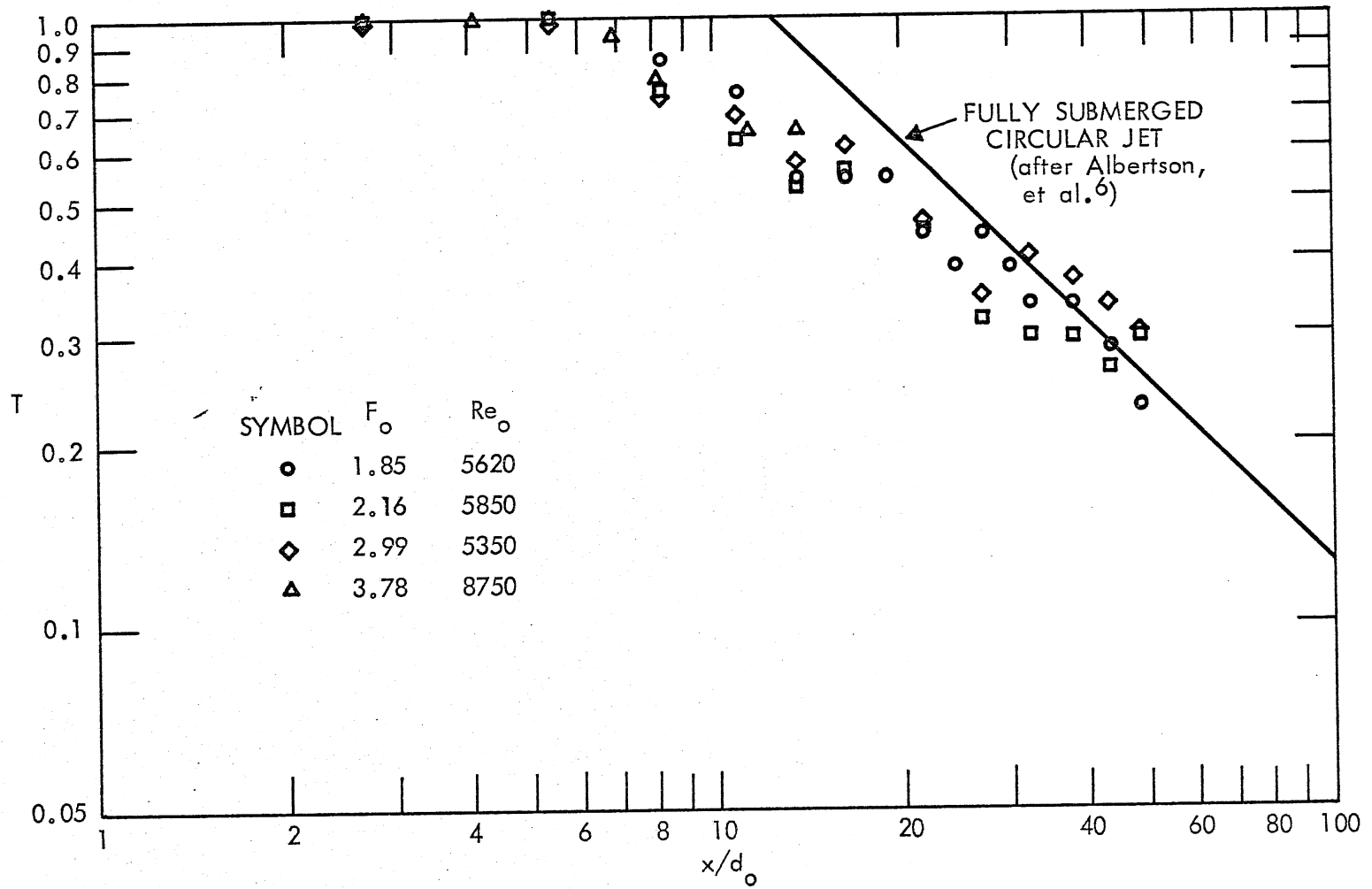


Fig. 5a - Surface centerline temperature versus axial distance, semicircular outlet, low F_o

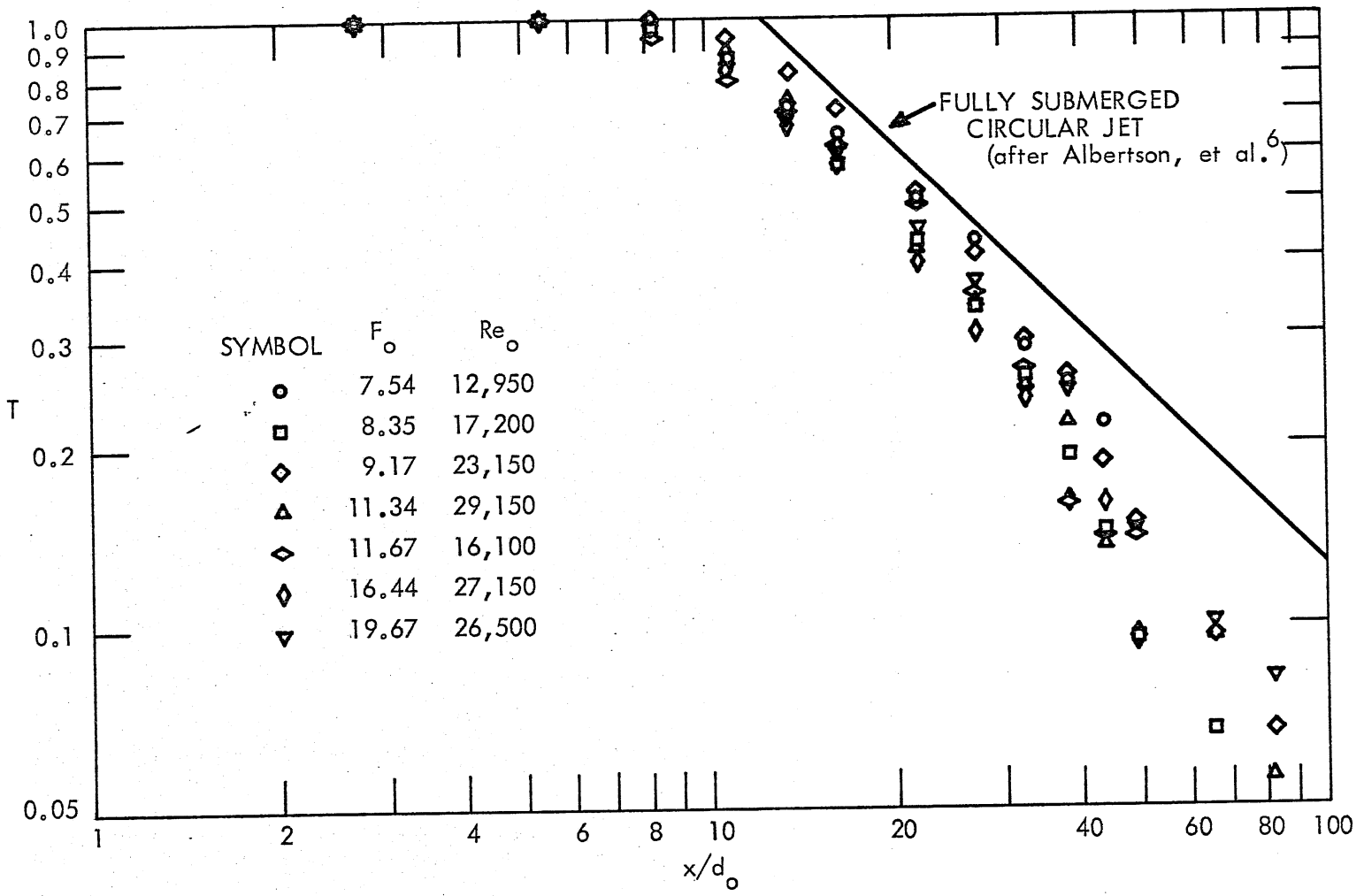


Fig. 5b - Surface centerline temperature versus axial distance, semicircular outlet, high F_o

centerline velocity measurements as shown in Fig. 6 (see, for example, Reference 6). A backward extrapolation cannot easily be applied to the data of Fig. 5 because the data, particularly for the higher Froude numbers, do not fall on a straight line.

The difficulty in applying the extrapolation procedure is, of course, that a jet with a high densimetric Froude number at the outlet tends toward smaller local densimetric Froude numbers (for which buoyancy effects are important) as it moves away from the outlet. This was shown by Stefan, Hayakawa, and Schiebe³ and explains many of the heated surface jet's characteristics, including the observation that a log temperature concentration versus log distance plot as shown in Fig. 5 does not give a straight line in the fully established flow region. This has also been documented by other investigators, including Dornhelm, Nouel, and Wiegel⁹, Tamai, Wiegel, and Tornberg¹⁰, and Jen, Wiegel, and Mobarek¹¹. It is therefore quite difficult to use the standard procedure of backward extrapolation illustrated in Fig. 6 to define the length of the zone of flow establishment. A number of more general alternatives for specifying the length of the ZFE had to be considered.

It is important to emphasize that the real instantaneous length of the zone of flow establishment fluctuates considerably in time because the jet discharge produces a highly turbulent flow and eddies in the free shear layer are of considerable size relative to the size of the outlet. The length of the ZFE must therefore be defined on the basis of either time-averaged measurements or intensities of fluctuating components. Measurements of water temperature, flow velocity, or tracer materials can be used. Figure 7 illustrates this approach using instantaneous temperature measurements or velocity measurements. It is apparent that a definition of the ZFE based on time-averaged values is quite sensitive to the absolute temperature level at which the end of the ZFE is marked. Normalized excess temperature values T and centerline velocity ratios V on the order of 0.98, 0.95, 0.90, 0.85, and 0.80 will be used as cutoff points. Fluctuating components of temperature and velocity are also suited to defining the establishment length, because they are

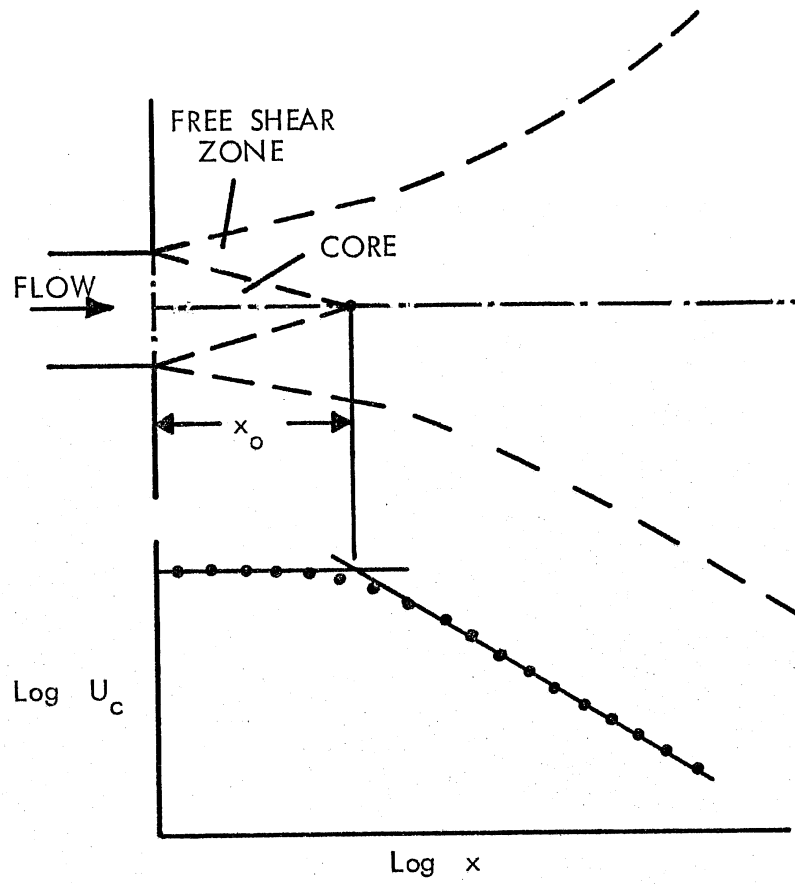


Fig. 6 - Definition of zone of flow establishment for non-buoyant, fully submerged jets (after Albertson, et al.⁶)

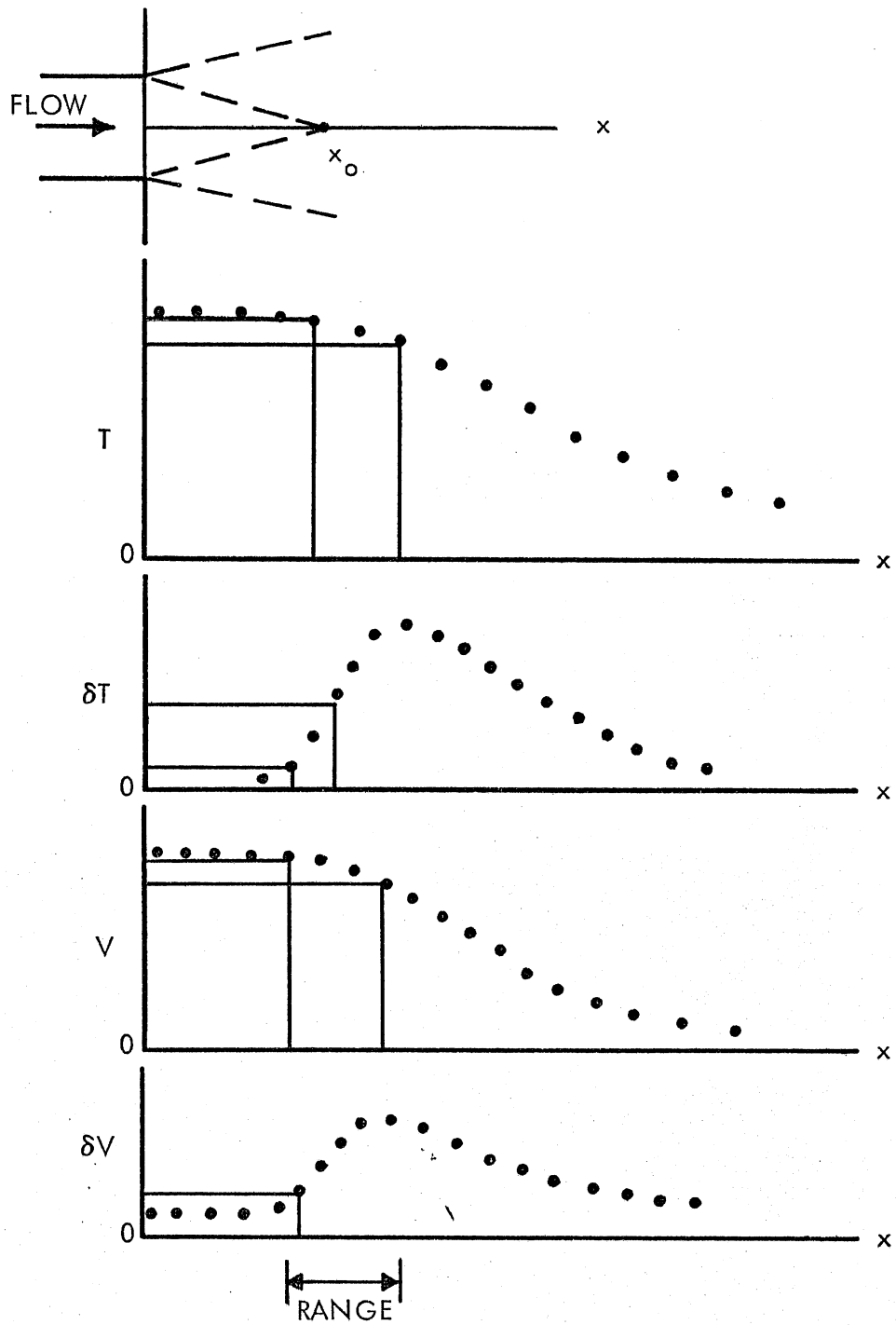


Fig. 7 - Schematic showing range of alternative values of x_0 depending on definition

nearly independent of ambient temperature controls. Values of T and V on the order of 0.02, 0.04, and 0.10 will be used. With any of the definitions used there will be significant spread, as is shown in Fig. 7.

A reduction of the data of Figs. 5a and 5b in terms of T versus x/d_0 is given in Fig. 8a. Some data for a negatively buoyant jet are shown in Fig. 8b. Buoyancy effects for the negatively buoyant jet begin to show up at $F_0 < 30$, whereas positive buoyancy appears to be negligible at $F_0 > 20$. This could be interpreted as a surface effect; the free surface does not significantly hinder the sinking plume, but it is a boundary for the rising (positively buoyant) one.

Because of the aforementioned difficulties, another series of pilot experiments was run. Tracer particles on the surface of the tank were used to show the surface spreading and mixing pattern near the outlet. Because the water discharged from the channel was clear, a visual impression of the extent and shape of the zone of flow establishment on the water surface was obtained. A graduated marker suspended over the water surface was used to estimate x_0 . The length of the ZFE could not be measured easily in this way, because the end of the zone is usually marked by the convergence of large eddies which form in the free shear zone between the free surface jet and the ambient reservoir. Since these eddies move downstream apparently randomly, the length x_0 also varies randomly with time around some mean value. It was therefore decided to use the average of several photographs to record visual values of x_0 . These data are of some interest for winter conditions; they are reproduced in Fig. 8b and supplement Fig. 8a.

The photographic records can also be used to derive lateral spreading angles for the shear zone ϕ_0 and spreading angles for the core region. A set of values of ϕ_0 is given in Fig. 9. The strong dependence of ϕ_0 on F_0 and the nearly complete lack of dependence on A , the aspect ratio, are quite obvious. This means essentially that the buoyancy-induced initial lateral spreading is quite similar in all situations in which the discharge Froude number is the same. A

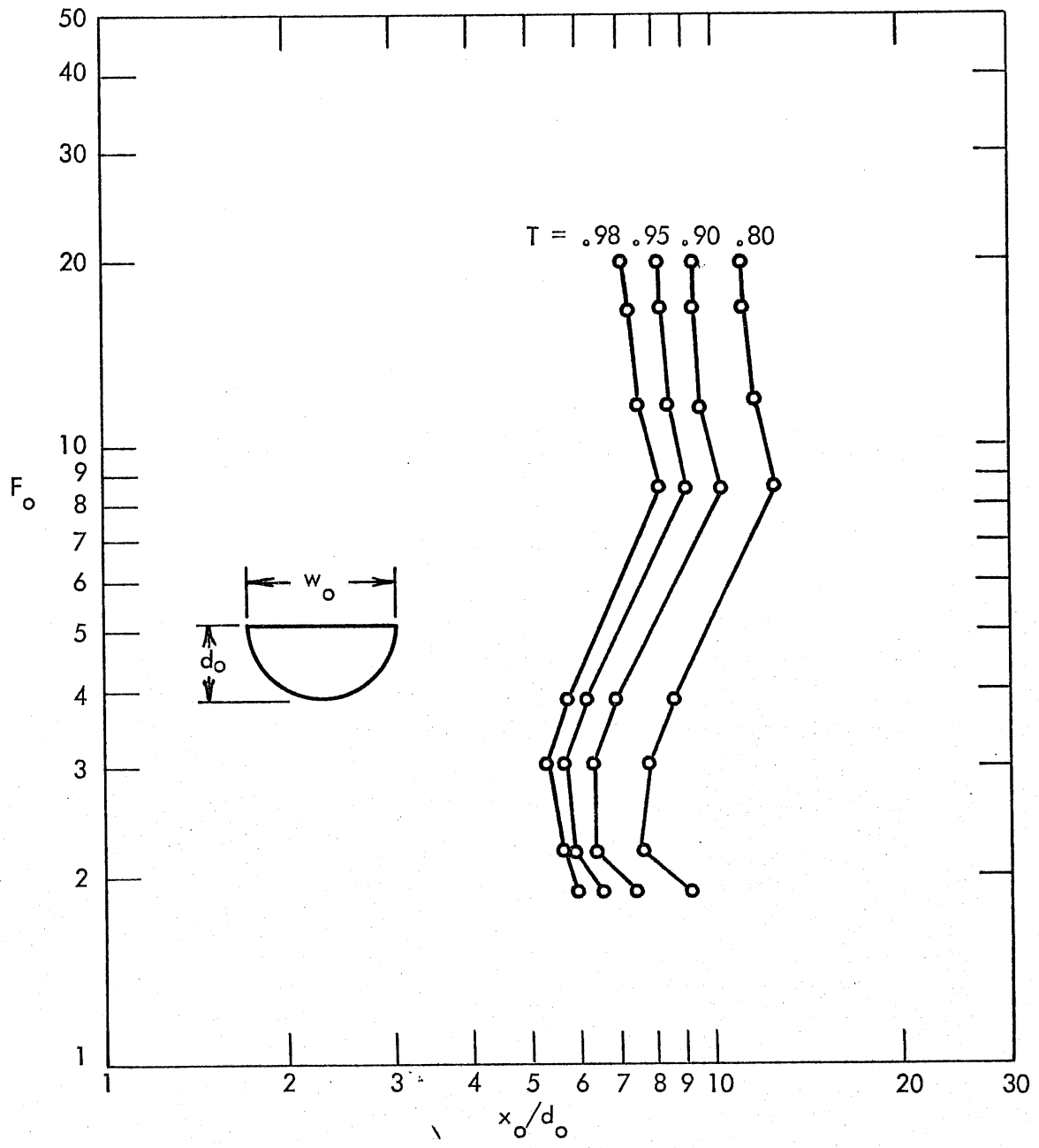


Fig. 8a - x_o/d_o versus F_o at $T = 0.98, 0.95, 0.90,$ and 0.80 and $A = 2.0$ (semicircular pipe, positive buoyancy)

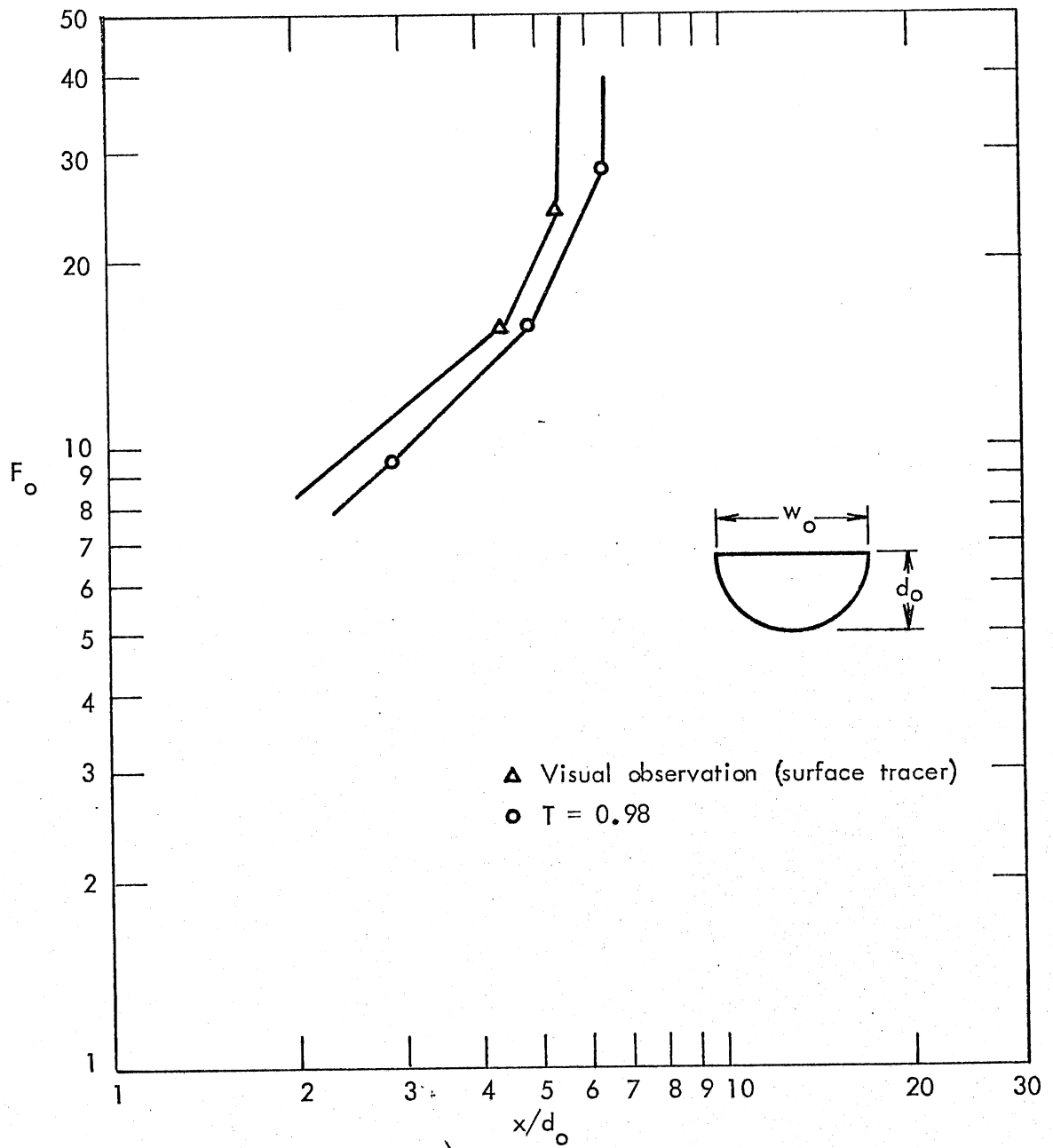


Fig. 8b - x_o/d_o versus F_o at $T = 0.98$ and visual observations, $A = 2.0$ (semicircular pipe, negative buoyancy)

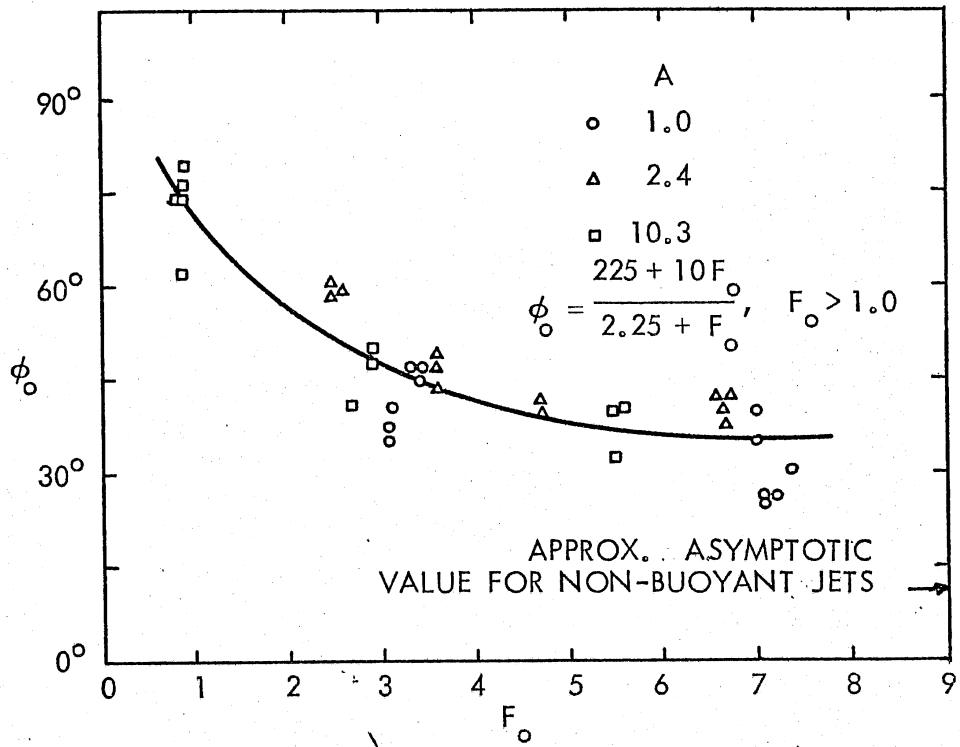
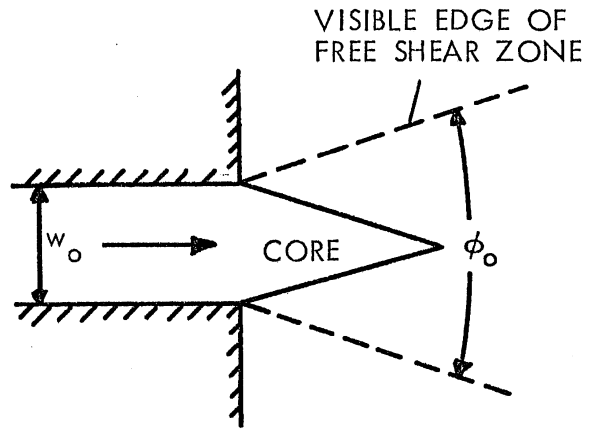


Fig. 9 - Horizontal spreading angle, ϕ_0 , of free shear zone recorded photographically (average value of $\phi_0 = 10^\circ$ at $F_0 \rightarrow \infty$ not shown)

dependency on aspect ratio need not be included initially. Mathematical modeling of the width of thermal surface plumes has been a problem, and relationships for surface spreading have mostly ignored the effects of the aspect ratio. The information provided should be helpful in resolving some of the difficulties.

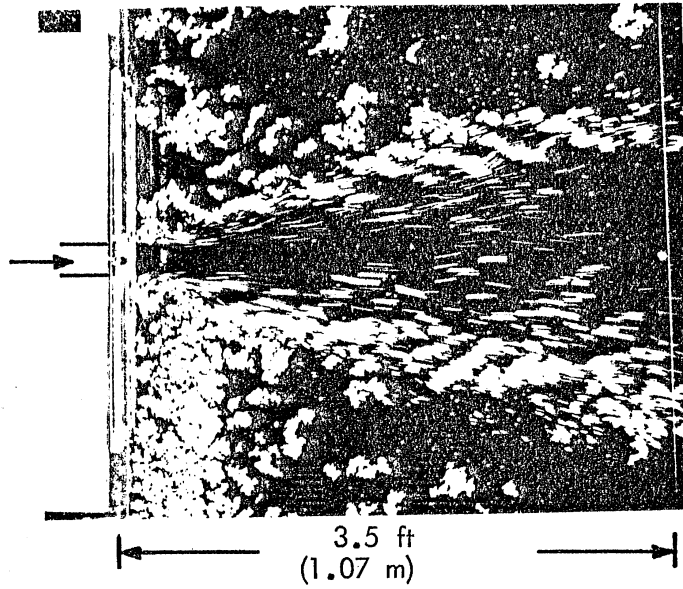
MAIN EXPERIMENTS: STRAIGHT JETS

Length of Zone of Flow Establishment (ZFE)

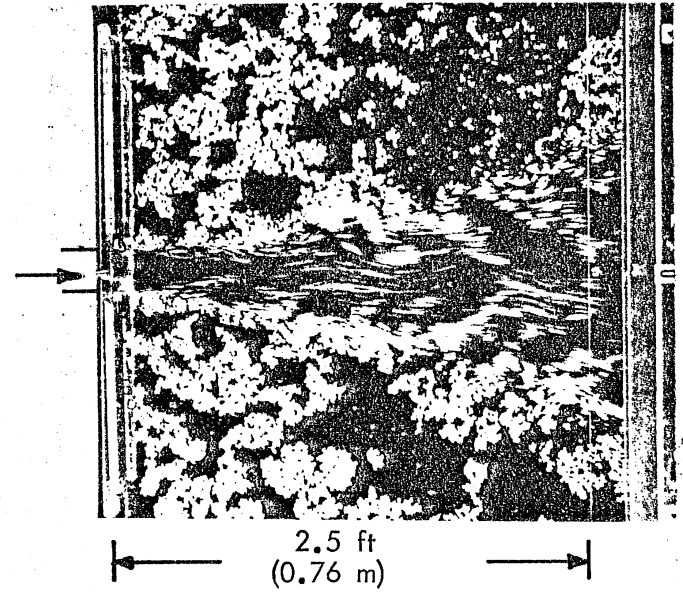
Photographs of Surface Flow

White, buoyant, nearly spherical particles with a specific gravity of approximately 0.95, approximately 3/16 inch (5 mm) in diameter, were spread on the surface of the experimental tank and retained there by a boom which prevented their entrainment into the recirculating flow. Water discharged from the outlet channel entrained the surface particles. The core region and the shear layers, defined schematically in Fig. 1a, were made visible by the behavior of the particles on the water surface of the tank. The core region was represented by a dark triangular area and the shear layer by the random path of the particles, which contrasted with the particle path in the ambient, more quiescent pool. Figures 10a, 10b, and 10c give illustrations for outlet channel aspect ratios $A = 1, 2.4, \text{ and } 9.6$ and Froude numbers F_o ranging from ω (isothermal) to 2.5. A closer inspection of the photographs reveals the following features:

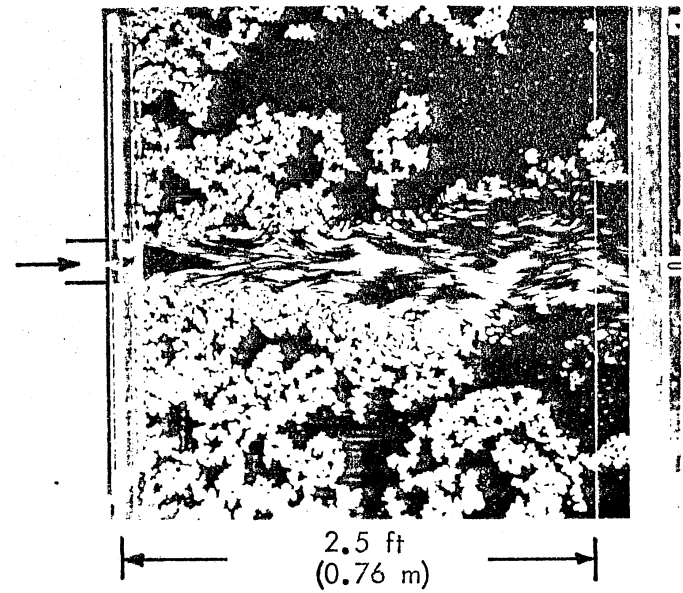
- a. Under isothermal conditions, the jet discharge has a tendency to meander slightly around the main trajectory. This phenomenon is caused by the vortex shedding in the free shear zone and is more apparent for outlet channels of small aspect ratio than for those of wide aspect ratio; increased buoyancy of the discharge seems to suppress the phenomenon. The meandering phenomenon was also mentioned by Jen, Wiegel, and Mobarek¹¹.
- b. Under isothermal conditions, fluid particles entrained on the tank surface reach the center of the jet regardless of aspect



$F_o = 3.3$



$F_o = 7.1$



$F_o = \infty$

Fig. 10a - Streaklines illustrating surface flow patterns - $A = 1.0$, $R = 0$, Exposure = 1/10 sec

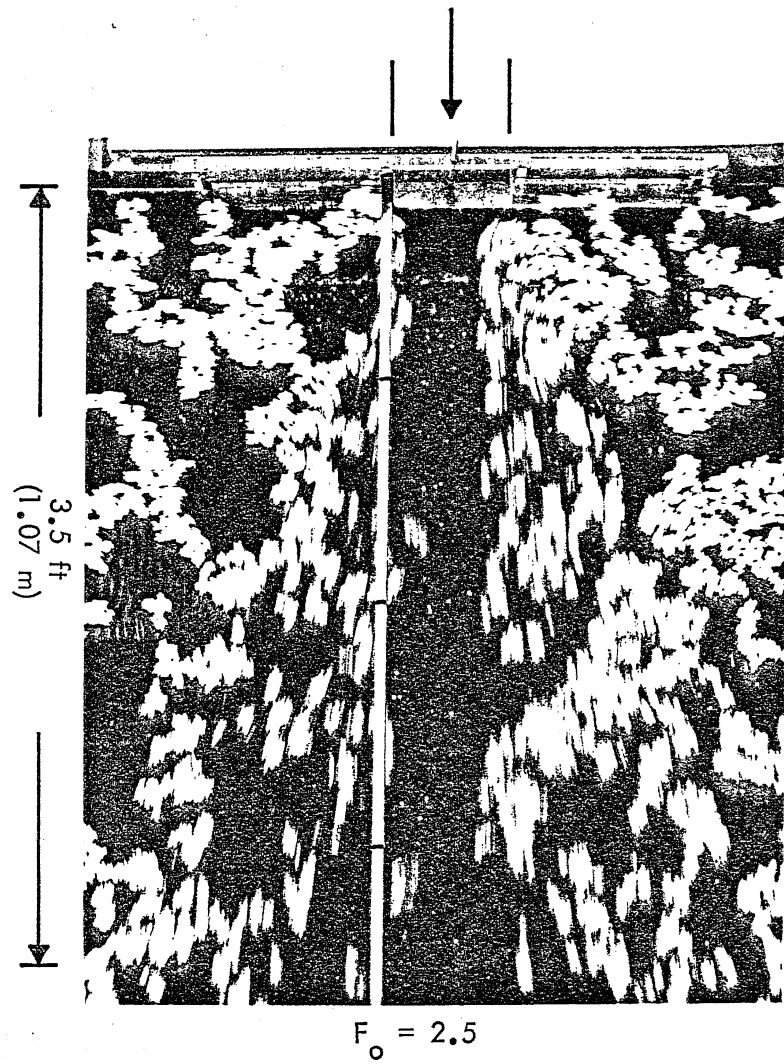
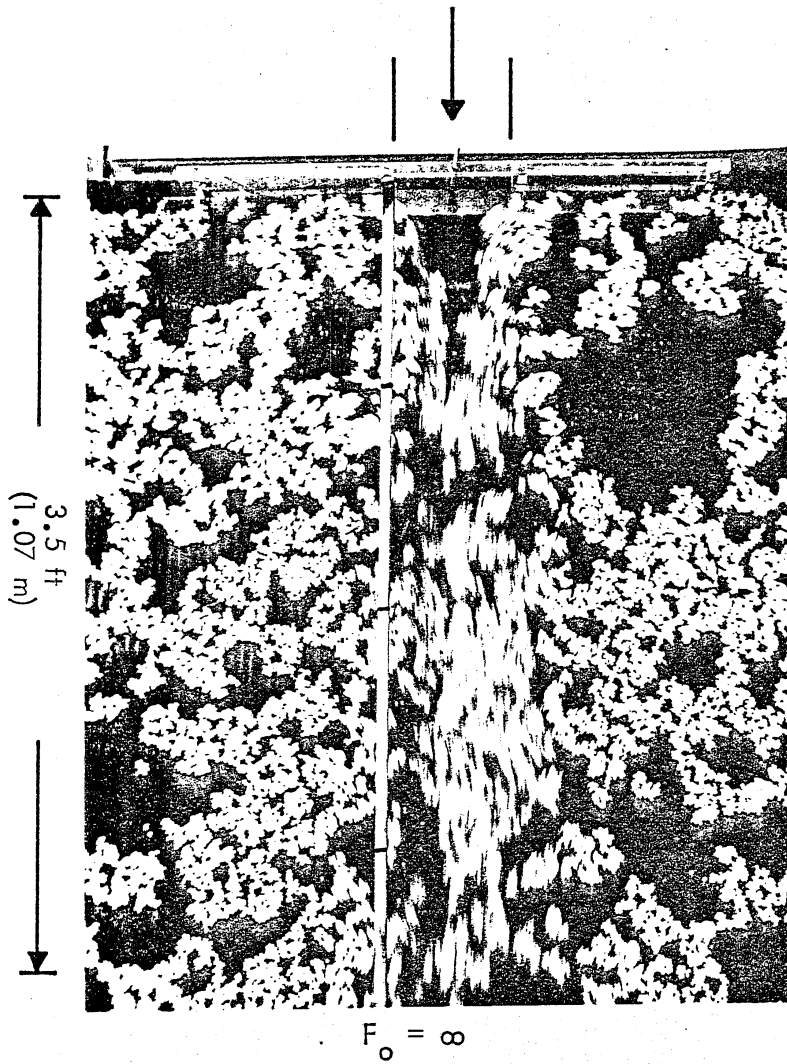


Fig. 10b - Streaklines illustrating surface flow patterns - $A = 2.4$, $R = 0$, Exposure = $1/5$ sec
(yardstick with distance markers suspended above water surface)

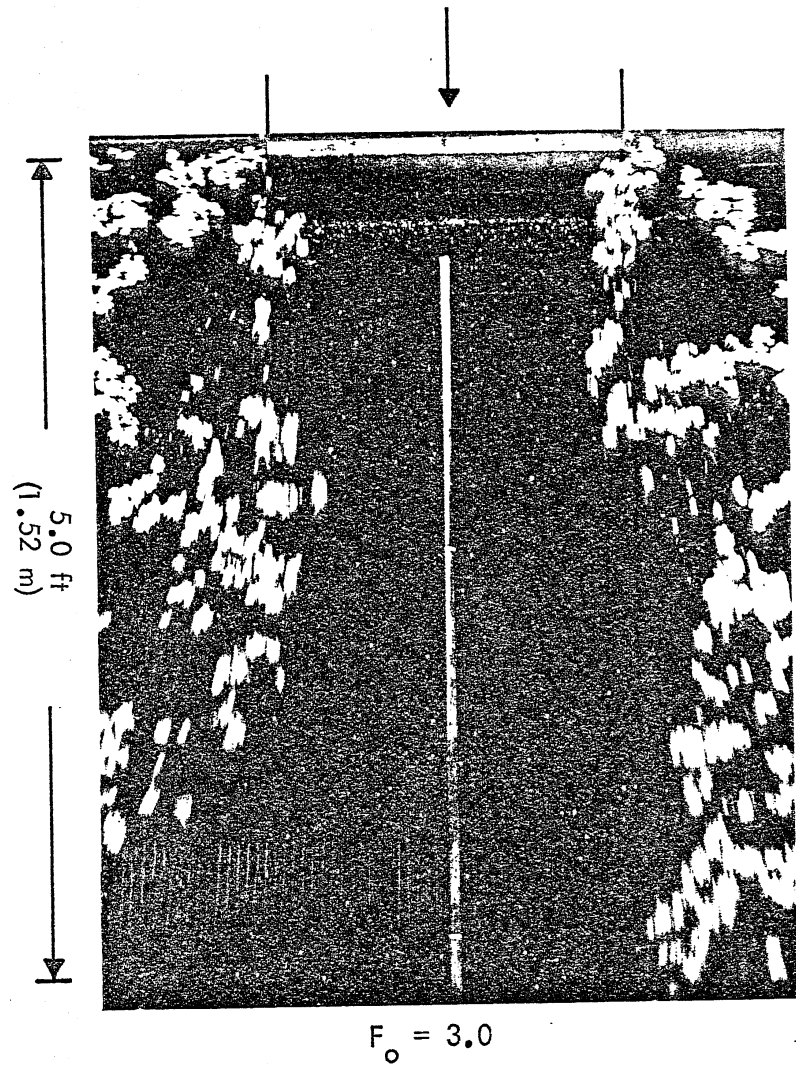
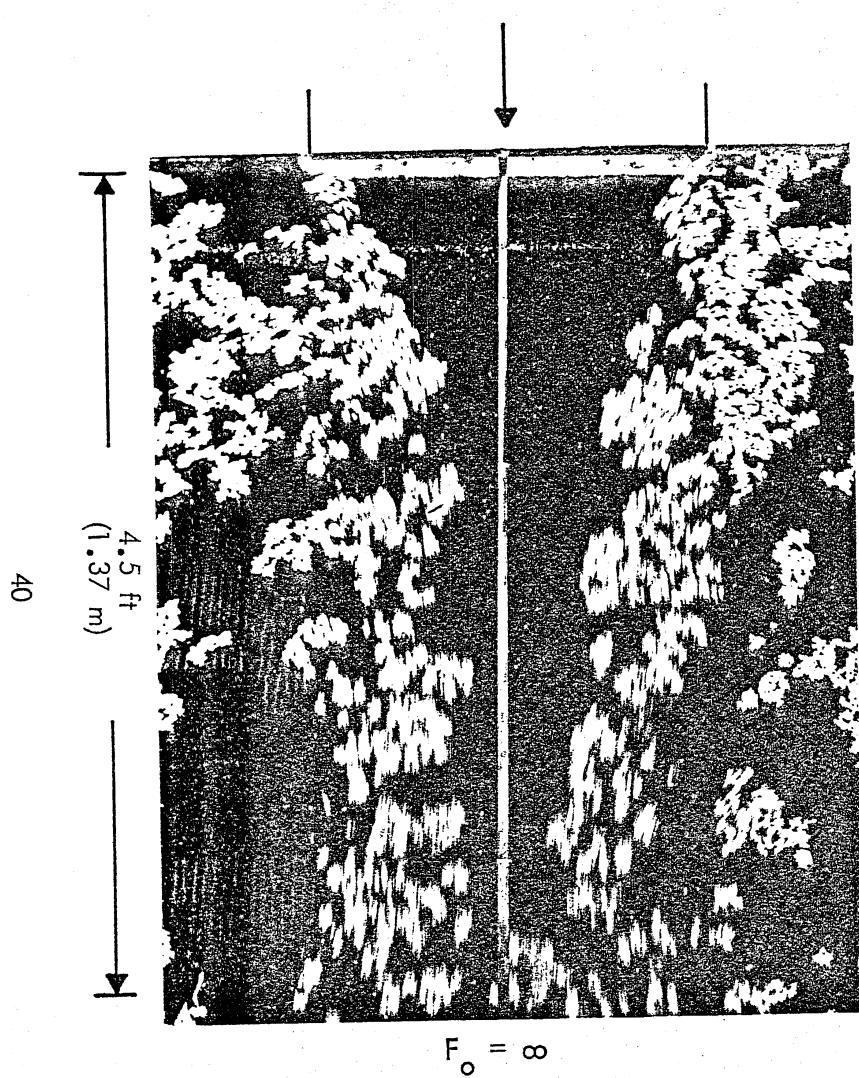


Fig. 10c - Streaklines illustrating surface flow patterns - $A = 9.6$, $R = 0$, Exposure = $1/5$ sec at $F = \infty$ and $1/10$ sec at $F = 3.0$ (yardstick with distance markers suspended above water surface)

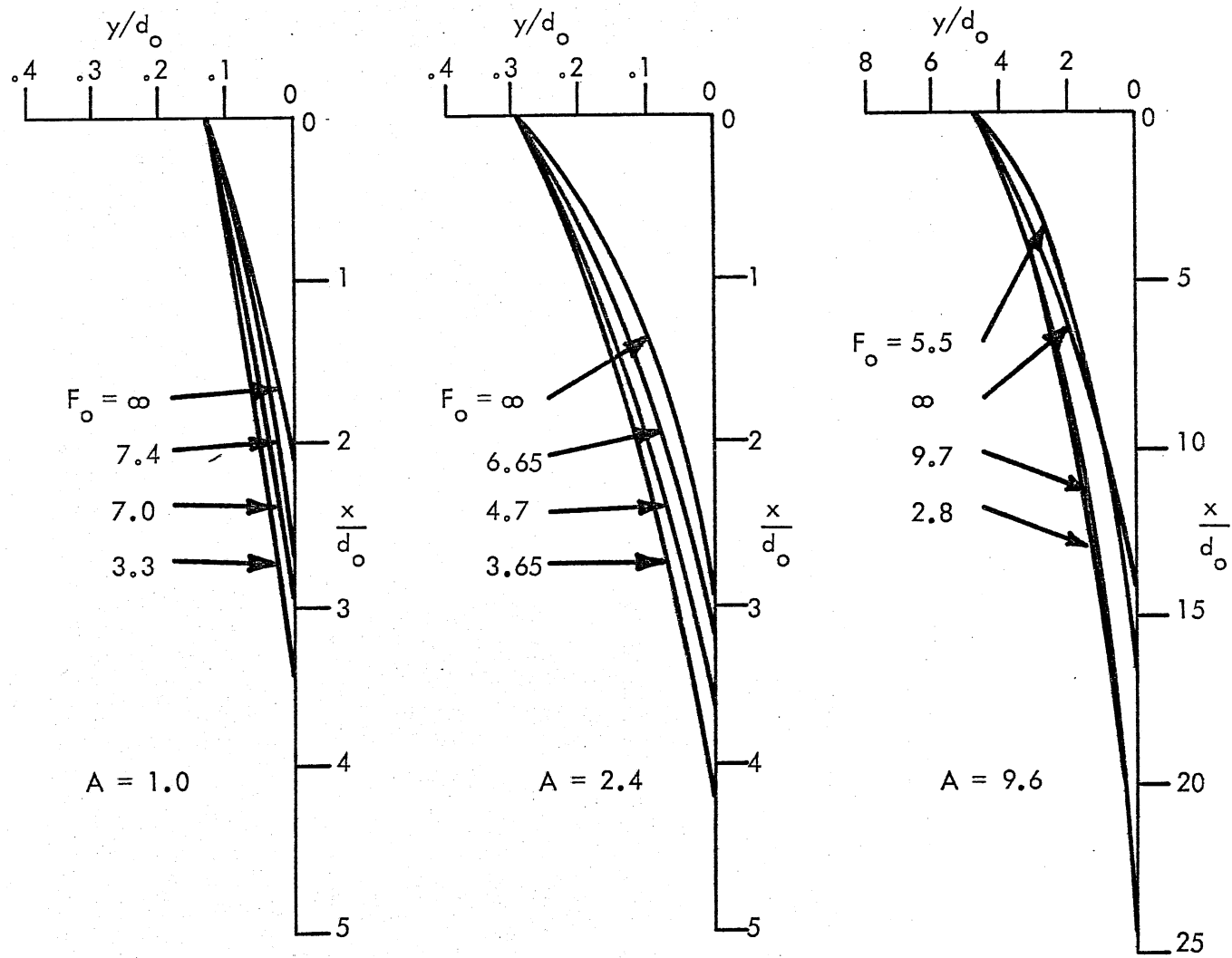


Fig. 11 - Boundaries of visible core region for $A = 1.0, 2.4,$ and 9.6 and various F_o

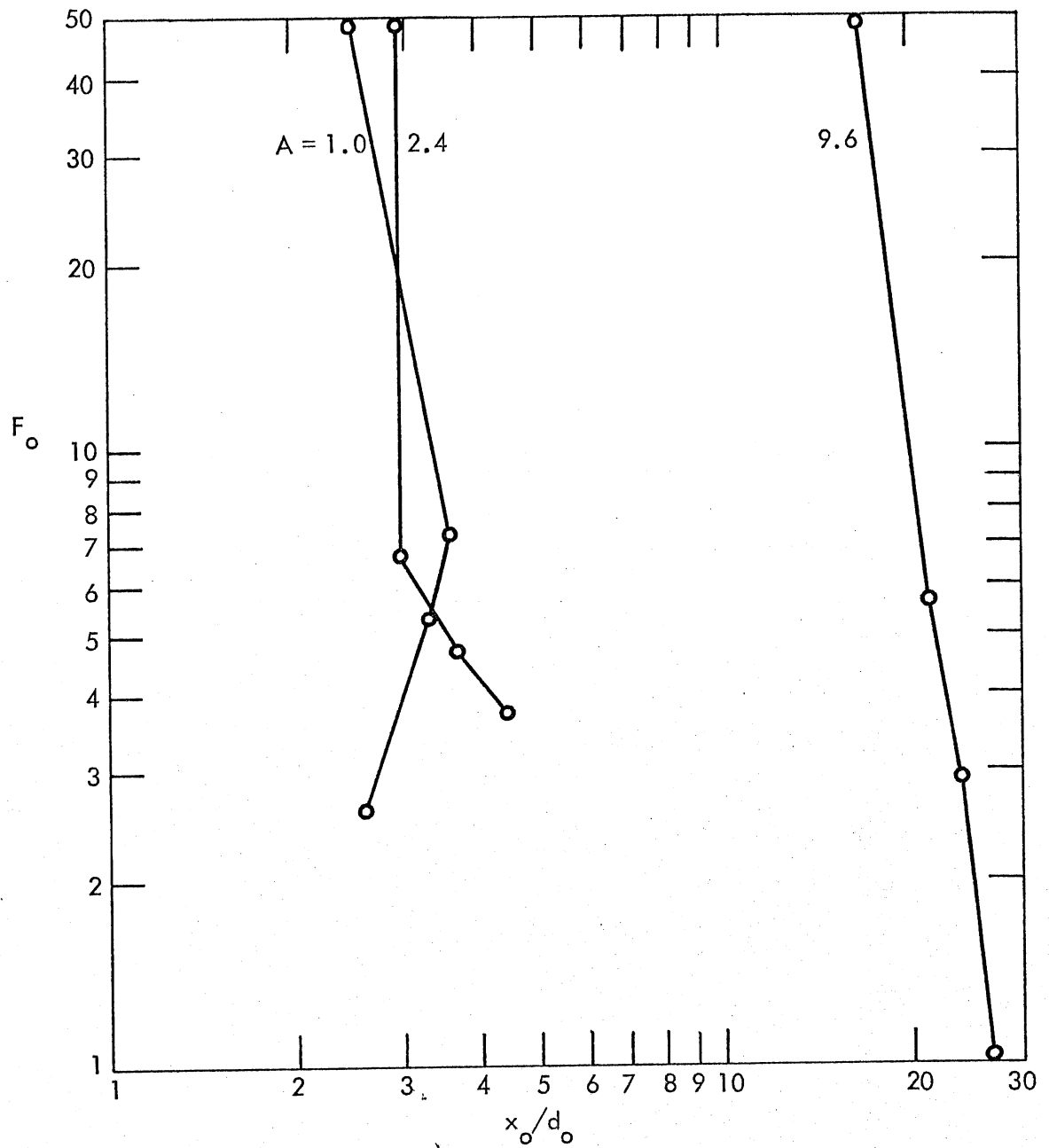


Fig. 12- x_o/d_o versus F_o at $A = 1.0, 2.4,$ and 9.6 as determined from photographs of surface tracers

ratio. This does not mean, however, that the point of convergence marks the end of the ZFE.

- c. When Froude numbers F_o are as low as 2 or 3, fluid particles entrained from the tank surface do not reach the centerline of the jet; this implies that the end of the ZFE is not controlled by convergence of the lateral shear layers, but must be reached when the vertical shear layer reaches the water surface.
- d. Lateral entrainment velocities have a "pinching effect" on the jet discharge near the outlet, apparently resulting in faster convergence of the surface-entrained particles; the pinching effect is caused by the jet-generated momentum of the laterally entrained flow, and it is more apparent for the wide channel than for the narrower one.

Approximate boundaries of the visual (surface) core region as derived from the photographs are shown in Fig. 11. A normalized representation is given. Each line is an average based on three to five instantaneous pictures. Changes that occur in the visual core length are consistent with Froude number, but are not proportional to the width of the outlet channel. The buoyancy effect appears to be much stronger for the narrow channel than for the wide one. For the narrower channels the visible core region seems to be independent of width. This is illustrated more directly in Fig. 12. The dependency on aspect ratio appears to be much stronger than that on Froude number.

Water Temperature Data

Time-Averaged Water Temperatures--Time-averaged water temperatures or velocities measured along the axis of the jet (on the surface of the tank) decline gradually with distance from the point of discharge. Figure 13 gives an illustration of the effect of Froude number on the temperature distribution. Data similar to those of Fig. 13 have previously been reported in the literature by several experimenters. A type of summary was provided by Dormhelm, Nouel, and Wiegel⁹. Figure 13 shows normalized excess

117

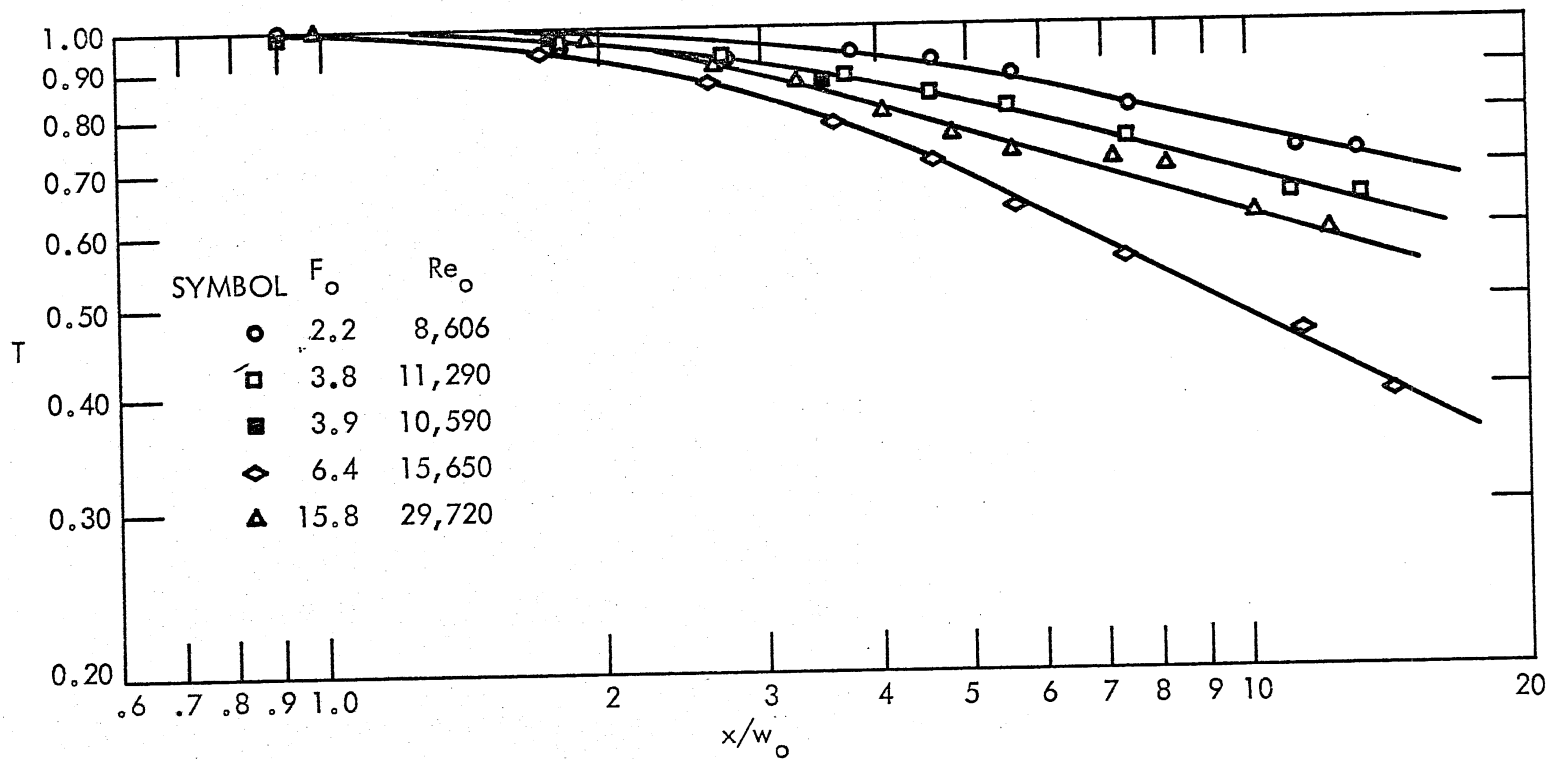


Fig. 13 - Sample of time-averaged water temperatures along jet axis - $A = 2.4$, $F_o = 2.2, 3.8, 3.9, 6.4, \text{ and } 15.8$

temperature T versus normalized distance, x_0/w_0 . The plot given is useful for illustrating a number of points, including the following:

- a) It is difficult to find the length of the ZFE by extrapolating backwards from the initial temperature decline curve.
- b) An excess temperature concentration value between 0.98 and 0.80 can be chosen arbitrarily to define the length of the ZFE; it can be seen that it is easy to commit major errors in doing this.

Values of x_0/d_0 derived for different values of T are given in Figs. 14a, b, c, and d for aspect ratios of 1.0, 2.4, 4.8, and 9.6 respectively. The results can be interpreted as follows:

There exist two virtually opposite effects of buoyancy on the length of the ZFE:

- a) The buoyancy-induced spread of the plume (illustrated in Fig. 9) is associated with outward velocities which prevent the horizontal convergence of the shear layers and thereby lengthen the ZFE.
- b) The buoyancy-induced lateral spread of the plume also reduces the depth of the plume and brings the vertical shear layer closer to the surface, thereby promoting the shortening of the ZFE.

Figures 14a through d show that effect (a) typically appears at $F_0 > 5$; effect (b) seems to be dominant at $F_0 < 4$. There is also some dependency on aspect ratio; for example, at $A = 1$, effect (b) seems to be particularly strong.

The above statements can be carried one step further by saying that the length of the ZFE seems to be controlled primarily by the growth of the vertical shear layer regardless of F_0 values except when the aspect ratio is small ($A < 2$). The effect of the aspect ratio on the ZFE is shown explicitly in Figs. 15a, b, and c. The trend from an aspect ratio of 1 to 4.8 to 9.6 is fairly consistent. For a reason unknown to the authors, it was more difficult to obtain consistent data for $A = 2.4$

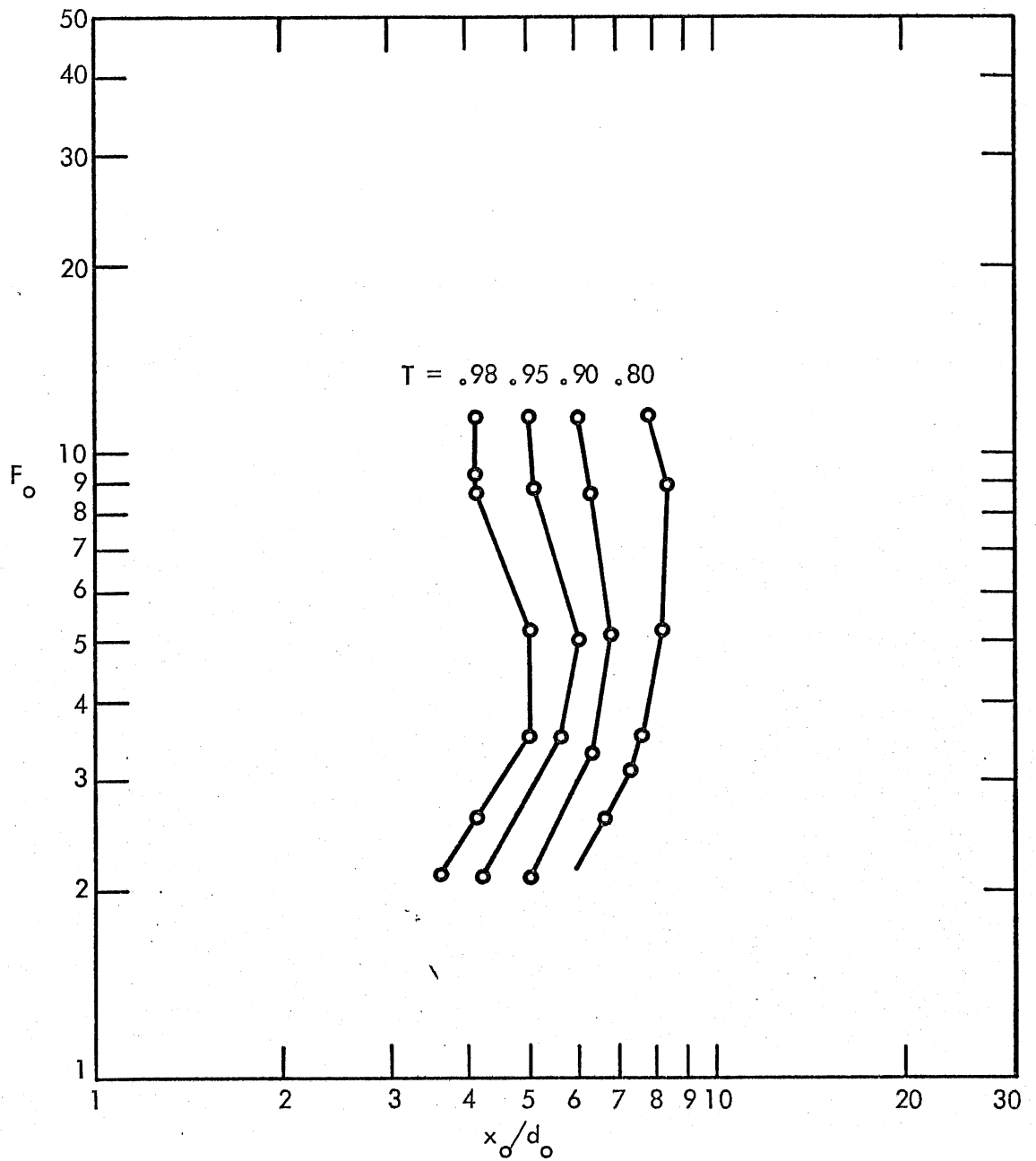


Fig. 14a - x_o/d_o versus F_o at $T = 0.98, 0.95, 0.90,$ and 0.80 ;
 $A = 1.0, R = 0$

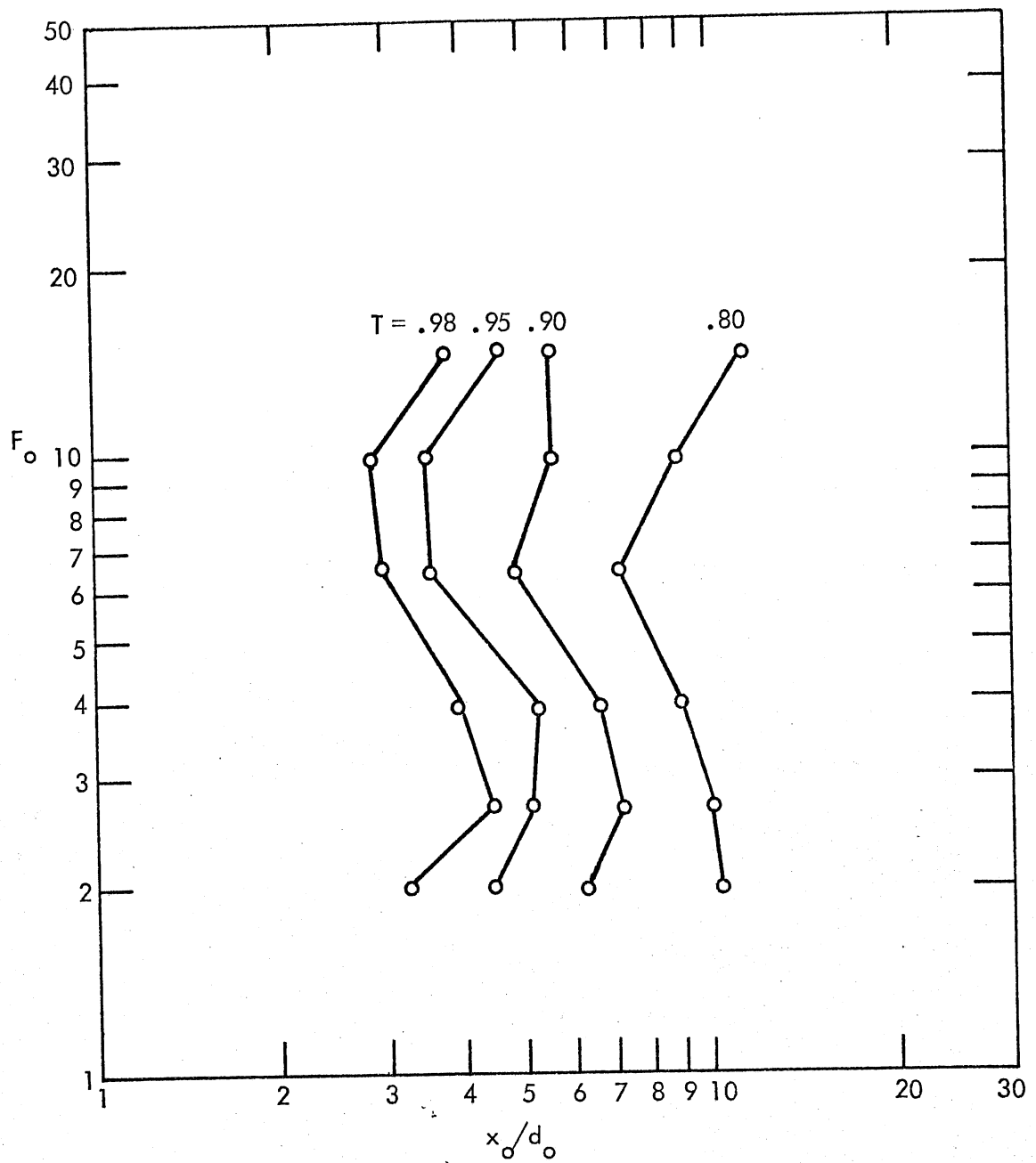


Fig. 14b - x_o/d_o versus F_o at $T = 0.98, 0.95, 0.90,$ and 0.80 ;
 $A = 2.4, R = 0$

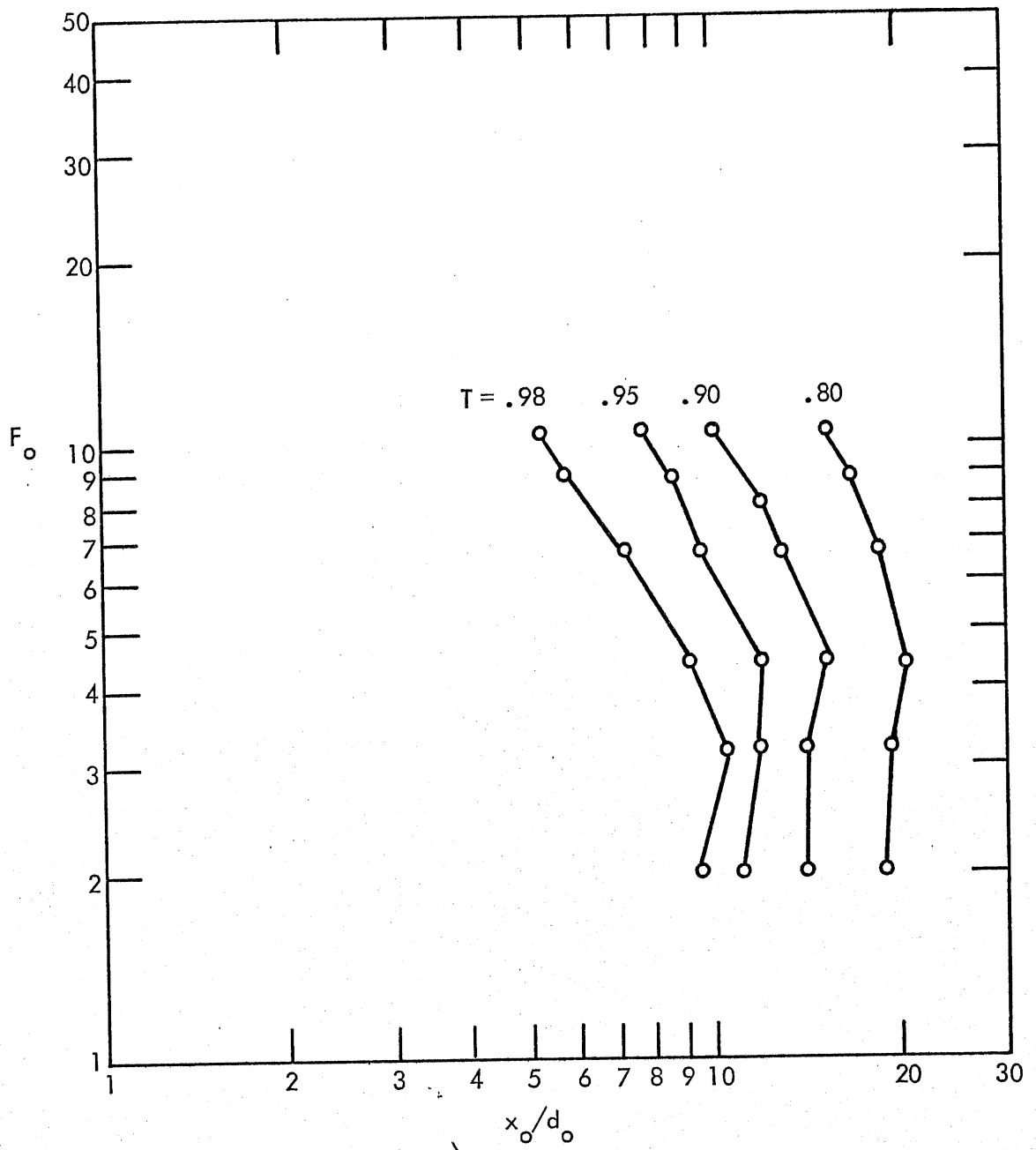


Fig. 14c - x_o/d_o versus F_o at $T = 0.98, 0.95, 0.90,$ and 0.80 ;
 $A = 4.8, R = 0$

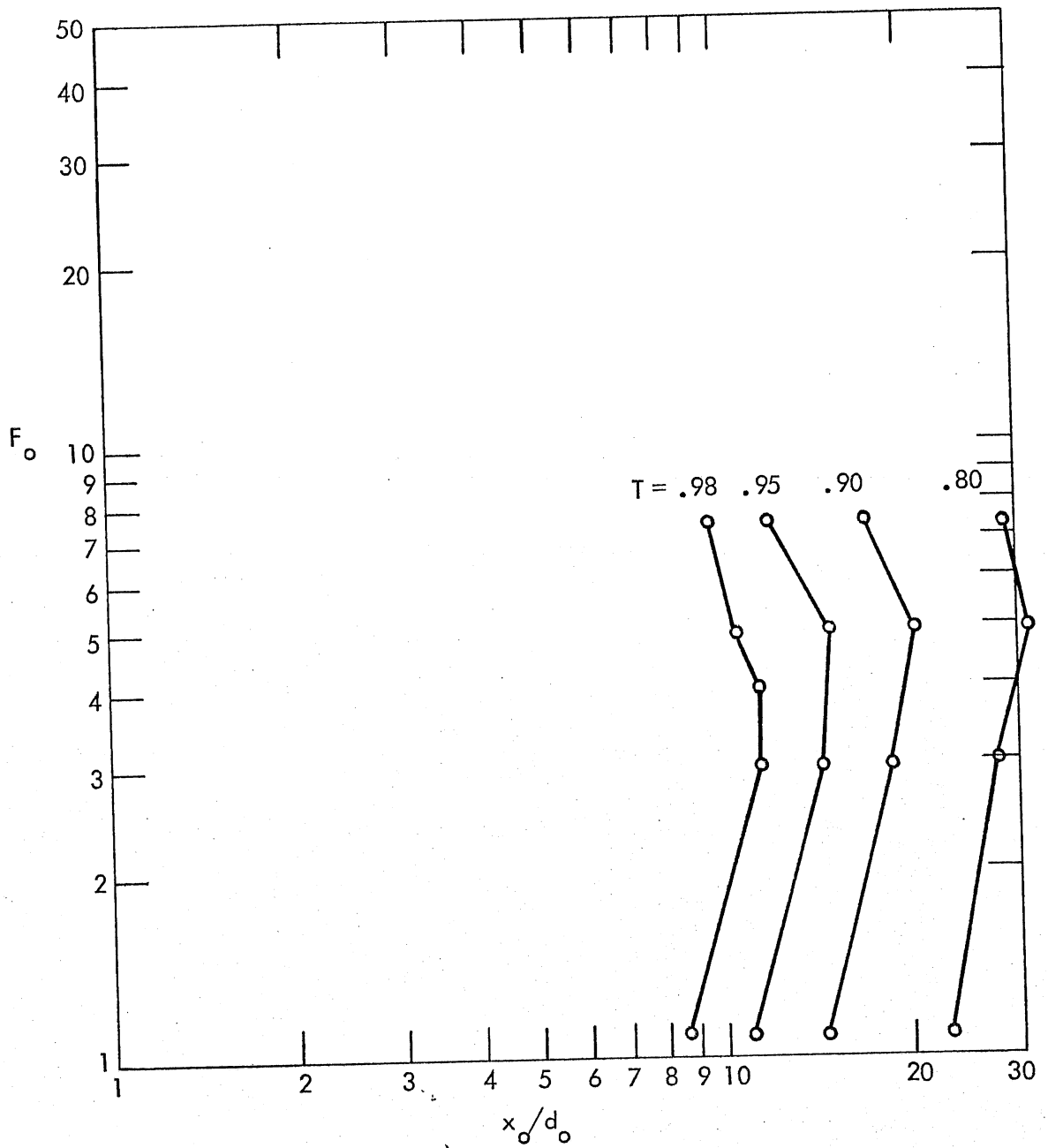


Fig. 14d - x_o/d_o versus F_o at $T = 0.98, 0.95, 0.90,$ and 0.80 ;
 $A = 9.6, R = 0$

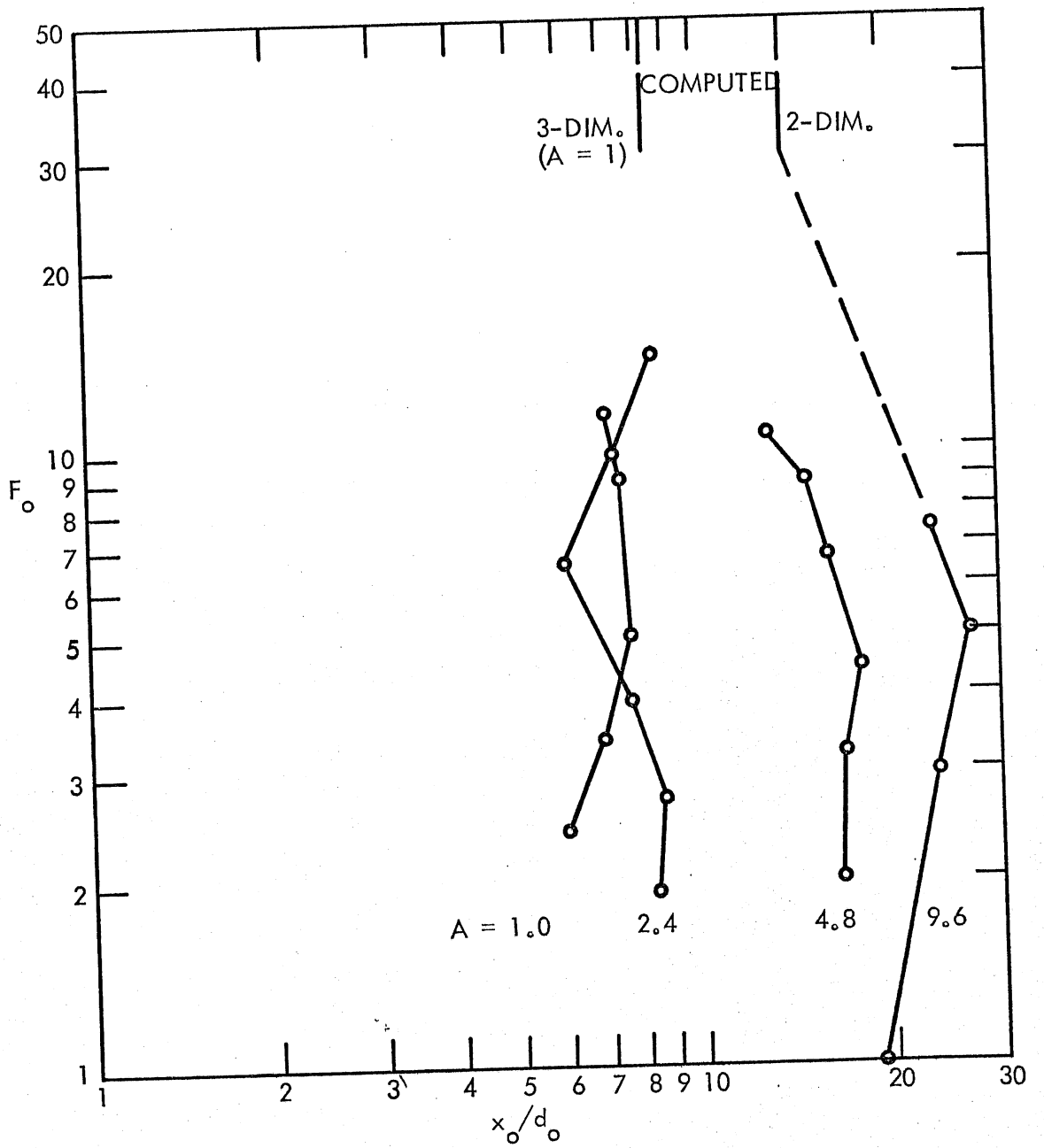


Fig. 15a - x_o/d_o versus F_o at $T = 0.85$; $A = 1.0, 2.4, 4.8,$ and 9.6 ; and $R = 0$

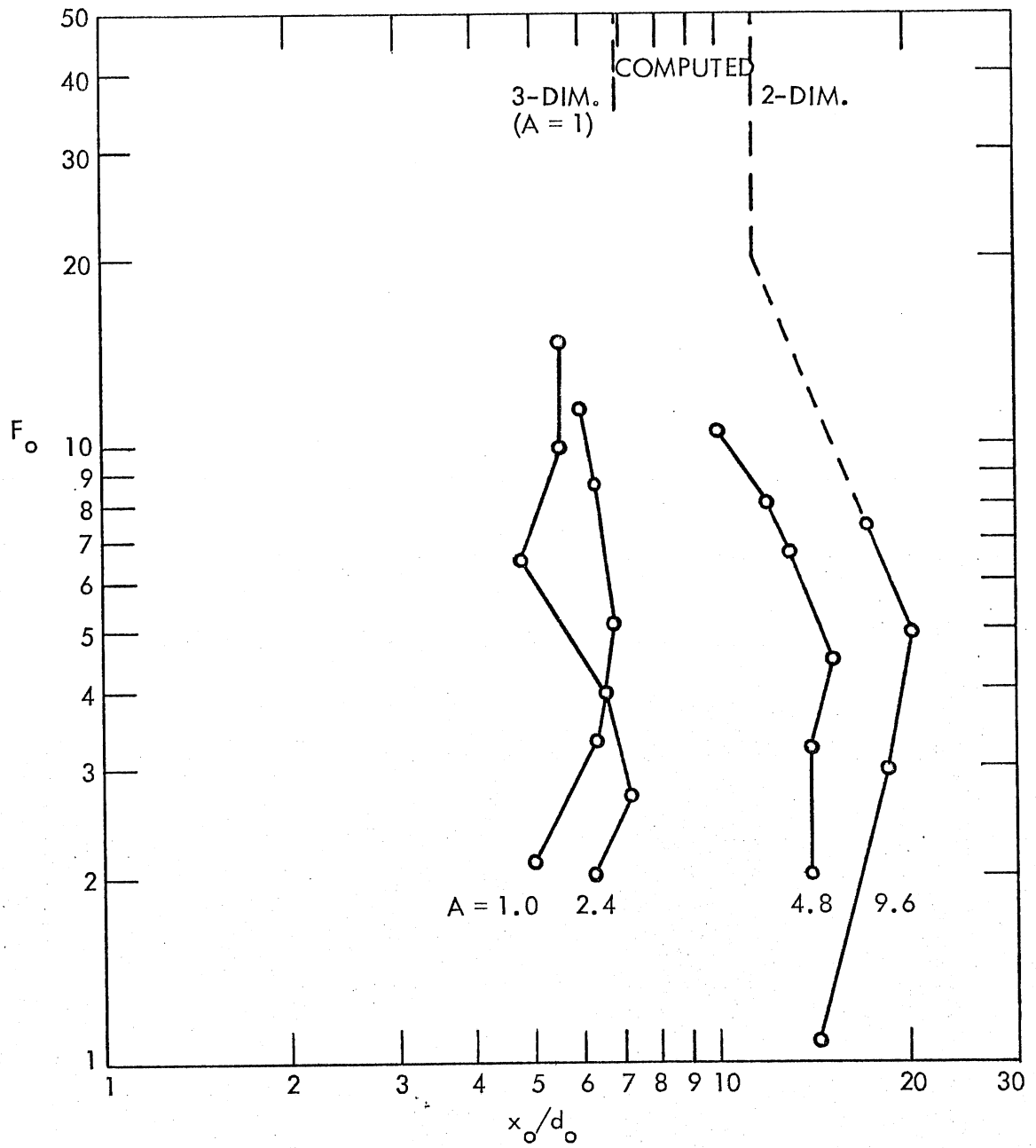


Fig. 15b - x_0/d_0 versus F_0 at $T = 0.90$; $A = 1.0, 2.4, 4.8,$ and 9.6 ; and $R = 0$

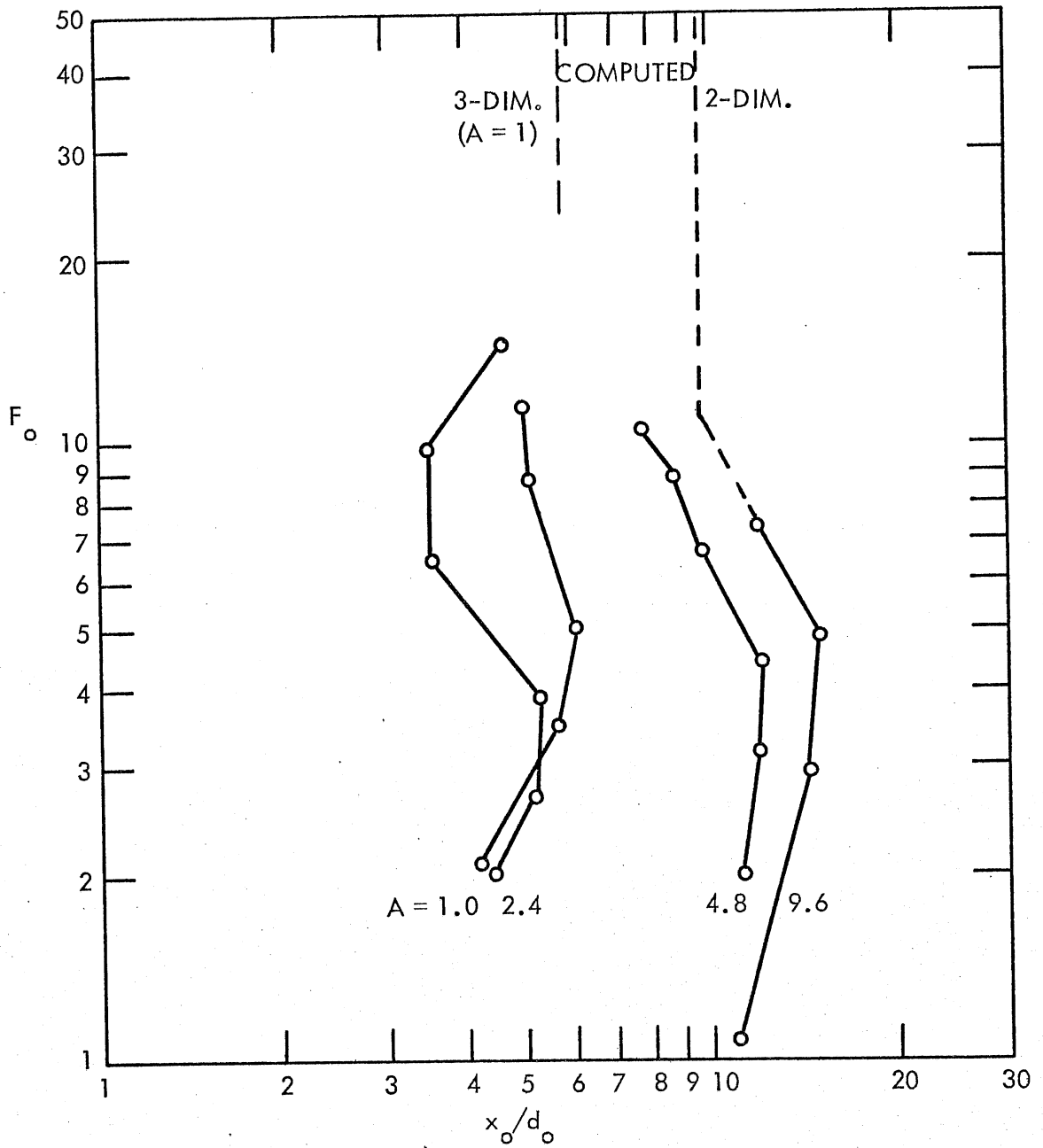


Fig. 15c - x_0/d_0 versus F_0 at $T = 0.95$; $A = 1.0, 2.4, 4.8,$ and 9.6 ; and $R = 0$.

than for any other value of A . This is indicated by the standard deviations of the x_o/d_o values given in Table 1. A strong secondary motion causing upwelling along the centerline of the jet relatively close to the outlet seemed to be one possible source of the peculiarity.

Table 1. STANDARD DEVIATIONS OF x_o/w_o and x_o/d_o
AS GIVEN IN FIGURES 14a, b, and d

Aspect Ratio	$A = 1$	2.4	9.6
Standard Deviation	$\left\{ \begin{array}{l} \sigma(x_o/w_o) = 0.60 \\ \sigma(x_o/d_o) = 0.60 \end{array} \right.$	0.77	0.172
		1.85	1.72

How do the results of Figs. 14 and 15 compare with those for non-buoyant, circular, fully submerged jets? There are three main differences between the flows leading to the results of Figs. 14 and 15 and the non-buoyant, circular, fully submerged jets investigated, for example, by Albertson, Dai, Jensen, and Rouse⁶: (1) initial jet shape; (2) buoyancy; and (3) free surface.

To relate circular and non-circular jets one might use the hydraulic diameter as shown in Table 2. The Albertson, et al., definition of x_o for three-dimensional jets corresponds approximately to the 85 per cent value of their measured velocity concentration, and their definition for two-dimensional jets corresponds approximately to the 90 per cent value. Comparisons must therefore be made at those concentration levels. A comparison of non-buoyant and buoyant jet results (based on time-averaged temperatures) after elimination of shape effects is given in Table 3. The results are also incorporated in Fig. 15.

As the buoyancy decreases in significance, values of x_o/d_o tend toward the values given in the second column of Table 3. Buoyancy appears to reduce the length of the ZFE when the aspect ratio is small ($A \leq 3$) and to lengthen the ZFE when the aspect ratio is large ($A \geq 3$). The greatest lengthening effect appears at F_o values in the vicinity of 5. By extrapolation as shown in Fig. 15a it is found that

Table 2. ESTABLISHMENT LENGTHS x_o COMPUTED FOR NON-BUOYANT, FULLY SUBMERGED JETS (after Albertson, et al.⁶)

For a two-dimensional, non-buoyant jet, $\frac{x_o}{2d_o} = 5.2$

For a three-dimensional, non-buoyant, axisymmetric jet, $\frac{x_o}{D_o} = 6.2$

applied to rectangular channels of different aspect ratios A ,

$A = 1.0$: $D_h = \frac{4d_o}{3}$ $\frac{x_o}{d_o} = 8.3$

$A = 2.4$: $D_h = 2.18 d_o$ $\frac{x_o}{d_o} = 13.5$

$A = 9.6$: $D_h = 3.2 d_o$ $\frac{x_o}{d_o} = 19.8$

The limiting aspect ratio at which $x_o/d_o = 10.4$ for both two- and three-dimensional jets is $A = 1.44$.

Table 3. COMPARISON OF COMPUTED AND MEASURED x_o/d_o VALUES

<u>A</u>	<u>x_o/d_o</u>		<u>T</u>	
	Computed Non-Buoyant	Measured Buoyant		
		<u>Max.</u>	<u>Min.</u>	
1.0	8.3 (three-dimensional)	7.4	5.4	0.85
2.4	10.4 (two-dimensional)	7.2	4.8	0.90
4.8	10.4 (two-dimensional)	15.2	10.3	0.90
9.6	10.4 (two-dimensional)	20.5	15.0	0.90

at approximately $F_o \geq 30$ the effects of buoyancy on the ZFE became negligible.

A more direct comparison of shape effects is possible using the results obtained with a semicircular outlet channel ($A = 2$), reported in Fig. 8a, and the data for the rectangular outlet channel ($A = 2.4$) reported in Fig. 14b. It is most intriguing to observe that the trends reported on the two graphs are opposites. Furthermore, the order of magnitude of the x_o/d_o values is significantly higher for the semicircular outlet than for the rectangular one. The buoyancy effect manifests itself for the semicircular outlet by reducing the length of the ZFE (minimum of x_o/d_o at $F_o = 3$); for the rectangular outlet, x_o/d_o has a maximum at $F_o = 3$. In attempting to resolve or explain this apparent discrepancy, one must consider (a) the definition of the Froude number in both cases and (b) the secondary currents.

For the semicircular channel d_o represents the maximum depth, whereas for the rectangular channel it is the average depth. Froude numbers for the semicircular channel should therefore be increased before comparisons are made. (The factor would be approximately 1.2.) The secondary motion referred to is documented only indirectly through plots such as those shown in Figs. A-7 and A-9, to be discussed later. The differences between Figs. 8a and 14b represent a shape effect other than that expressed through the aspect ratio A .

A comparison of Figs. 11 and 15 shows that surface tracers do not give a good indication of the length of the ZFE, because they rely primarily on the horizontal shear layer at the surface, whereas the length of the ZFE depends more strongly on the vertical shear layer.

At small aspect ratios the visually determined values of x_o are considerably lower than those found from time-averaged temperature data. At large aspect ratios the results are more similar.

Fluctuating Water Temperature Components--The standard deviation σ_T of the fluctuating water temperature component was computed from the record obtained at each point. The standard deviation was normalized in the

same way as the time-averaged water temperature measurements as defined in Eq. (6). The resulting dimensionless parameter δT was plotted in several formats.

Centerline values of δT versus x/d_o are given in Figs. 16a through 16d. The following observations were made:

- a. The background level of the water temperature fluctuations as determined by δT is less than one per cent in the core region of the discharge. This value is a measure of the accuracy with which water temperatures in the discharge channel were controlled by the heat exchanger-thermostat-buffer tank system.
- b. There is a gradual transition from the near isothermal core region to the region in which water temperature fluctuations are more significant. This reflects the presence of turbulent eddies penetrating from the free shear layer into the core region.
- c. Peak values of δT reached were on the order of 5 to 13 per cent. A dependence of peak values on outlet Froude number, but not on aspect ratio is apparent. Values of F_o between 2.0 and 3.0 consistently gave the lowest measured peak values of δT . In general terms this can be interpreted as the effect of increased stratification stability on turbulence.
- d. The point at which peak values of δT occur was generally found to be farther from the outlet when aspect ratios were large. This reflects a lengthening of the ZFE which is in accordance with earlier findings based on time-averaged temperatures.
- e. It should be remarked that results for aspect ratio $A = 2.4$ again showed a much larger spread of results at nearly identical F_o values than those for any other aspect ratio. No clear explanation for this phenomenon has been found, but it is suspected that it may

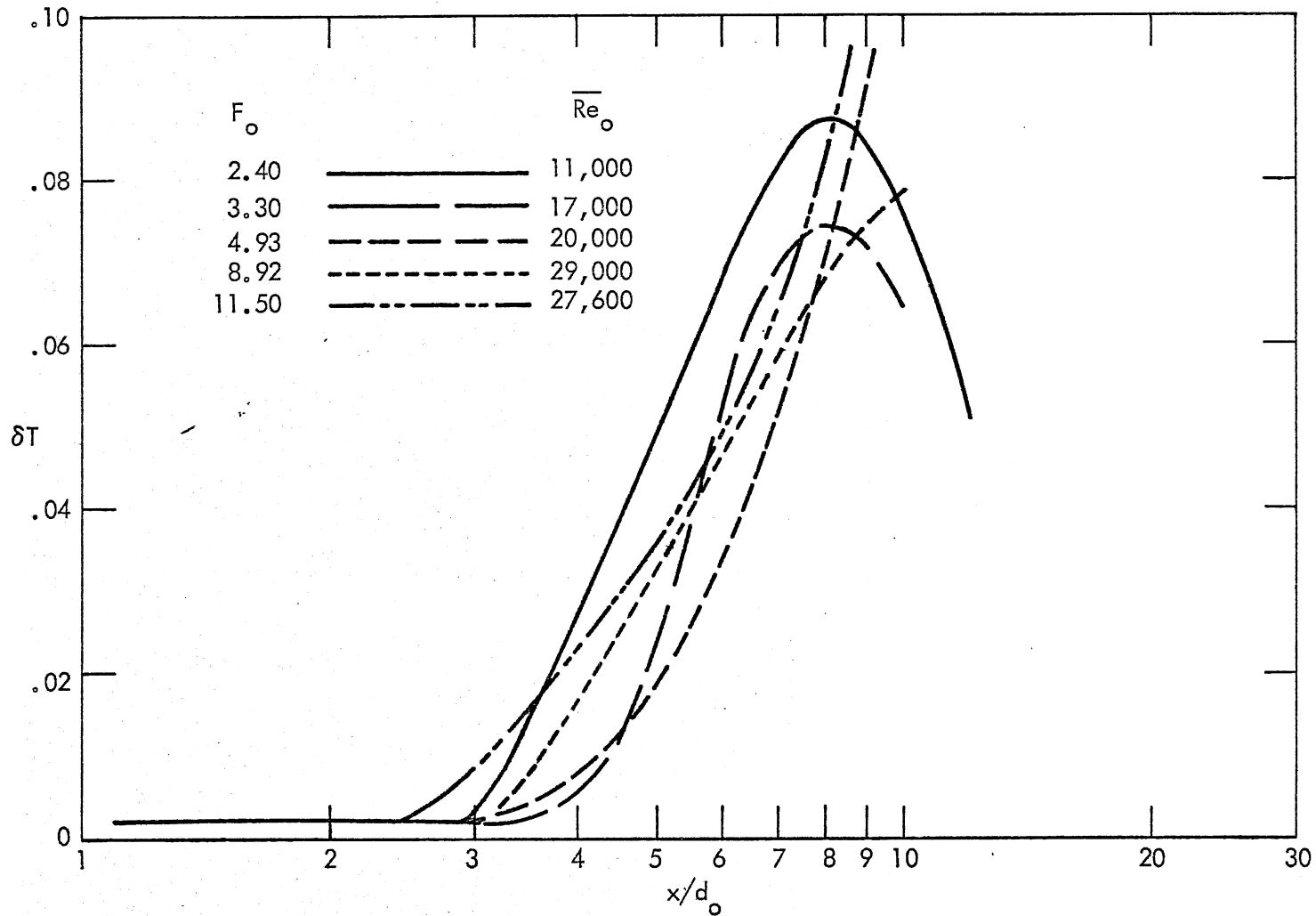


Fig. 16a - δT versus x/d_0 along jet axis at $A = 1.0$ and $R = 0$

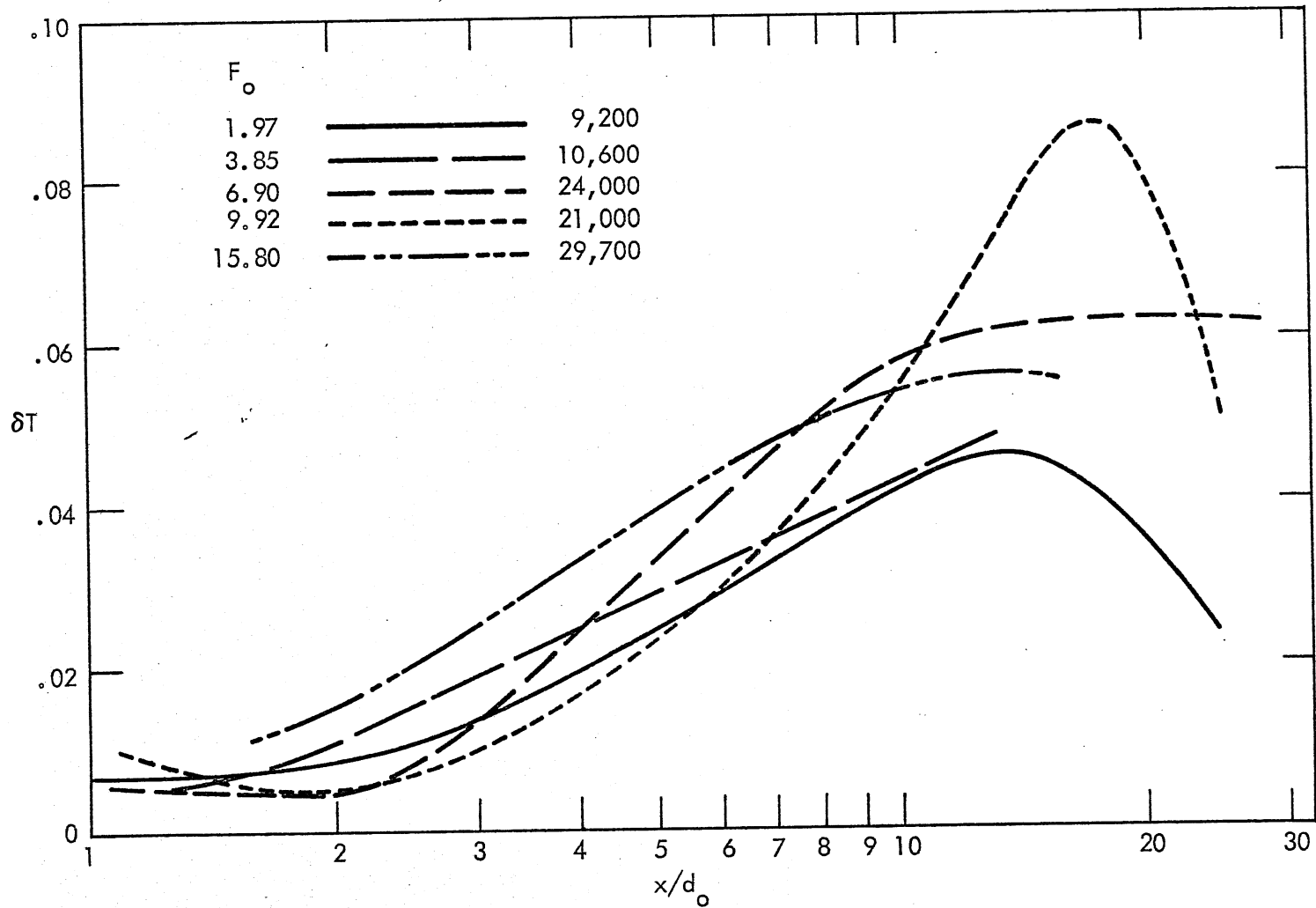


Fig. 16b - δT versus x/d_0 along jet axis at $A = 2.4$ and $R = 0$

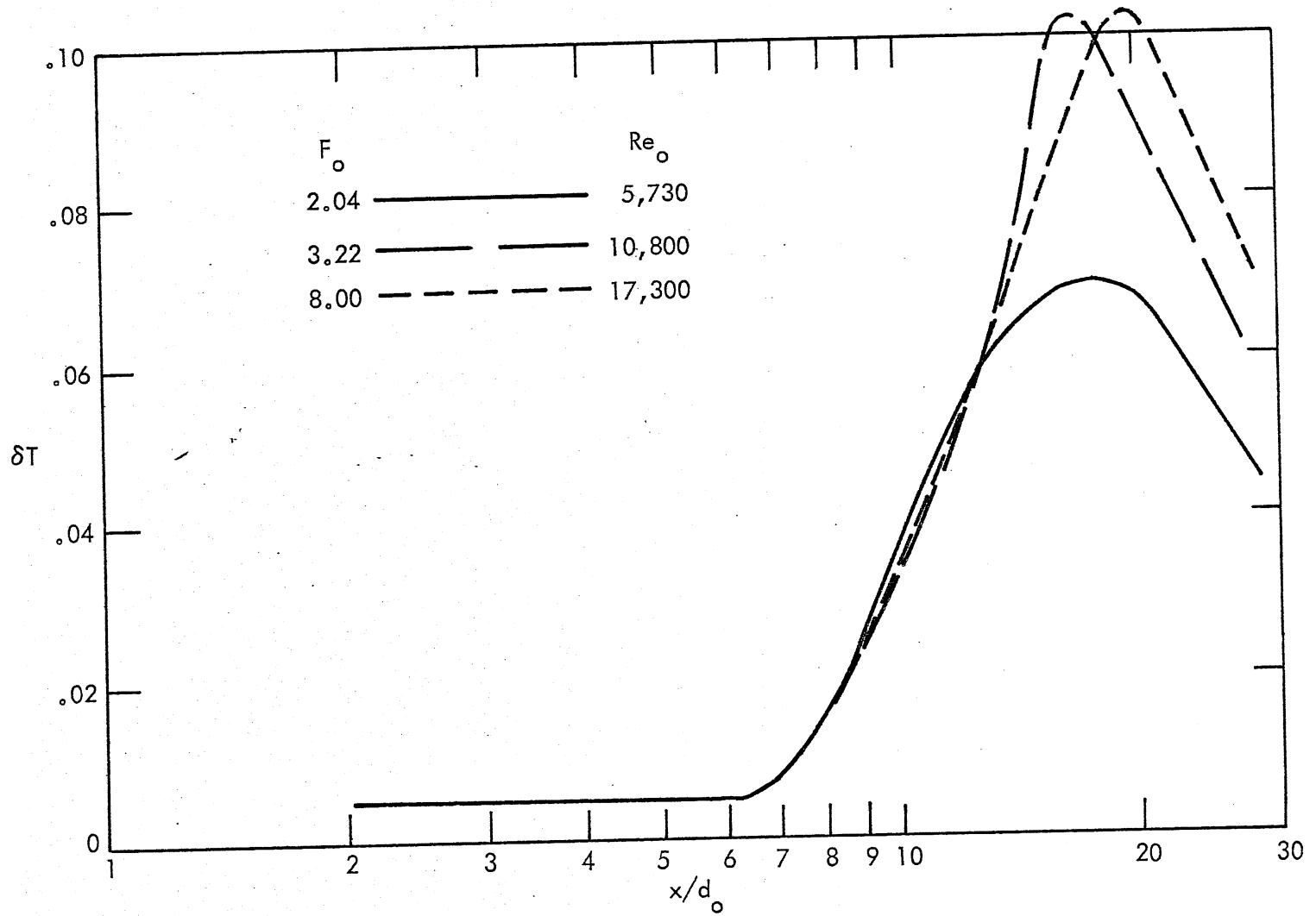


Fig. 16c - δT versus x/d_0 along jet axis at $A = 4.8$ and $R = 0$

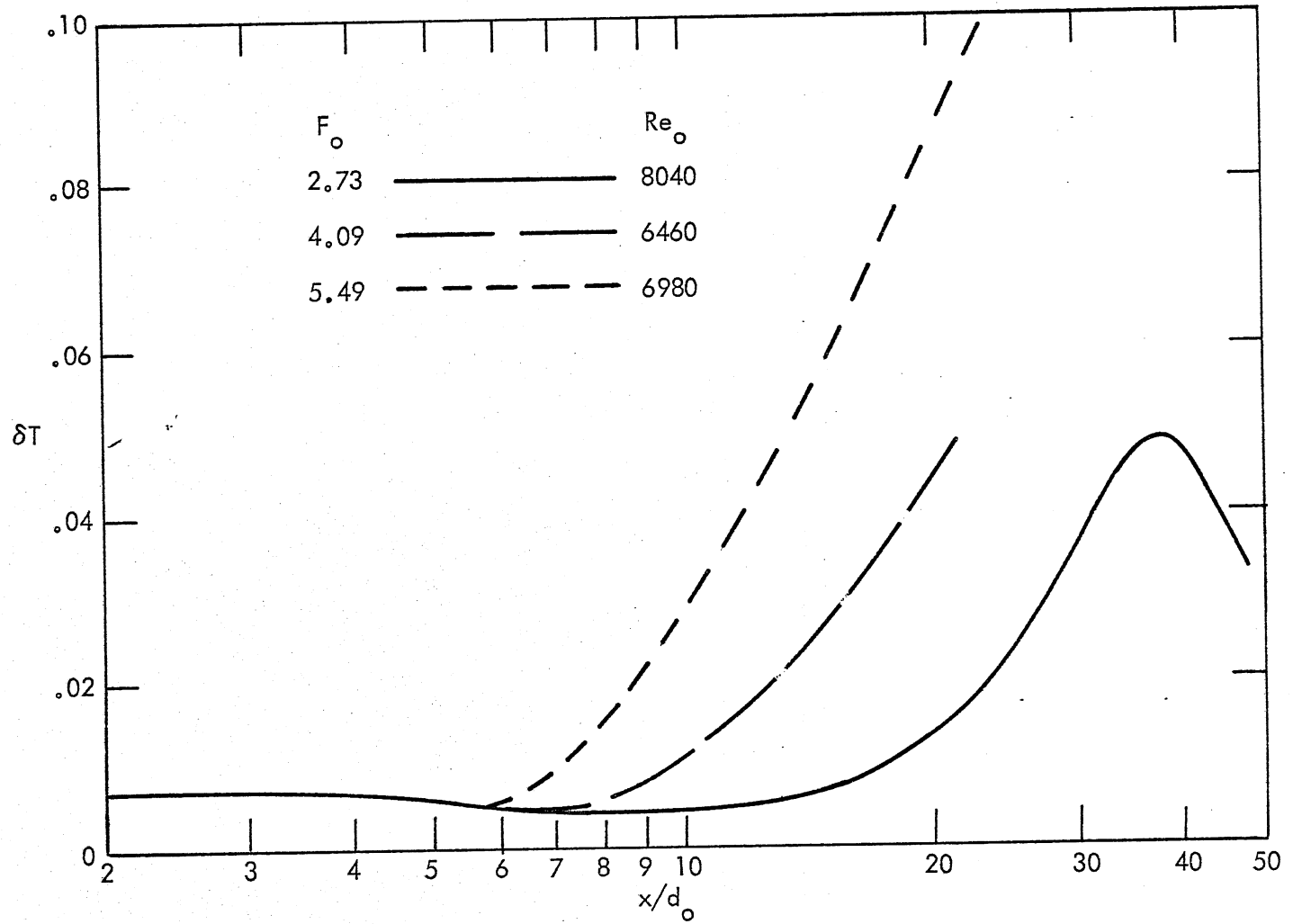


Fig. 16d - δT versus x/d_0 along jet axis at $A = 9.6$ and $R = 0$

be related to the secondary flow mechanism referred to previously.

The length of the ZFE was derived from Figs 16a through 16d by arbitrarily selecting the two and four per cent levels of δT . The results are accumulated in Figs. 17a and 17b. The significant features of the plots are

- a. the dependency of x_o/d_o on the aspect ratio at low Froude numbers;
- b. the possible existence of an upper envelope curve that encompasses all aspect ratios and Froude numbers.

Figures 15 and 17 both give lengths of the ZFE, but they are based on different definitions. Although the graphs are quite dissimilar, they show similarly strong effects of aspect ratios on x_o/d_o values. To establish a more direct relationship between Figs. 15 and 17, the T levels which would give the same values of x_o/d_o as were found at the $T = 0.85, 0.90,$ and 0.95 levels were determined. Average values of δT and T for all Froude numbers were used, and the results are given in Table 4. Through this table a relationship is established between the ZFE data derived from time-averaged temperatures and those derived from fluctuating components. The scatter of the results is represented by the standard deviation $\sigma_{\delta T}$ around the weighted mean for all aspect ratios. It is quite evident that the results from time-averaged and fluctuating temperatures correspond less consistently as the aspect ratio goes up.

Table 4. EQUIVALENT VALUES OF T and δT

A	T = 0.85		T = 0.90		T = 0.95	
	δT %	$\sigma_{\delta T}$ %	δT %	$\sigma_{\delta T}$ %	δT %	$\sigma_{\delta T}$ %
1.0	5.9	1.0	4.7	0.9	3.2	0.6
2.4	5.4	2.0	4.5	2.0	3.4	2.1
4.8	8.2	3.0	6.6	2.3	4.2	1.6
9.6	4.1	3.1	3.2	3.5	2.2	2.6

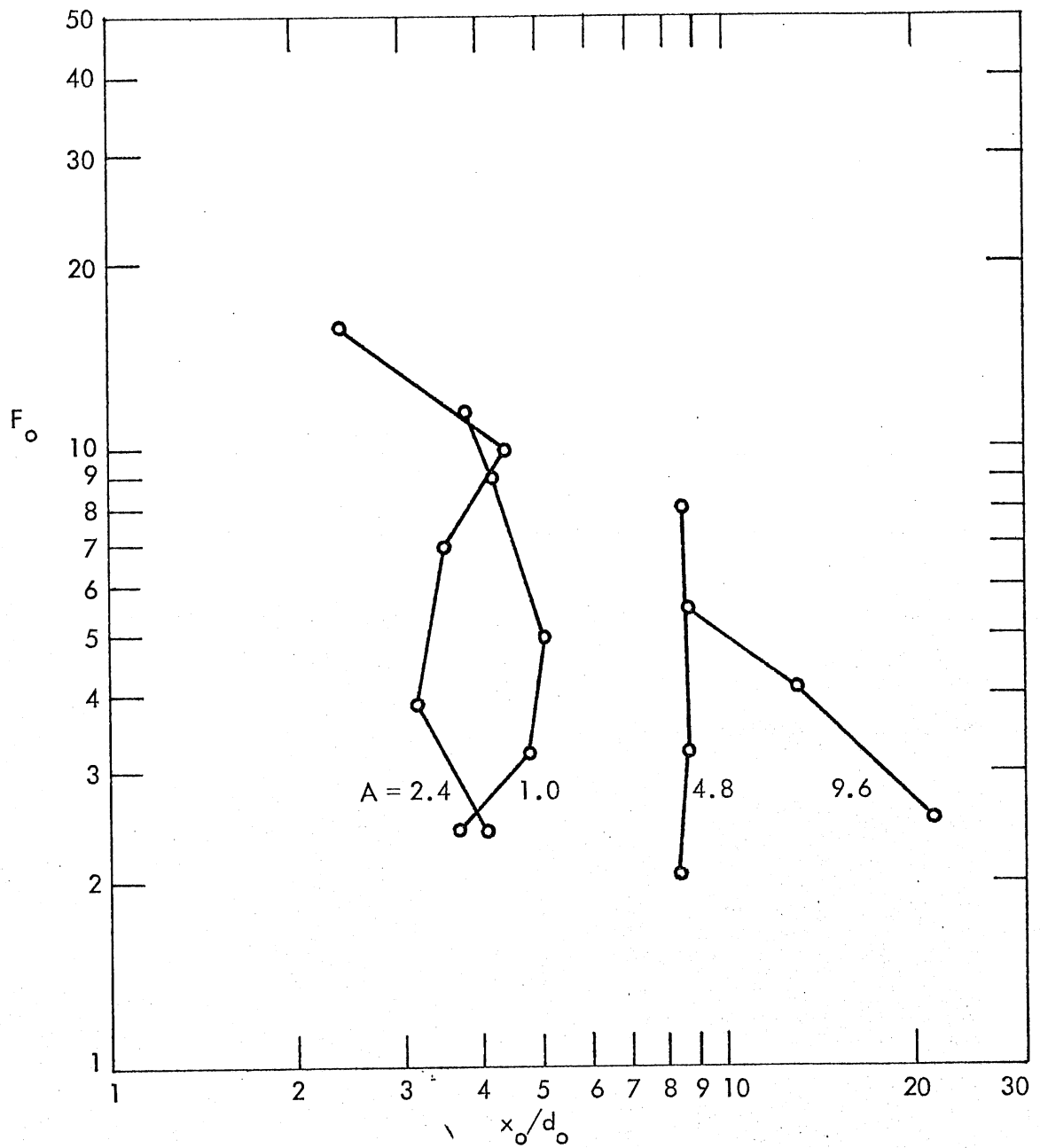


Fig. 17a - x_o/d_o versus F_o at $\delta T = 0.02$; $A = 1.0, 2.4, 4.8,$ and 9.6 ; and $R = 0$

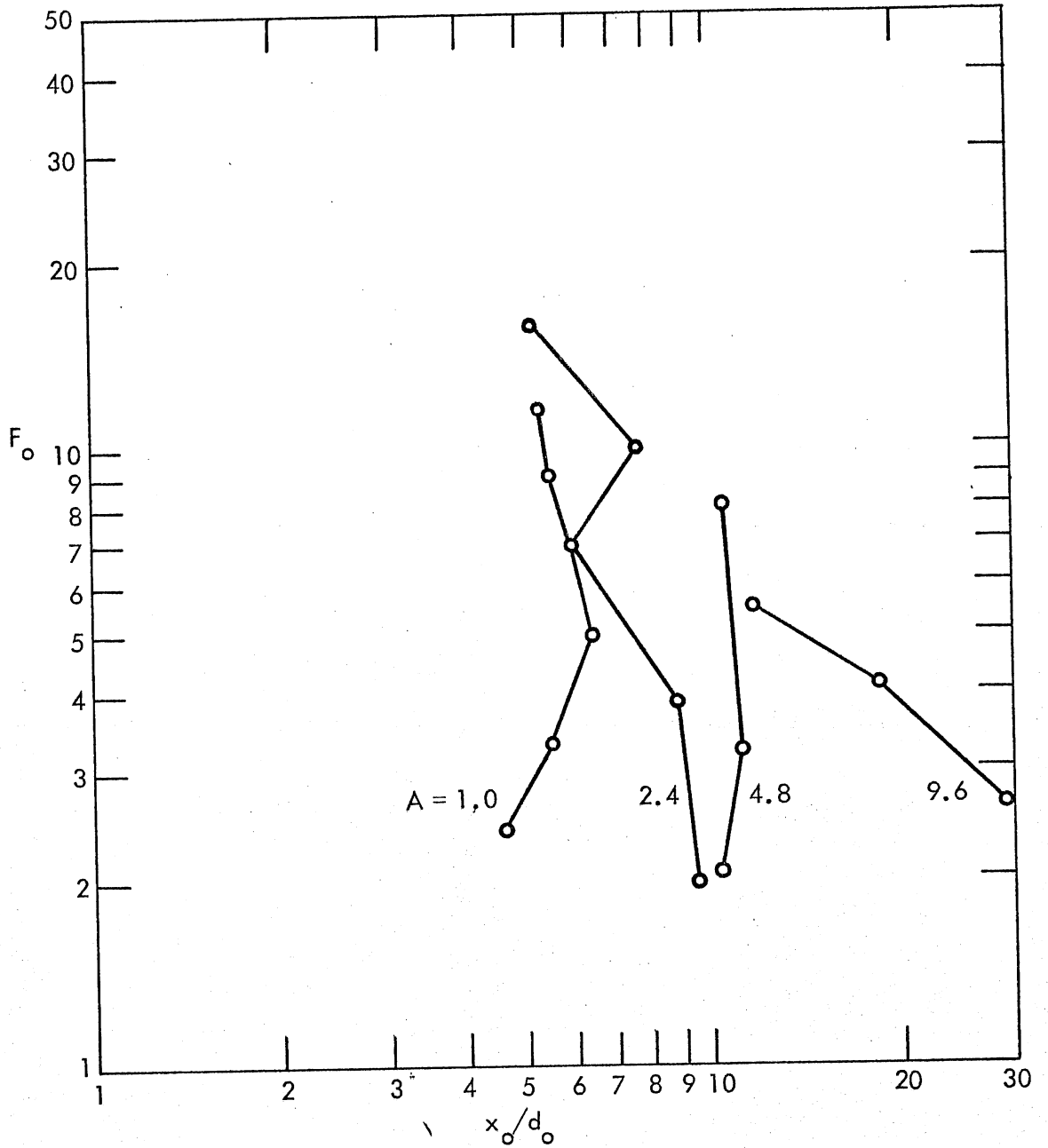


Fig. 17b - x_0/d_0 versus F_0 at $\delta T = 0.04$; $A = 1.0, 2.4, 4.8,$ and 9.6 ; and $R = 0$

Measurements of the fluctuating water temperature components are also useful for showing the entrainment and mixing mechanisms near the outlet. To obtain this information, water temperature profiles were measured not only along the centerline of the jet, but also in two or three cross sections perpendicular to it. Although it is possible to present only a selection from the data obtained, the following observations merit being listed and illustrated:

- a. The lateral spreading and mixing by large eddies formed in the free shear layer between the discharged jet and the ambient stagnant water appears to be more or less independent of the aspect ratio, as was inferred previously from visual observations of spreading angles (Fig. 9). Figures 18a, b, c, and d show typical results for aspect ratios of 1.0, 2.4, and 9.6.
- b. The effect of buoyancy (low F_0) is to increase the spreading angle, as is well known. This is illustrated in Fig. 19.
- c. Figure 19 also shows that the width of the free shear layer, as measured by δT values near the surface, is wider for the wider outlet channel. This is related to the dimensions of the horizontal eddies (vertical axis), which are apparently larger for the wider channel.

A series of graphs showing iso-temperature fluctuation lines is given in Appendix A. These graphs illustrate the effects of aspect ratio and Froude number in more detail; they identify areas of high fluctuation intensity. It can be seen, for example, that at a high degree of stability of stratification (low F_0 values), the measurements identify a surprisingly wide vertical area of high δT values. This is believed to be the result of internal waves forming near the point of discharge where the discharged warmer jet flow meets the colder ambient as observed in dye experiments. The existence of such waves (breaking or non-breaking) has previously been reported by Stefan, Hayakawa, and Schiebe³. Larger areas of high δT values are not necessarily associated with more entrainment of ambient colder water. They may merely reflect larger

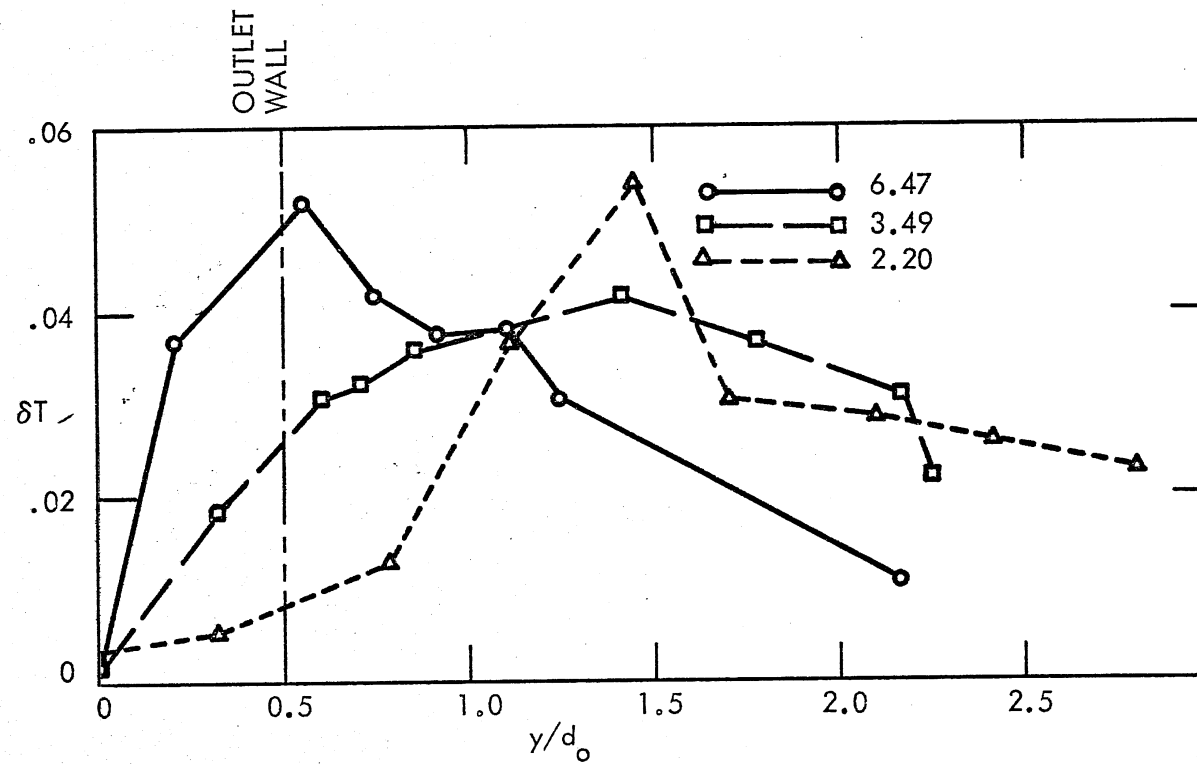


Fig. 18a - δT versus y/d_o perpendicular to jet axis at $A = 1.0$,
 $x/d_o = 1.7$, $R = 0$, and $F_o = 2.2, 3.5$, and 6.5

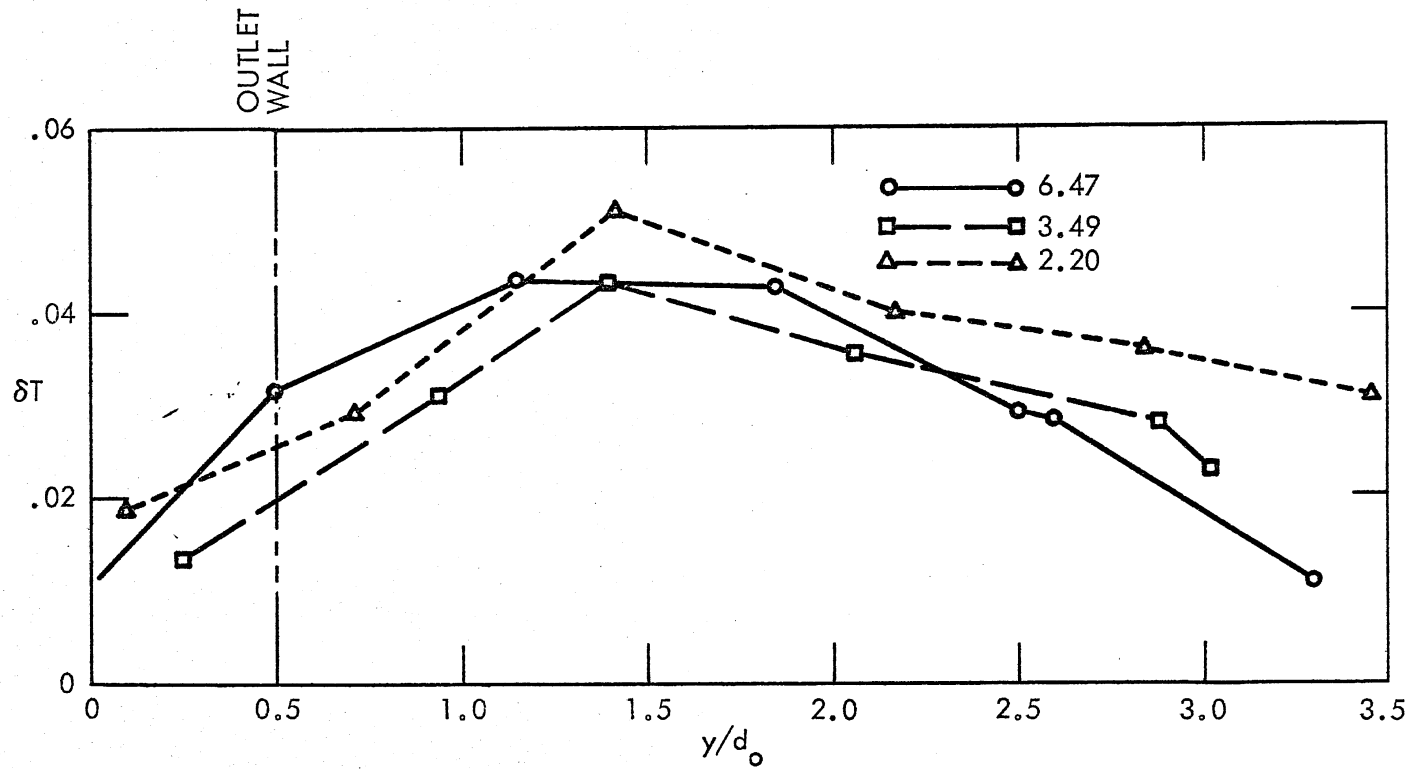


Fig. 18b - δT versus y/d_o perpendicular to jet axis at $A = 1.0$, $x/d_o = 3.5$, $R = 0$, and $F_o = 2.2, 3.5$, and 6.5

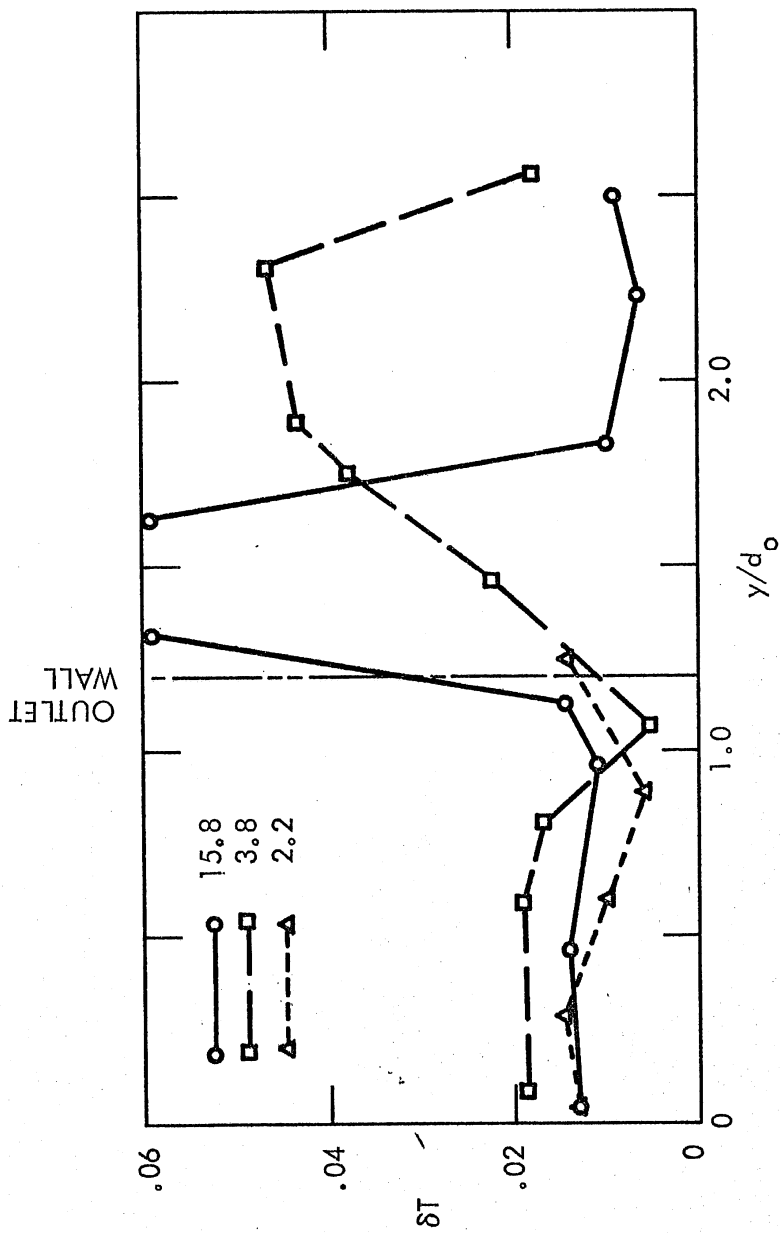


Fig. 18c - δT versus y/d_o perpendicular to jet axis at $A = 2.4$, $x/d_o = 2$, $R = 0$, and $F_o = 2.2, 3.8, \text{ and } 15.8$

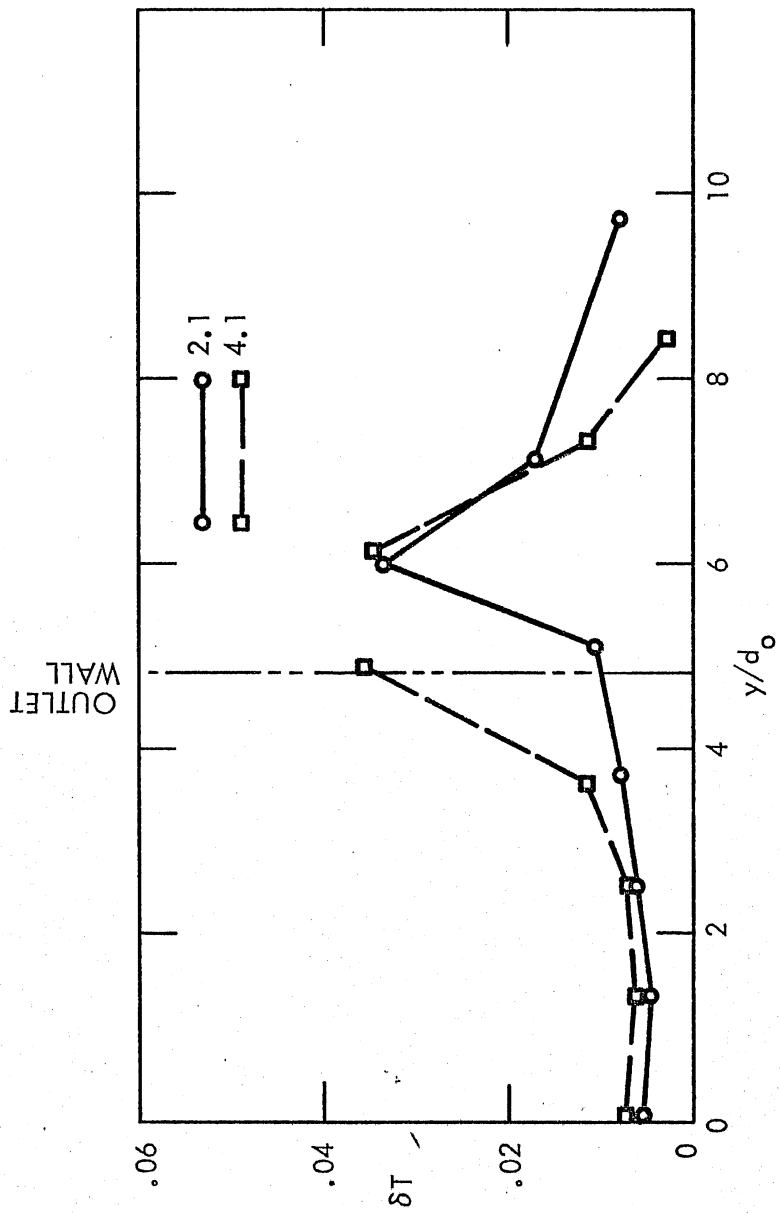


Fig. 18d - δT versus y/d_o perpendicular to jet axis at $A = 9.6$, $x/d_o = 2$, $R = 0$, and $F_o = 2.1$ and 4.1

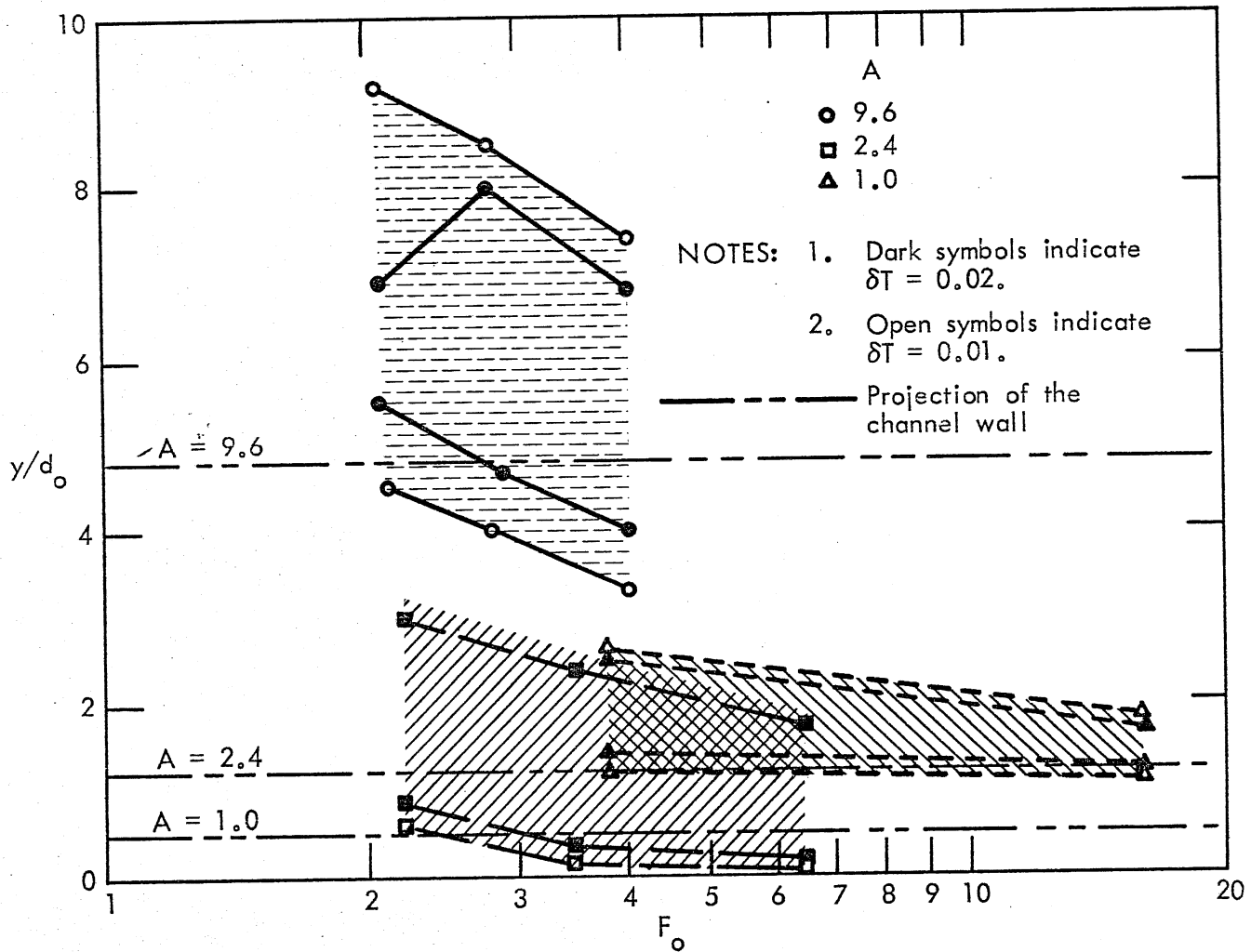


Fig. 19 - Spreading angle and width of free shear zone at $\delta T = 0.01$ and 0.02 for $A = 1.0, 2.4,$ and 9.6 ; $x/d_o = 2$ and $R = 0$

amplitudes of the vertical motions, and only if these waves are breaking waves or eddies will the entrainment be increased.

Upwelling of isotherms can be observed in Figs. A-7, A-8, and A-9 along the centerline of the jet. This is caused by an inward flow of cold water underneath the jet. As the flow converges toward the centerline of the jet, upwelling is caused through a stagnation effect. The phenomenon is much weaker for $A = 9.6$ than for $A = 2.4$.

In all longitudinal sections the iso-concentration lines of time-averaged water temperatures are quite similar in shape to the iso-fluctuation lines.

Velocity Data

Time-Averaged Velocities--Velocities were measured as local samples consisting of 50 instantaneous measurements spread over a one-minute period. Because of the size of the Delft current meter (diameter of the rotor = 15 mm), the measurement cannot be referred to as a point measurement; the results are nevertheless presented because they supplement the temperature data and are also used to calculate volumetric flow rates through integration of velocities in cross sections perpendicular to the jet axis.

Samples of instantaneous velocity measurements were used to compute time-averaged local velocities which were subsequently normalized using the centerline discharge velocity as a reference value. The resulting velocity concentrations, defined by Eq. (7), were first plotted versus distance along the axis of the jet, as were the excess temperatures in Fig. 13. Distances x_0/d_0 were read at the 0.98, 0.95, 0.90, and 0.80 levels and plotted versus Froude number F_0 for different aspect ratios. The results are shown in Figs. 20a, b, and c and 21.

The results derived from time-averaged temperatures in Figs. 14 and 15 can be compared with those obtained from time-averaged velocities in Figs. 20 and 21. It is apparent that increases in outlet channel aspect ratio result in longer ZFE lengths in terms of both temperature and velocity. The variations with Froude number are not consistent, however.

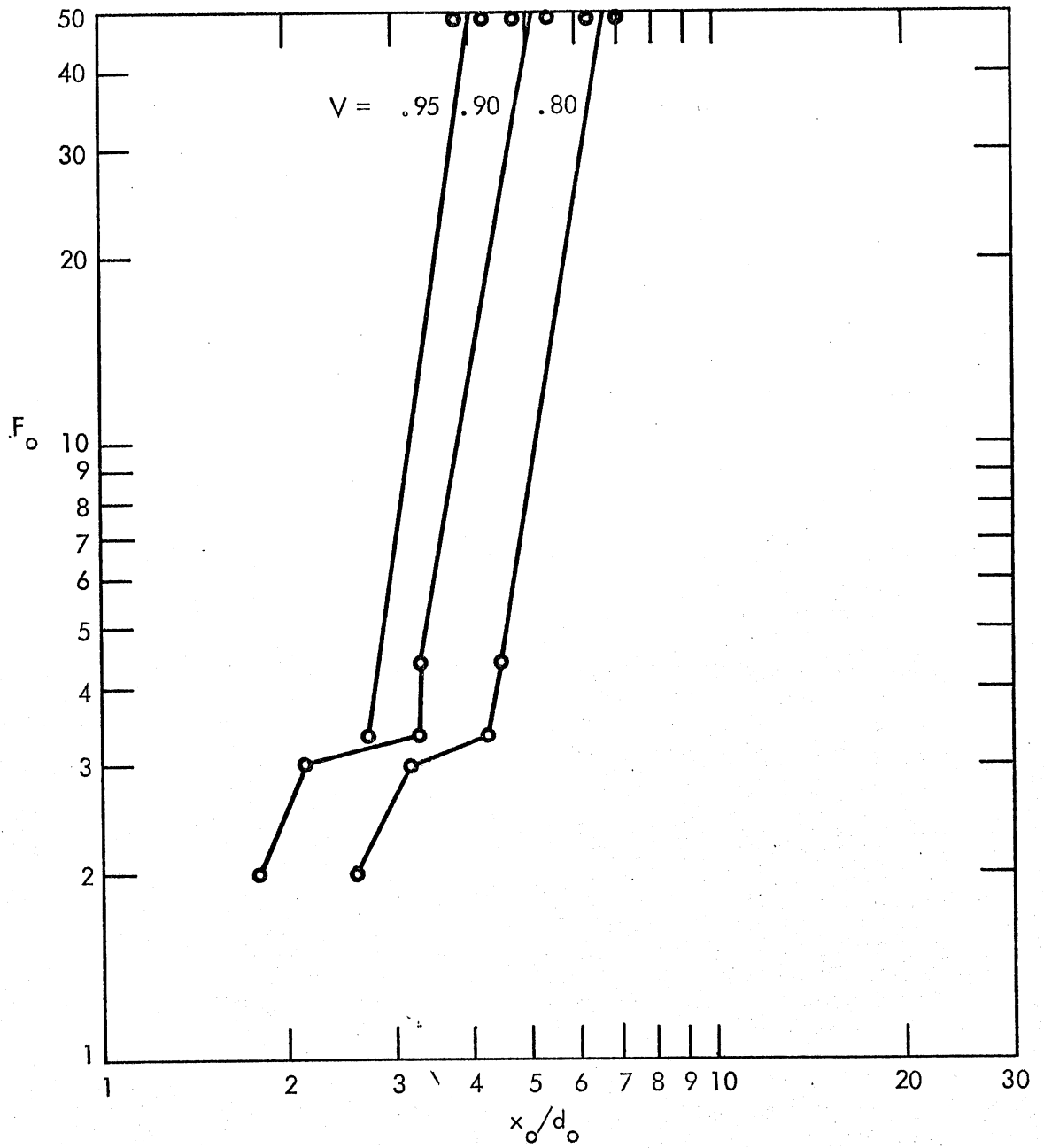


Fig. 20a - x_o/d_o versus F_o at $V = 0.95, 0.90,$ and 0.80 ; $A = 1.0$; and $R = 0$

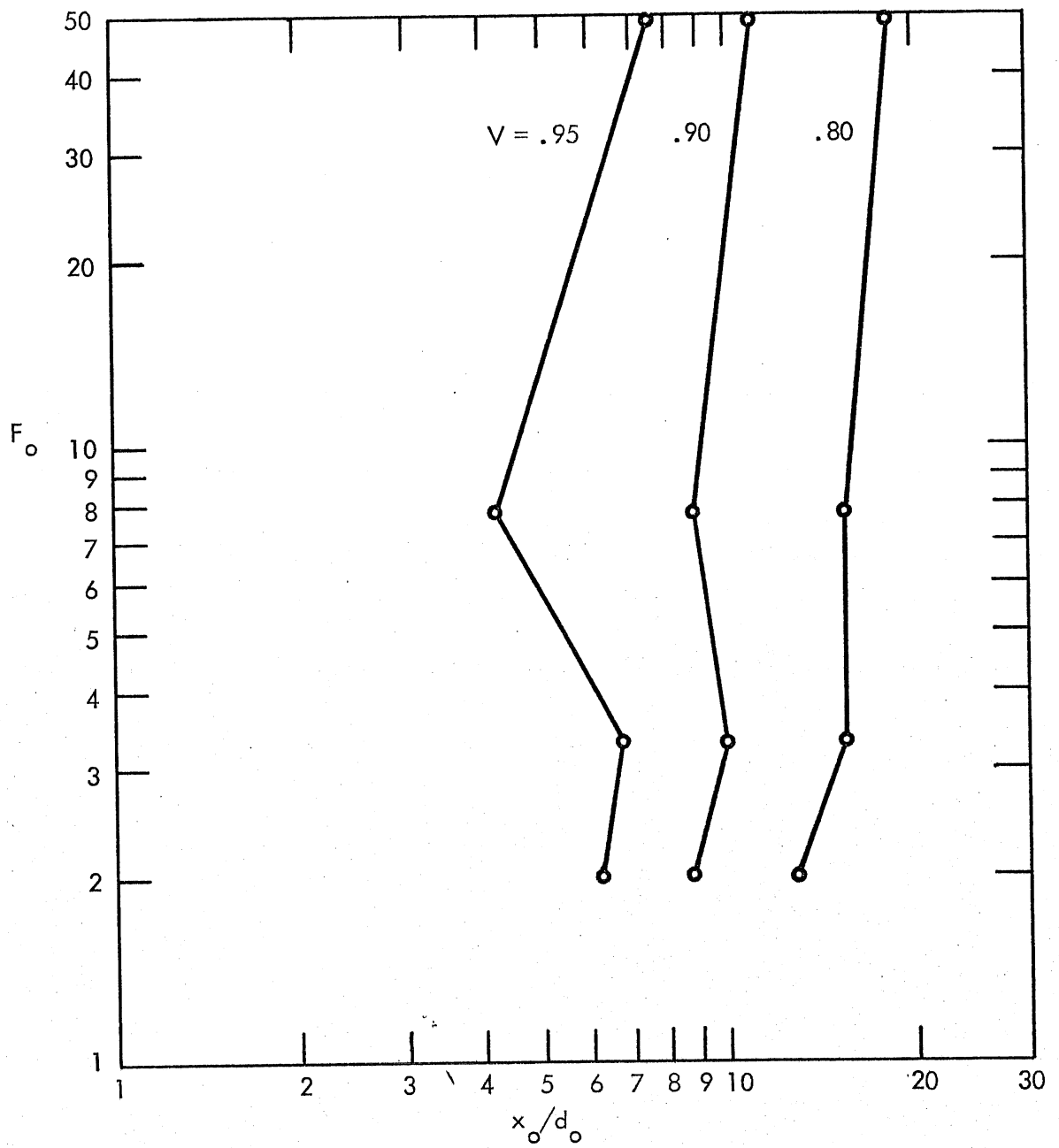


Fig. 20b - x_o/d_o versus F_o at $V = 0.95, 0.90,$ and 0.80 ; $A = 4.8$; and $R = 0$

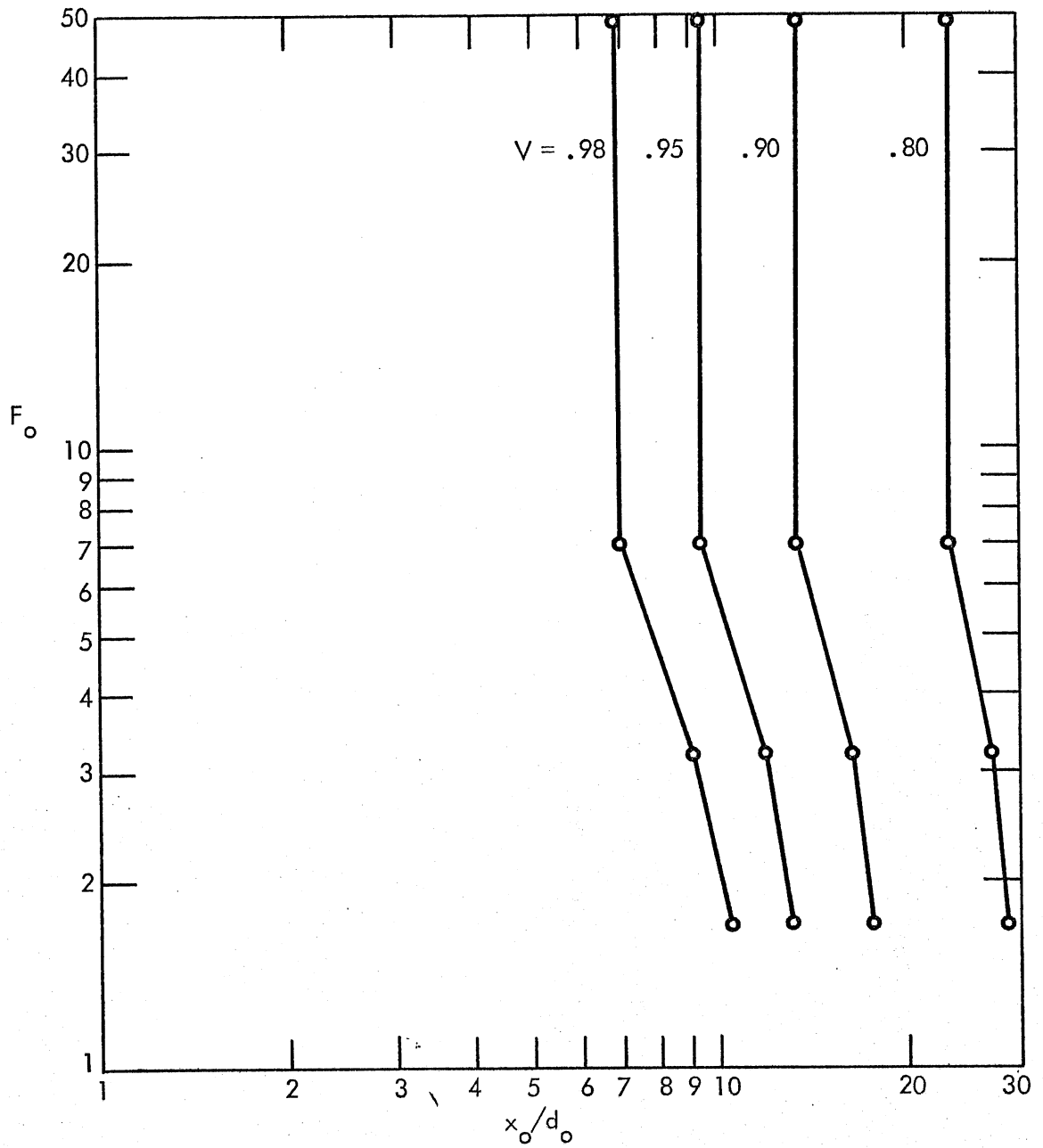


Fig. 20c - x_o/d_o versus F_o at $V = 0.98, 0.95, 0.90,$ and 0.80 ;
 $A = 9.6$; and $R = 0$

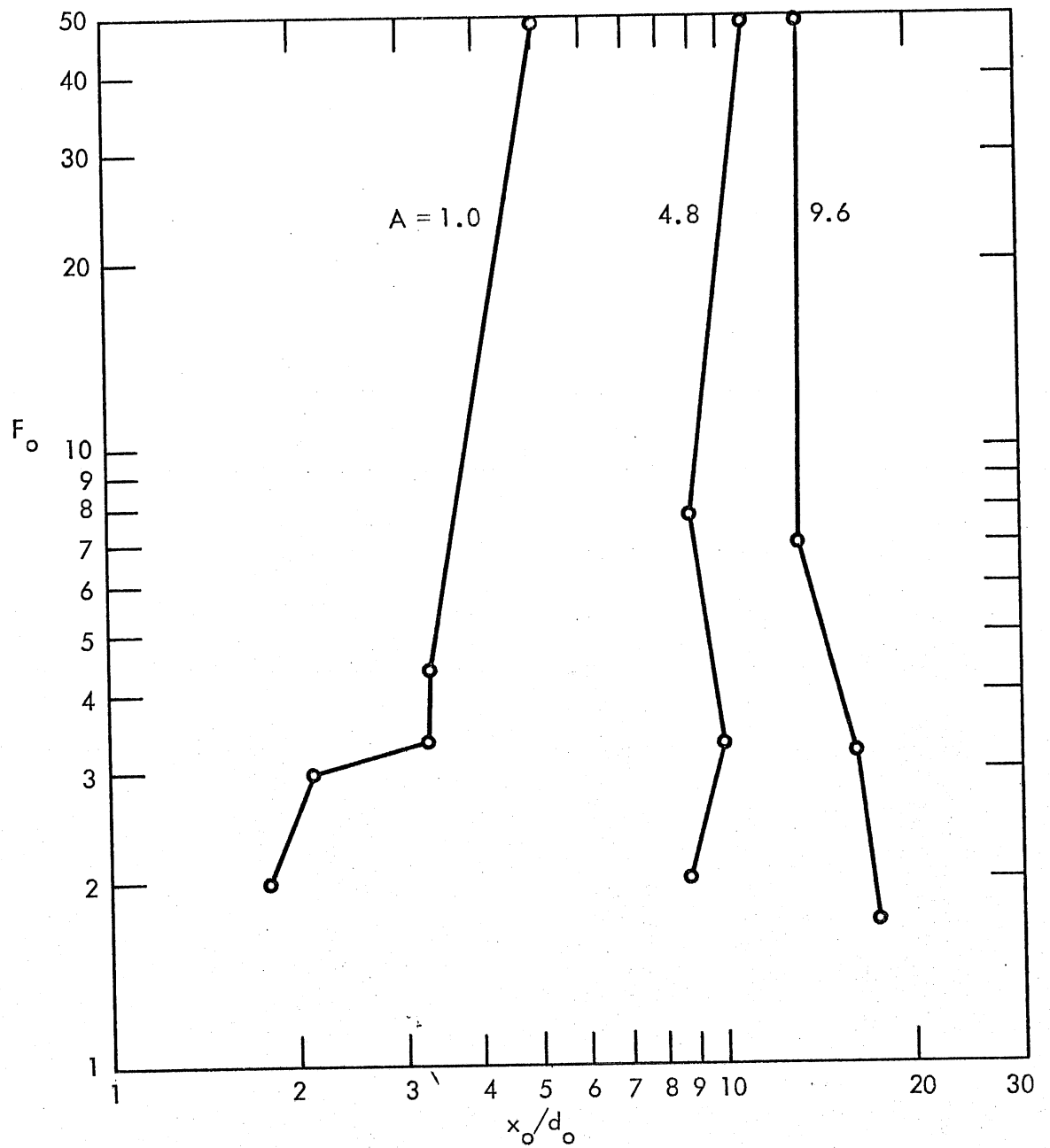


Fig. 21 - x_o/d_o versus F_o at $V = 0.9$; $A = 1.0, 4.8, \text{ and } 9.6$; and $R = 0$

The Froude number effect is more subtle than that of the aspect ratio; Froude number trends are similar for aspect ratios $A = 1.0$ and $A = 4.8$, but dissimilar for $A = 9.6$ below approximately $F_o = 3$. Absolute values of x_o/d_o at the 0.90 level or the 0.80 level do not match. Transfer of mass and transfer of momentum are somewhat different, but there are also differences in the spatial and temporal resolution of the temperature and velocity instrumentation, as was pointed out earlier; in addition, temperatures are initially uniform in the outlet channel, whereas velocities are not. (It should be remembered that the velocities have been normalized using the maximum velocity at the outlet.) Typical normalized average outlet velocities range from 1.156 at $A = 1.0$ to 1.093 at $A = 4.8$ and 1.04 at $A = 9.6$. Time-averaged percentage ratios of velocities should be increased by these factors before a comparison with time-averaged temperature data is made. But even then it will be difficult to interpret the results of such a comparison.

When the above procedure is applied, it is found that the lengths of the ZFE based on time-averaged velocities are still significantly shorter than those derived from time-averaged temperatures. Table 5 gives the ratios.

Table 5. RATIOS OF x_o VALUES, $\frac{(x_o)_{temp}}{(x_o)_{vel}}$, DERIVED FROM TEMPERATURE AND VELOCITY

<u>A = 1.0</u>			<u>A = 4.8</u>			<u>A = 9.6</u>		
<u>F_o</u>	<u>T = .90</u>	<u>T = .80</u>	<u>F_o</u>	<u>T = .90</u>	<u>T = .80</u>	<u>F_o</u>	<u>T = .90</u>	<u>T = .80</u>
2.0	2.7	2.2	2.0	1.6	1.5	1.7	0.93	0.9
3.0	2.7	2.4	-	-	-	-	-	-
3.4	1.9	1.7	3.3	1.4	1.3	3.2	1.2	1.0
4.4	2.0	1.8	7.8	1.4	1.1	7.0	1.3	1.3
11.6	1.5	1.5	10.5	1.1	1.0	10.0	1.1	1.2

Fluctuating Velocity Components--Interpreting the turbulent velocity data is even more difficult than interpreting the time-averaged values, because the exact response characteristics of the Delft current meter are not known. Sample results are presented in Figs. 22a and 22b.

Volumetric Flow Rates and Entrainment

Integration of velocity profiles in cross sections perpendicular to the jet axis provided information on the volumetric flow rates, specifically on their variation with distance from the outlet. This information gives both insight into the entrainment mechanism and data which can be compared directly with those obtained using mathematical models. This information is contained in Figs. 23a, b, and c. The effects of the aspect ratio as well as those of the Froude number are clear. For further comparison, Fig. 24 shows the computed flow ratio for non-buoyant, fully submerged jets after Albertson, et al.⁶. The results have been obtained by applying the three-dimensional theory to outlets of small aspect ratio, $A = 1$ and $A = 2.4$ (a hydraulic diameter was used instead of a real diameter), and the two-dimensional theory to $A \rightarrow \infty$. The results of Fig. 24 match those of Fig. 23 qualitatively. To make the effects of A and F_o even clearer, Fig. 25 was prepared. It is noteworthy that at the larger aspect ratios, changes in the Froude number reduce the flow ratio by no more than 20 per cent below that for isothermal ($F_o \rightarrow \infty$) conditions. This means that an increase in stability due to density stratification does not reduce the initial entrainment excessively. It might be argued that buoyancy increases the contact area between warm and cold water through lateral spreading and thereby counteracts the stability effects to some degree. But the main reason for the relatively high degree of entrainment in the presence of buoyancy seems to be the vortex and internal wave formation near the outlet due to viscous shear regardless of Froude number. Figure 26 illustrates this vortex formation. The photograph was obtained by injecting blue dye at the wall of the outlet channel near the water surface and red dye at the bottom of the outlet channel. Even in the black-and-white reproduction, the vortex (and internal wave) shedding shows up very clearly.

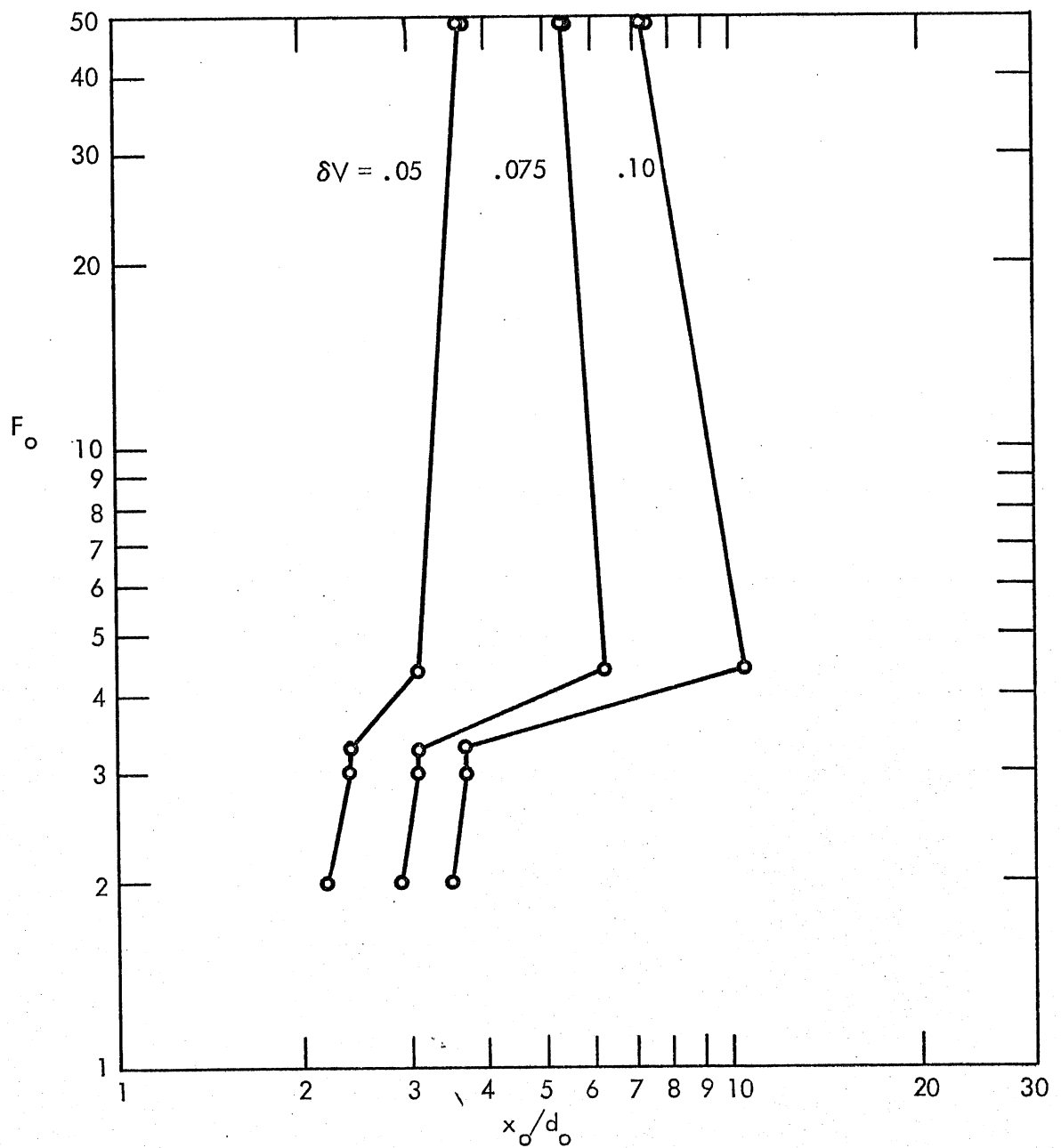


Fig. 22a - x_o/d_o versus F_o at $\delta V = 0.05, 0.075, \text{ and } 0.10$;
 $A = 1.0$; and $R = 0$

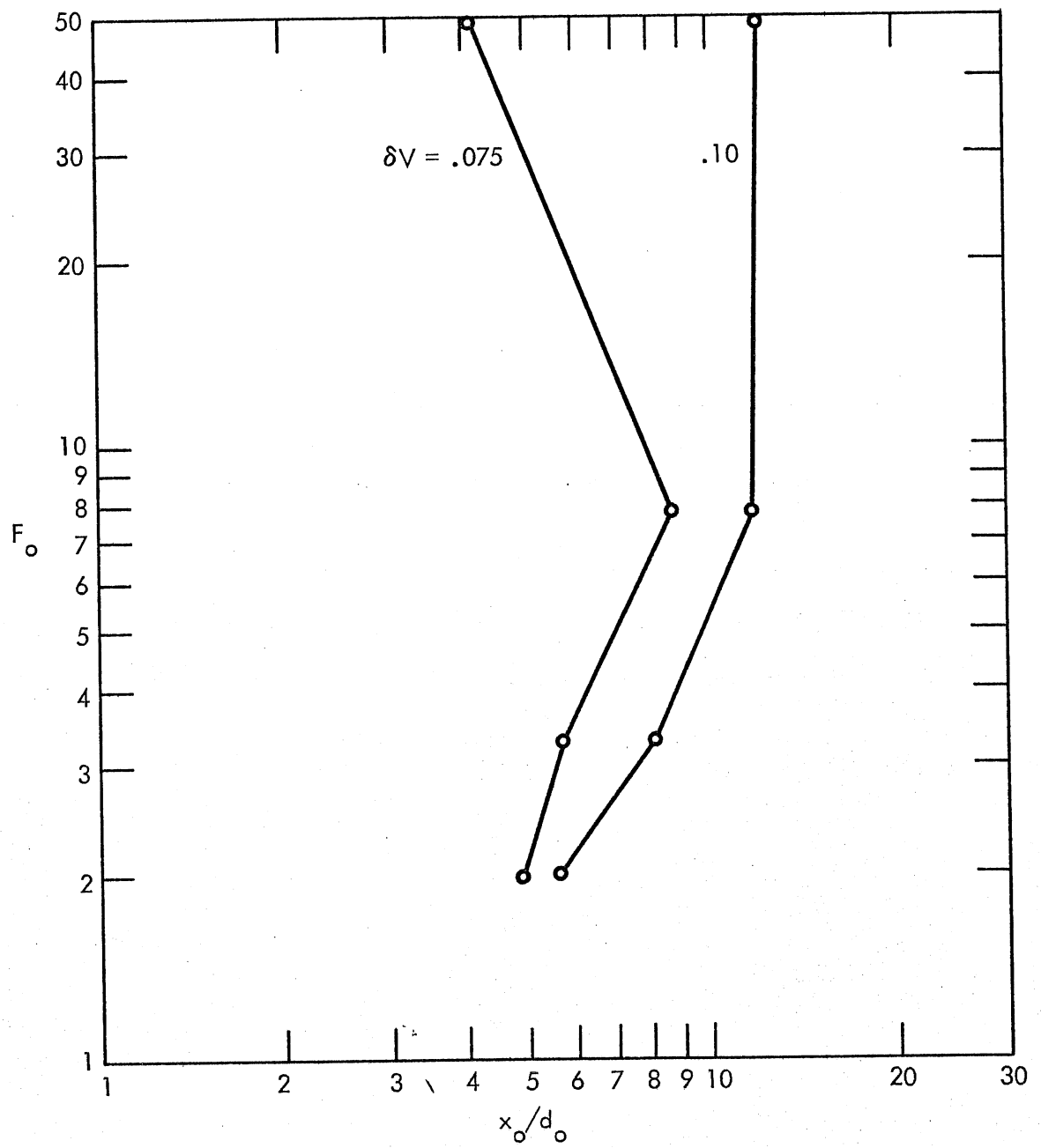


Fig. 22b - x_0/d_0 versus F_0 at $\delta V = 0.075$ and 0.10 , $A = 4.8$,
and $R = 0$

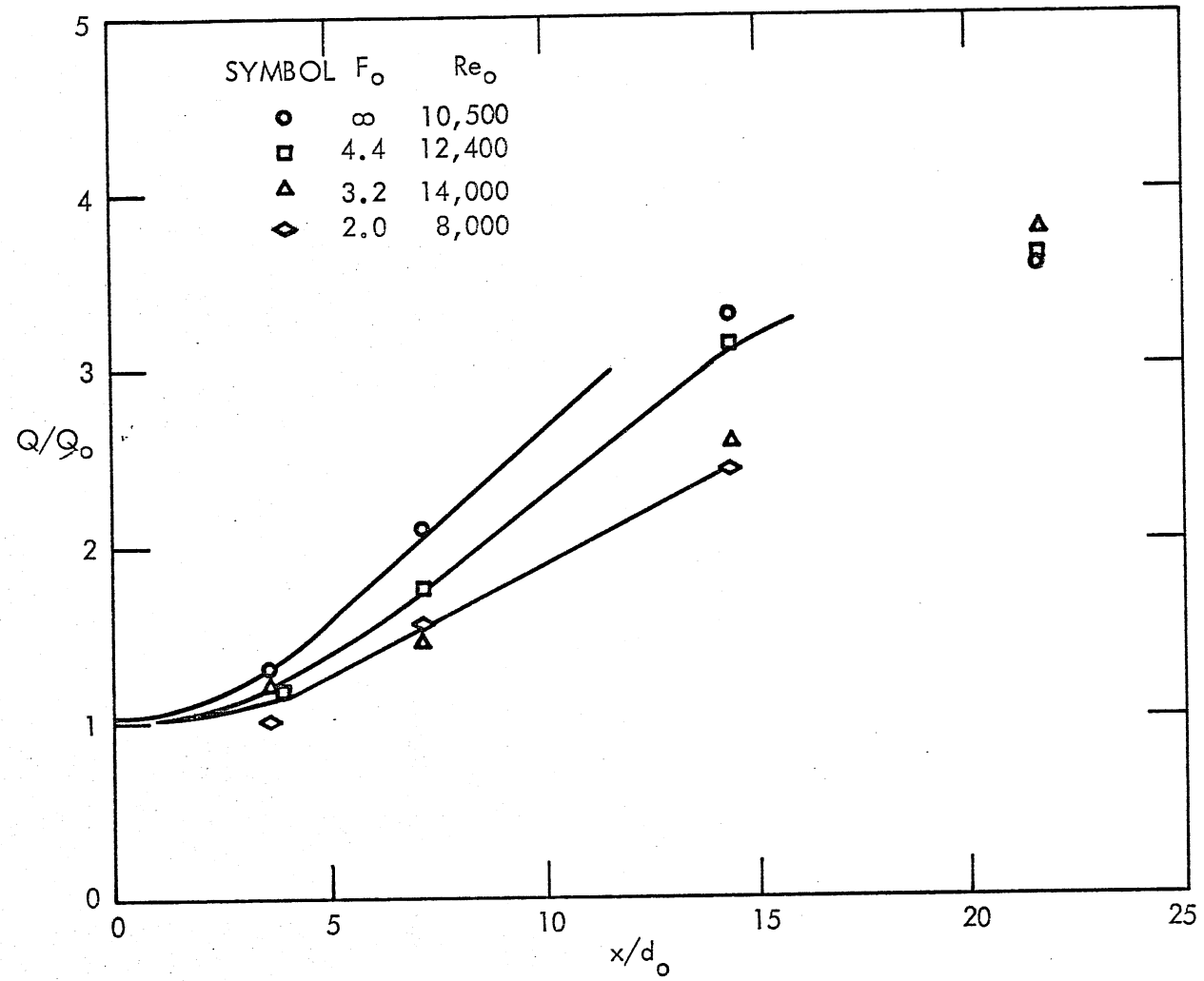


Fig. 23a - Q/Q_0 versus x/d_0 at $A = 1.0$ and $R = 0$

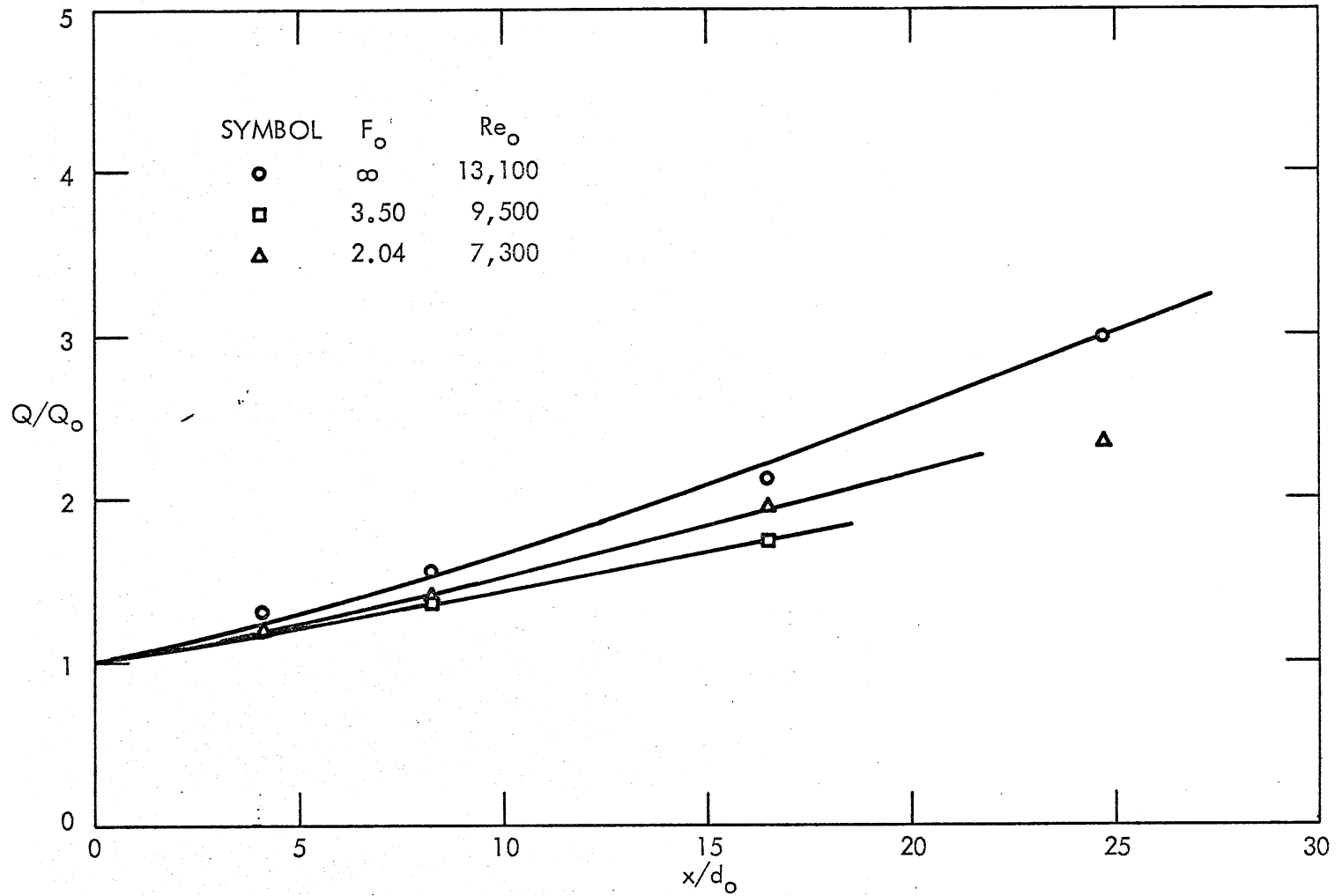


Fig. 23b - Q/Q_0 versus x/d_0 at $A = 4.8$ and $R = 0$

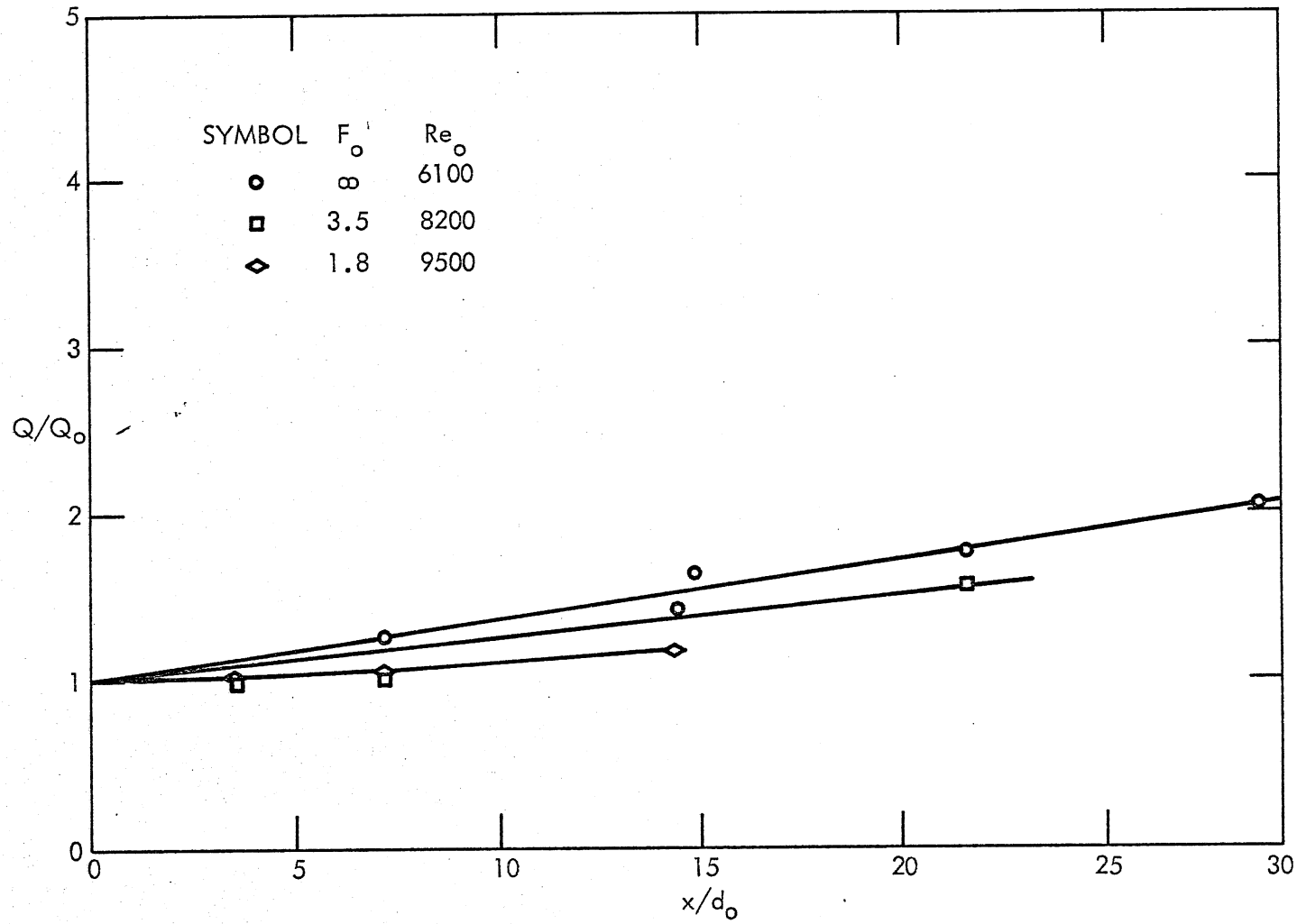


Fig. 23c - Q/Q_0 versus x/d_0 at $A = 9.6$ and $R = 0$

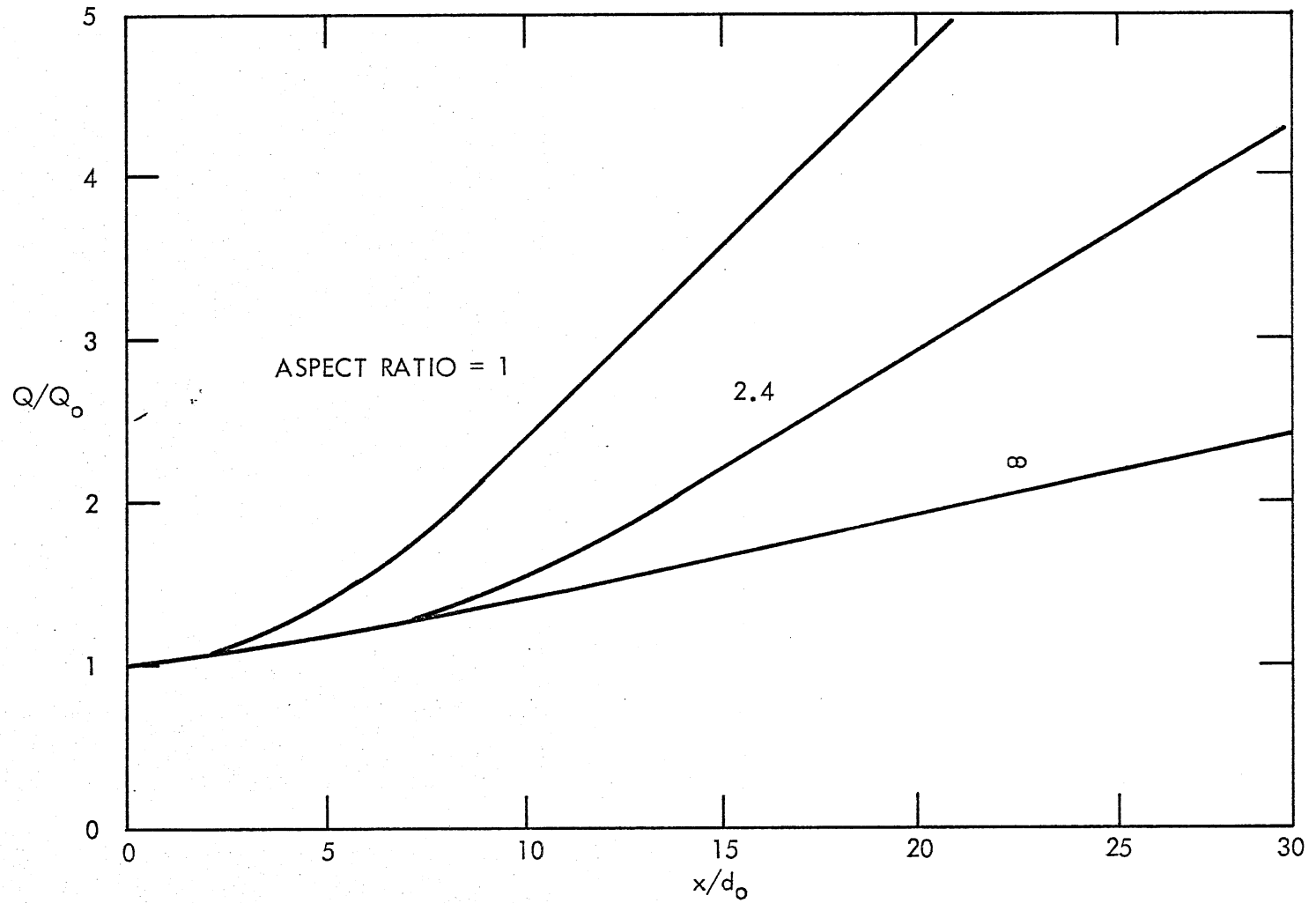


Fig. 24 - Q/Q_0 versus x/d_0 for fully submerged, non-buoyant two- and three-dimensional jets (computed after Albertson, et al.⁶ to illustrate effect of aspect ratio)

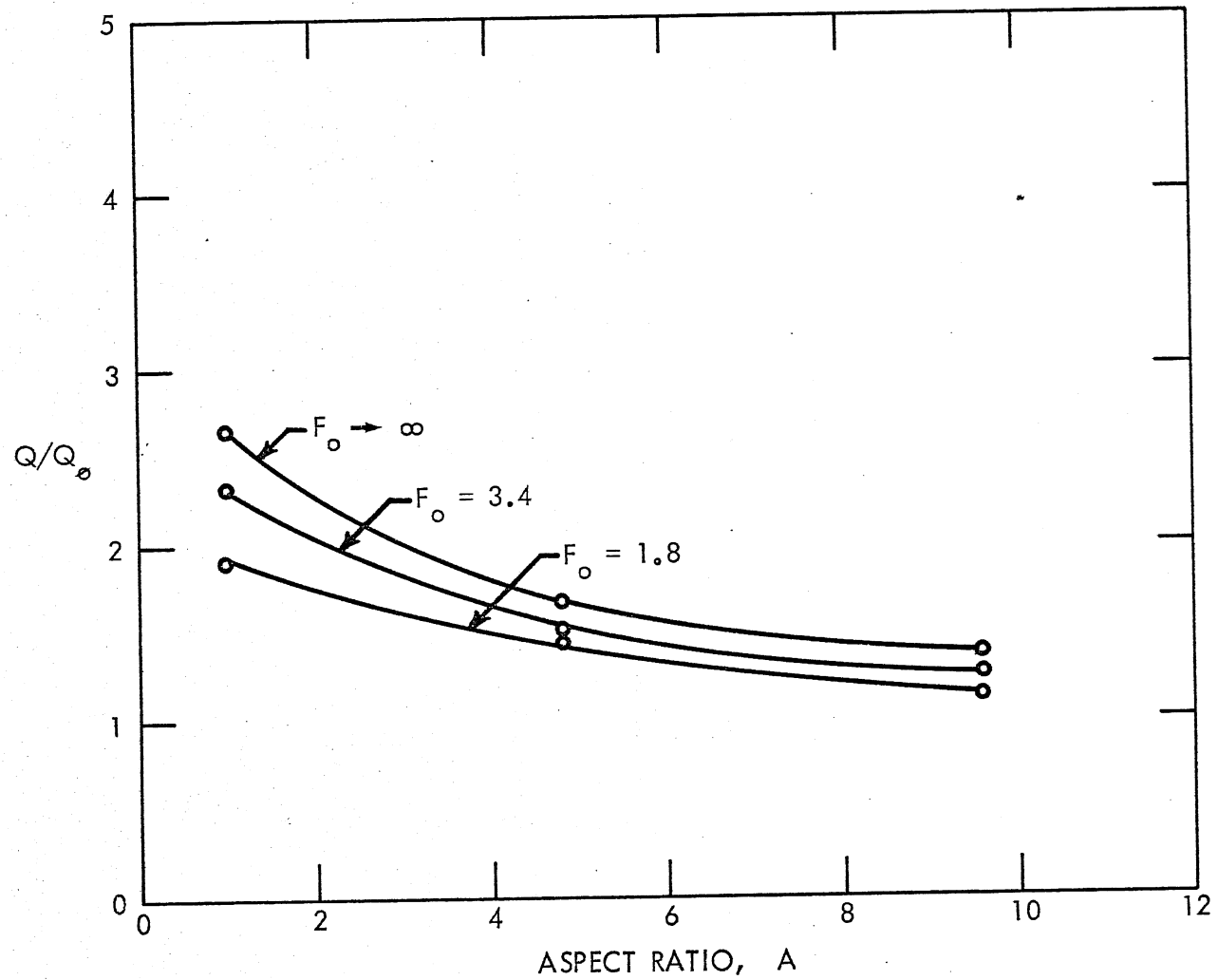


Fig. 25 - Q/Q_0 versus A at $F_0 = 1.8$, $F_0 = 3.4$, and $F_0 \rightarrow \infty$;
 $x/d_0 = 10$; and $R = 0$

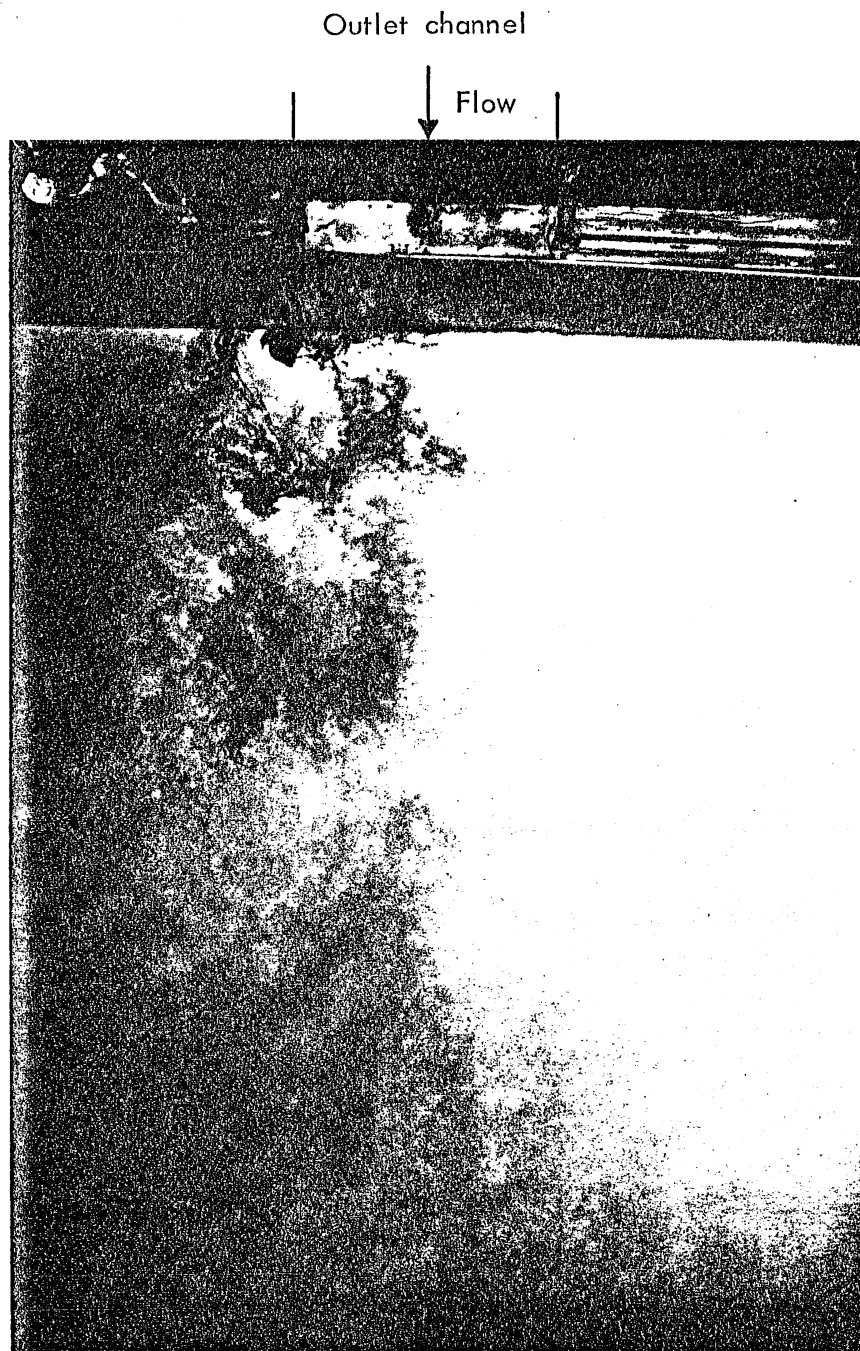


Fig. 26 - Photograph of vortex formation near the outlet at $A = 2.4$, $F_o = 3.46$, and $R = 0$

MAIN EXPERIMENTS: CURVILINEAR JETS

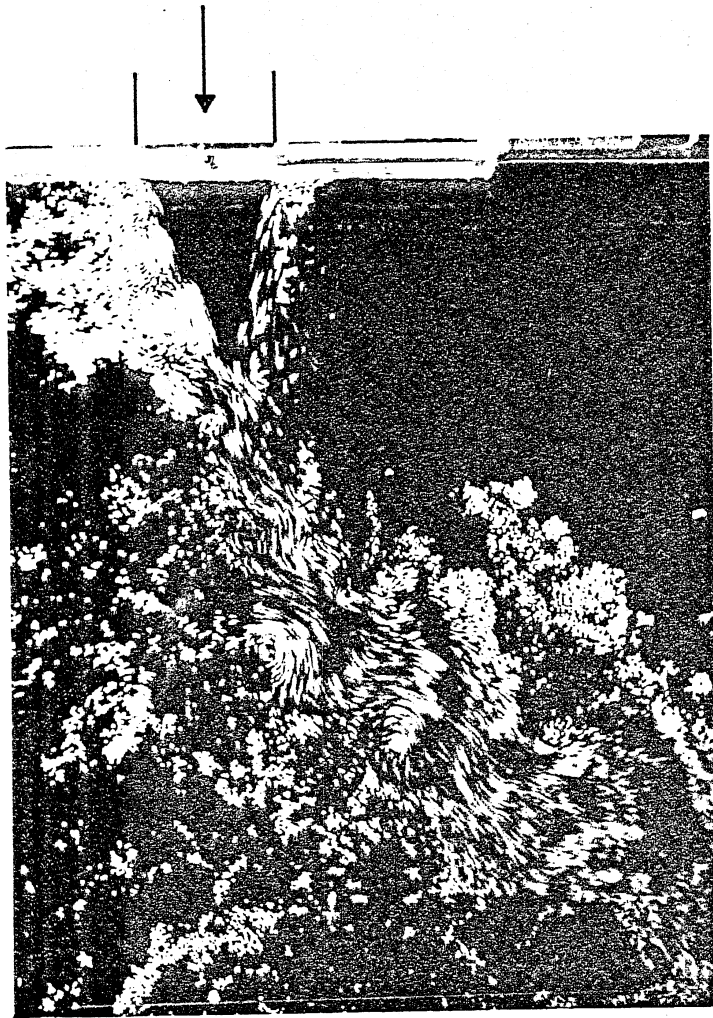
Photographs of Flow Features

Photographic data on surface flow patterns were not acquired in a systematic manner because they are of questionable value with regard to determining the length and trajectory of the zone of re-establishment. However, they do provide useful illustrations of some characteristic flow features. Figure 27, for example, shows the discharge from a channel with $A = 2.4$ at $F_o = 25.8$ and $F_o = 2.8$. Significant features are

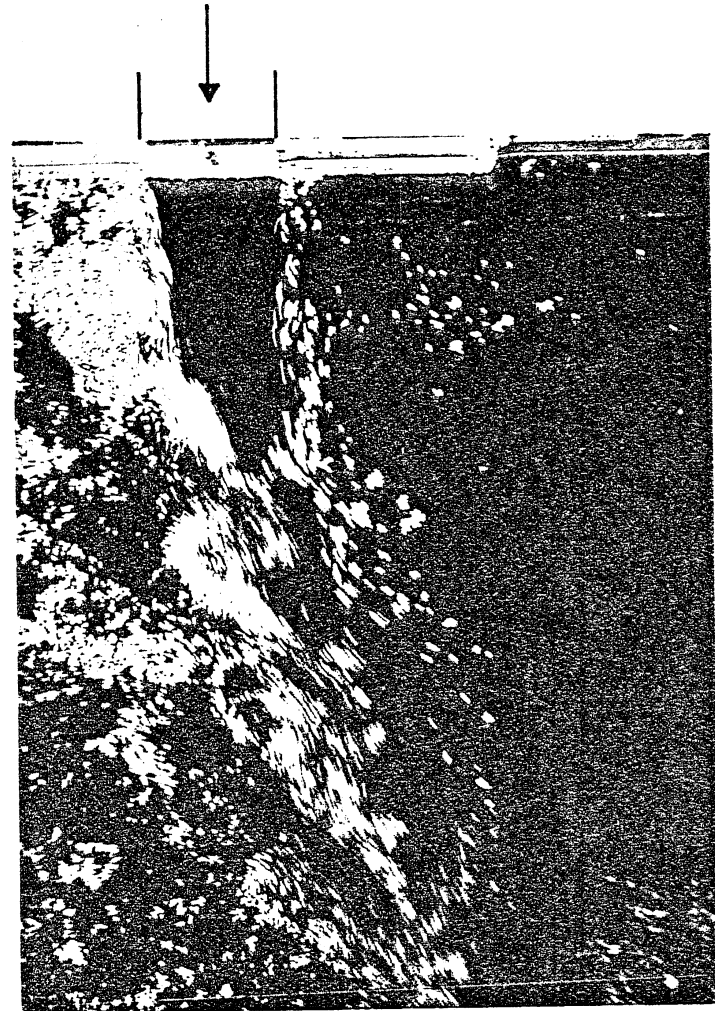
- a. the approximate surface extent of the plume as shown by the streaks of floating particles;
- b. the deflection of the jet by the cross-flow;
- c. the vortex shedding and undulation of the jet trajectory at the higher F_o value;
- d. the area of upwelling of the cross-flow marked by the absence of particles on the downstream side of the plume;
- e. the core region, a triangular region without particles in front of the outlet.

Trajectories

The plume trajectory was determined by several different methods at each aspect ratio. The plume axis location was first estimated by injecting dye into the outlet channel and observing the path of the most rapidly moving dye. The flow direction was then measured with a vane suspended by a taut monofilament thread. A $1/4$ -in.-thick brass disk was also attached to the vane shaft to provide inertia to dampen the high-frequency oscillations. These data were then used to supplement the dye measurements to determine the plume trajectory to be used as a baseline for the lateral velocity and temperature profiles. The velocity and temperature measurements were taken in planes perpendicular to the baseline plume trajectory. The same procedure was followed at each aspect ratio for the isothermal case and with a Froude number of approximately 3.25.



$F_o = 25.8$



$F_o = 2.8$

Fig. 27 - Photographs of discharge into a crossflow at $A = 2.4$, $R = 0.41$, and $F_o = 25.4$ and 2.8

A typical plot of the baseline trajectory for an aspect ratio of 4.8 at a Froude number of 3.25 is shown in Fig. 28. The dashed lines show the location of the lateral profiles. Note also in Fig. 28 that the plume centerline lies very near the shear zone between the outlet flow and the cross-flow. The plume seems to decay mostly from the upstream side, where the warm water is swept down and under the plume and then downstream by the cross-flow.

The plume trajectory can also be determined from the maximum velocities and temperatures measured in the lateral surveys. These are shown for aspect ratios of 1.0, 2.4, and 4.8 in Figs. 29a, b, and c respectively. Note that the effect of buoyancy is to straighten out the trajectory. The observed centerline coincides quite well with that determined from the maximum velocities for both the buoyant and non-buoyant cases. The line of maximum temperature lies downstream of the maximum velocity for both of the narrower channels ($A = 1.0$ and 2.4) and coincides with the maximum velocity for the wide channel ($A = 4.8$).

Figure 30a shows a summary plot of the observed plume centerlines for all three channels for both the buoyant and non-buoyant cases. A summary plot giving our best estimate of plume trajectory based on maximum velocities from the lateral surveys is given in Fig. 30b. The effect of both aspect ratio and Froude number can be seen clearly. As the channel width increases, the plume trajectory tends to flatten out. The effect of changing the Froude number from non-buoyant to $F_o = 3.25$ is much larger than the effect of the aspect ratio. The Froude number was varied by changing only the outlet temperature. The outlet velocity was held constant for all the crossflow experiments. The average outlet velocity was 0.53 fps (0.162 m/sec) and the crossflow velocity ratio, R , was 0.415. The outlet Reynolds number, Re_o , varied from about 11,000 to 15,000 depending on the outlet water temperature.

Length of Zone of Flow Establishment (ZFE)

The development length s_o/d_o has been measured using three different techniques: (1) outflow velocity decay, (2) temperature concentration, and (3) temperature fluctuation. The velocity fluctuations were

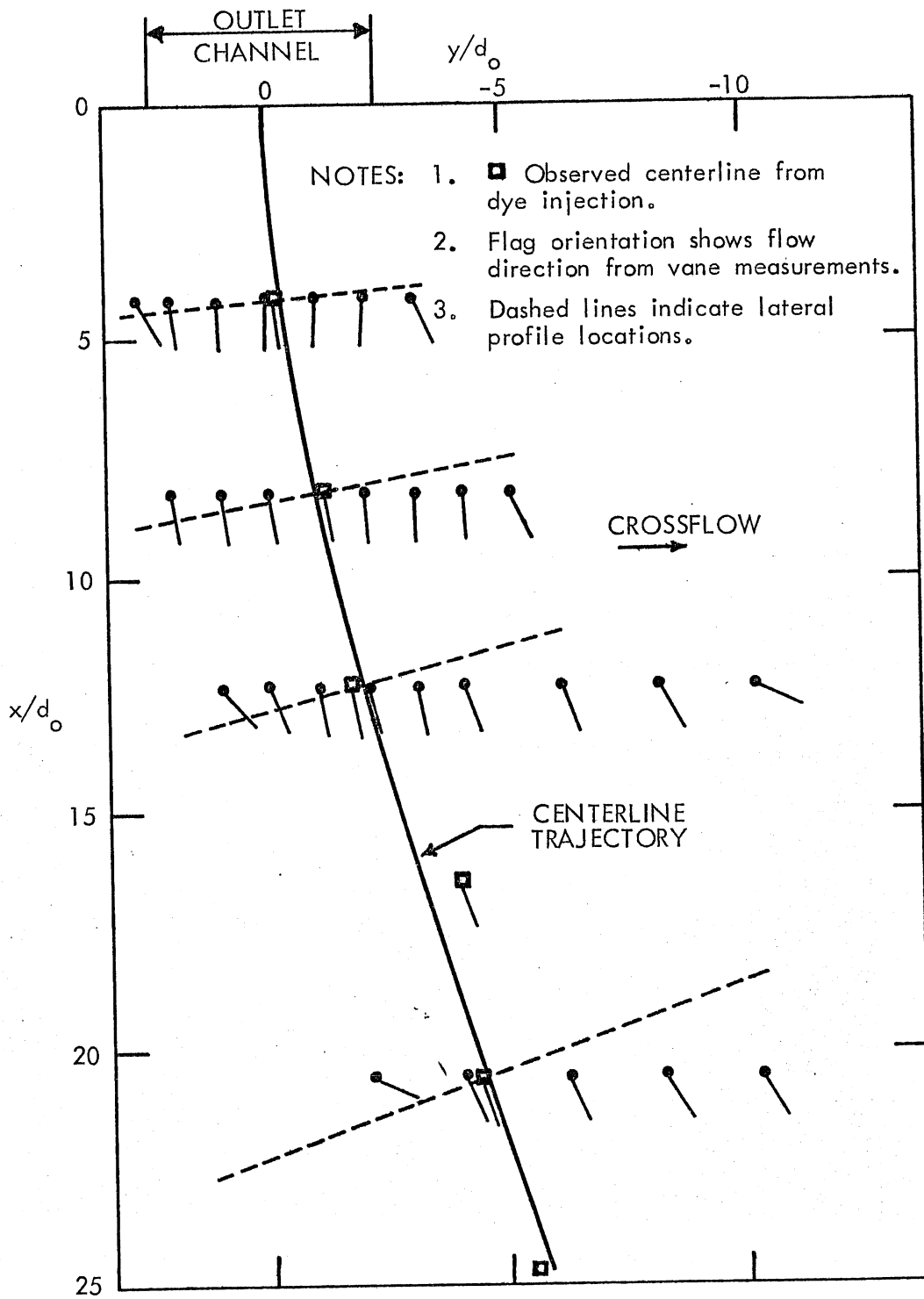


Fig. 28 - Typical centerline plume trajectory at $A = 4.8$, $R = 0.41$, and $F_o = 3.25$

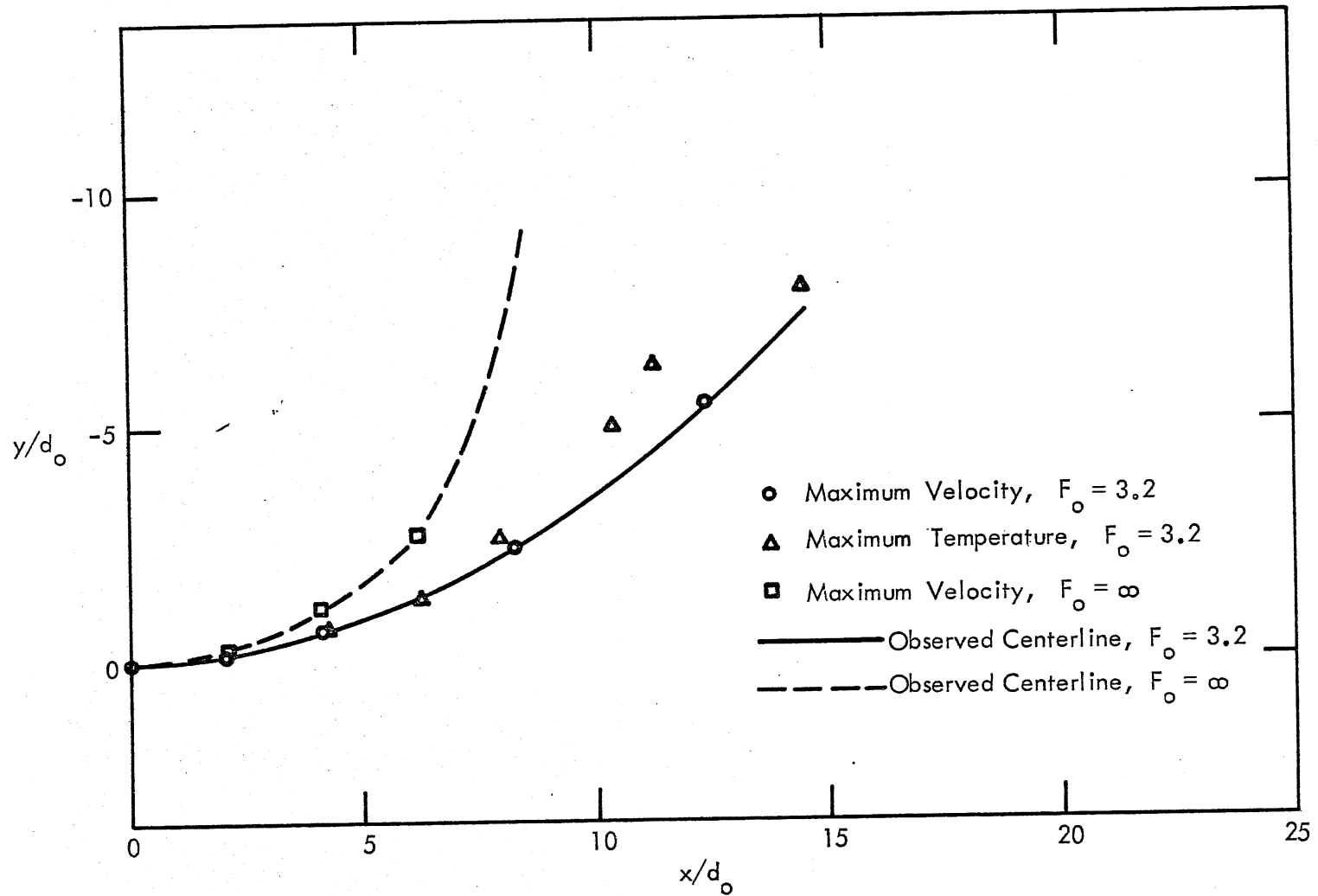


Fig. 29a - Plume trajectory at $A = 1.0$, $R = 0.41$, and $F_o = 3.2$ and ∞

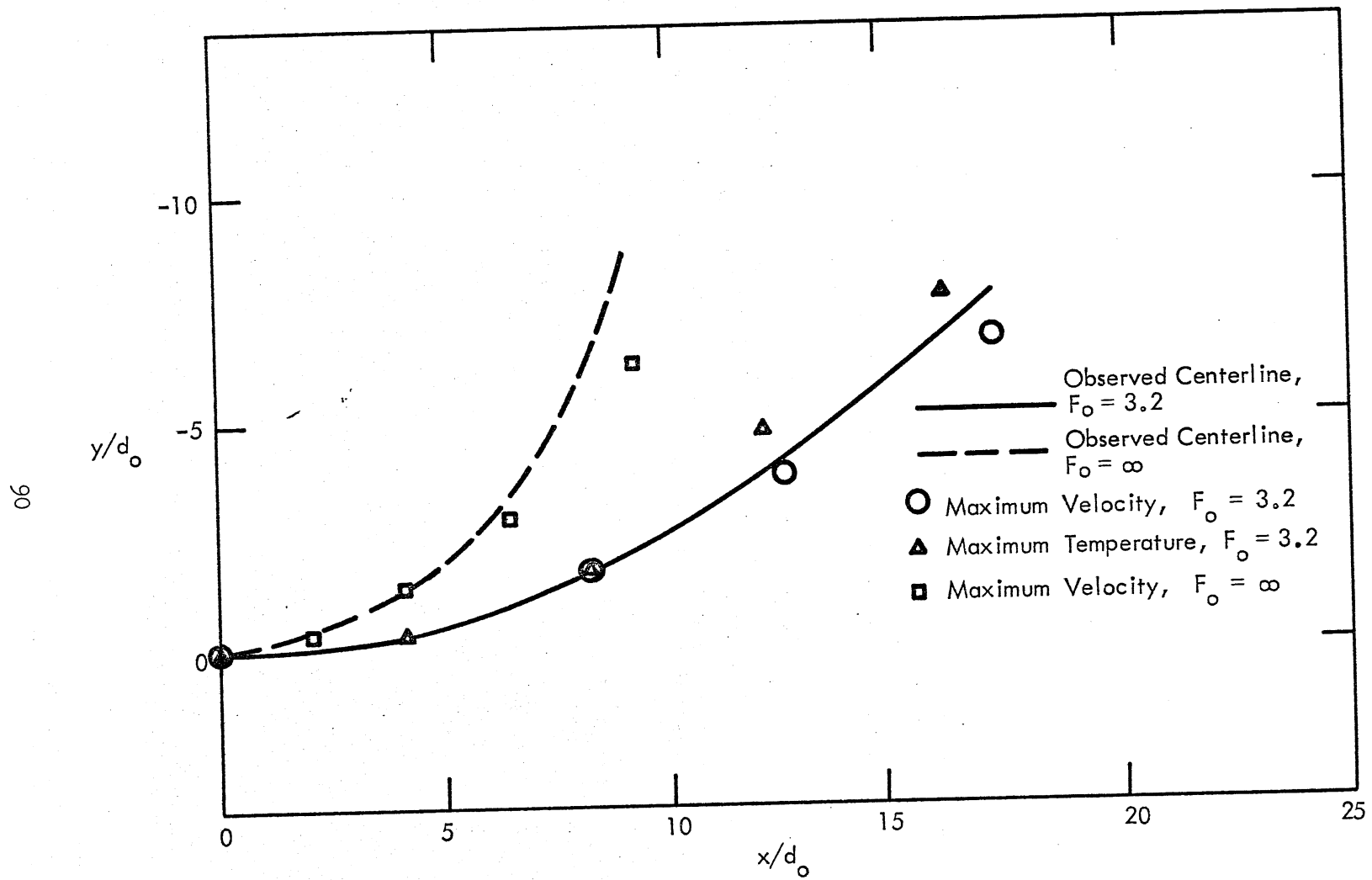


Fig. 29b - Plume trajectory at $A = 2.4$, $R = 0.41$, and $F_o = 3.2$ and ∞

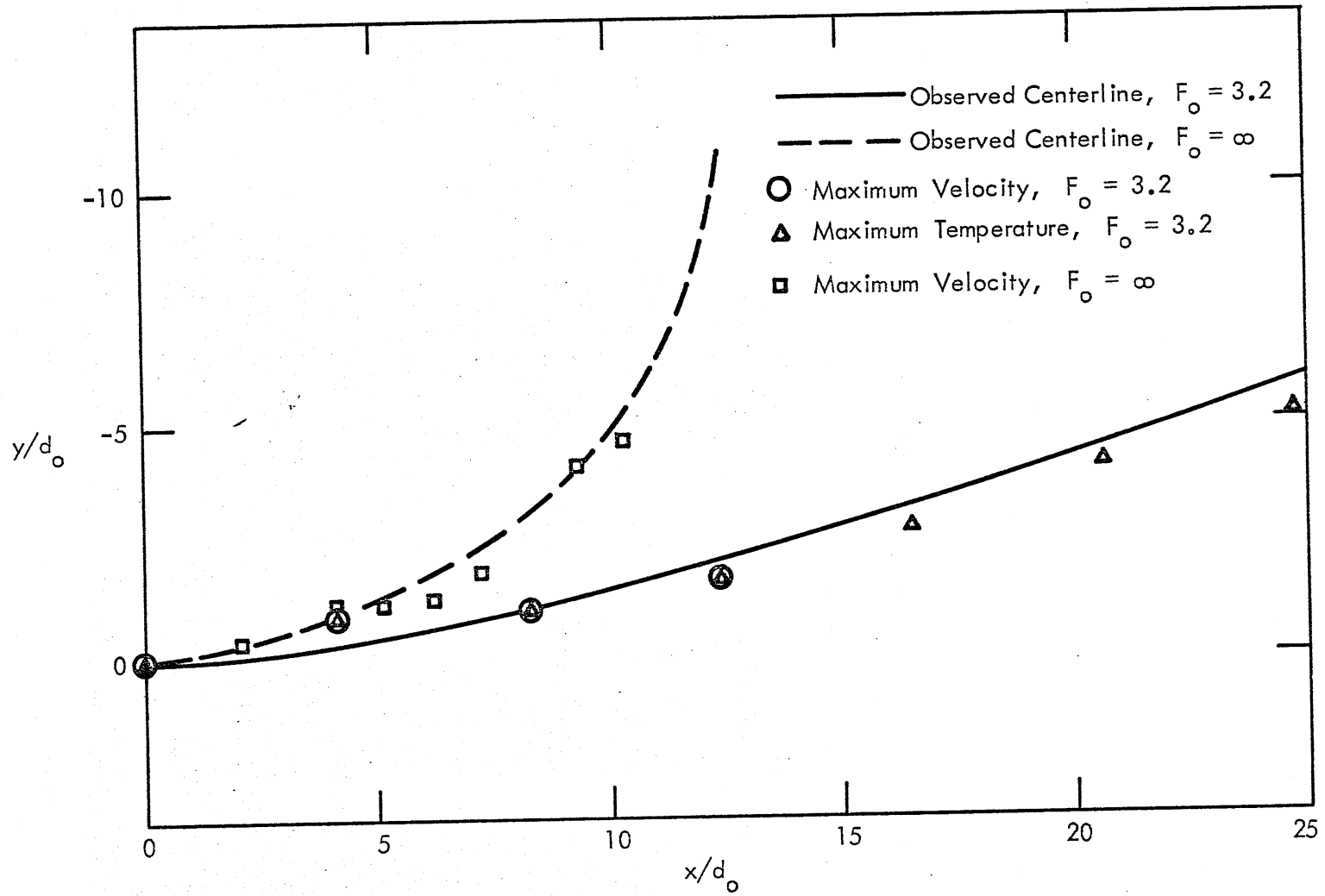


Fig. 29c - Plume trajectory at $A = 4.8$, $R = 0.41$, and $F_o = 3.2$ and ∞

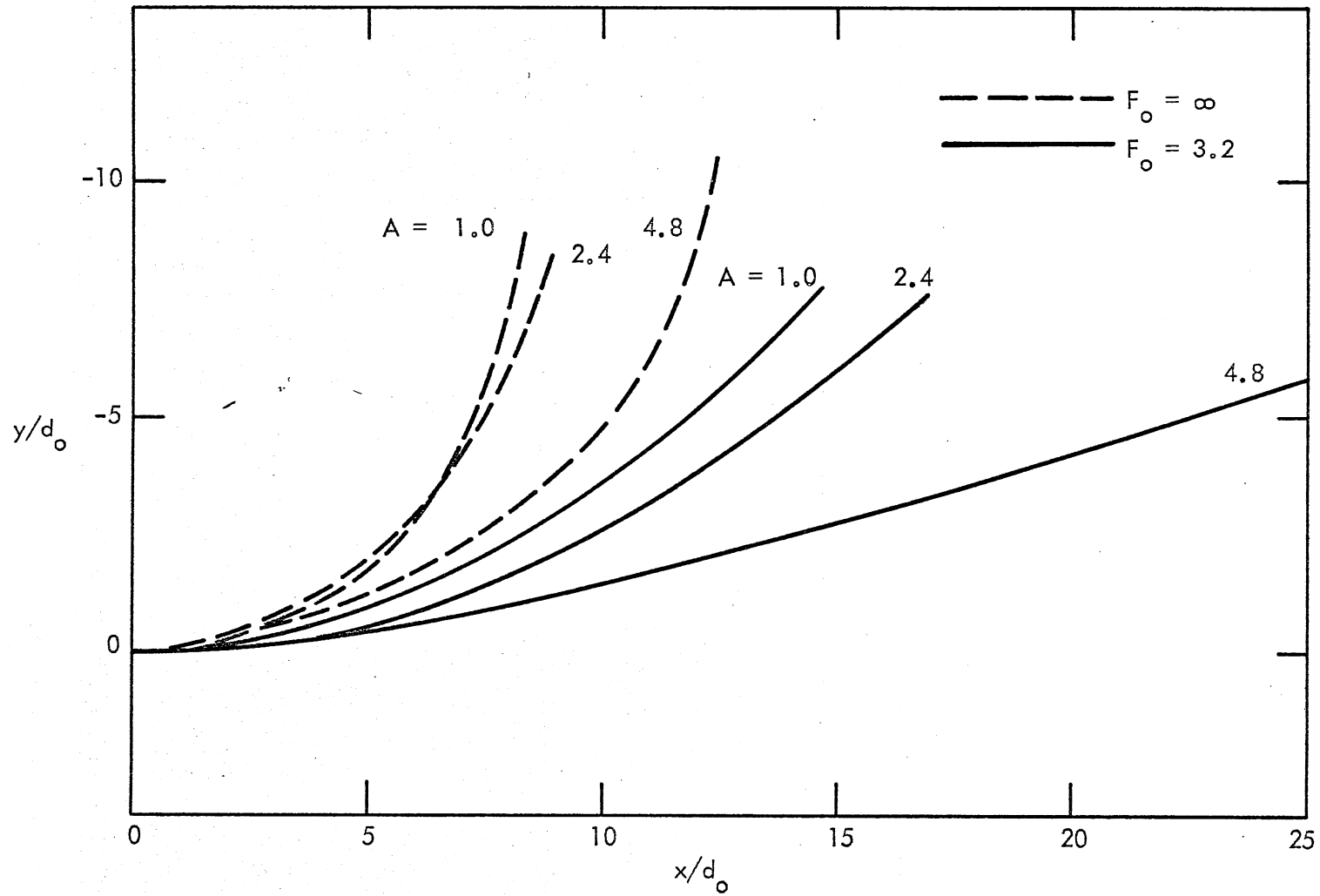


Fig. 30a - Observed trajectories, $A = 1.0, 2.4, \text{ and } 4.8$; $F_o = 3.3 \text{ and } \infty$; and $R = 0.41$

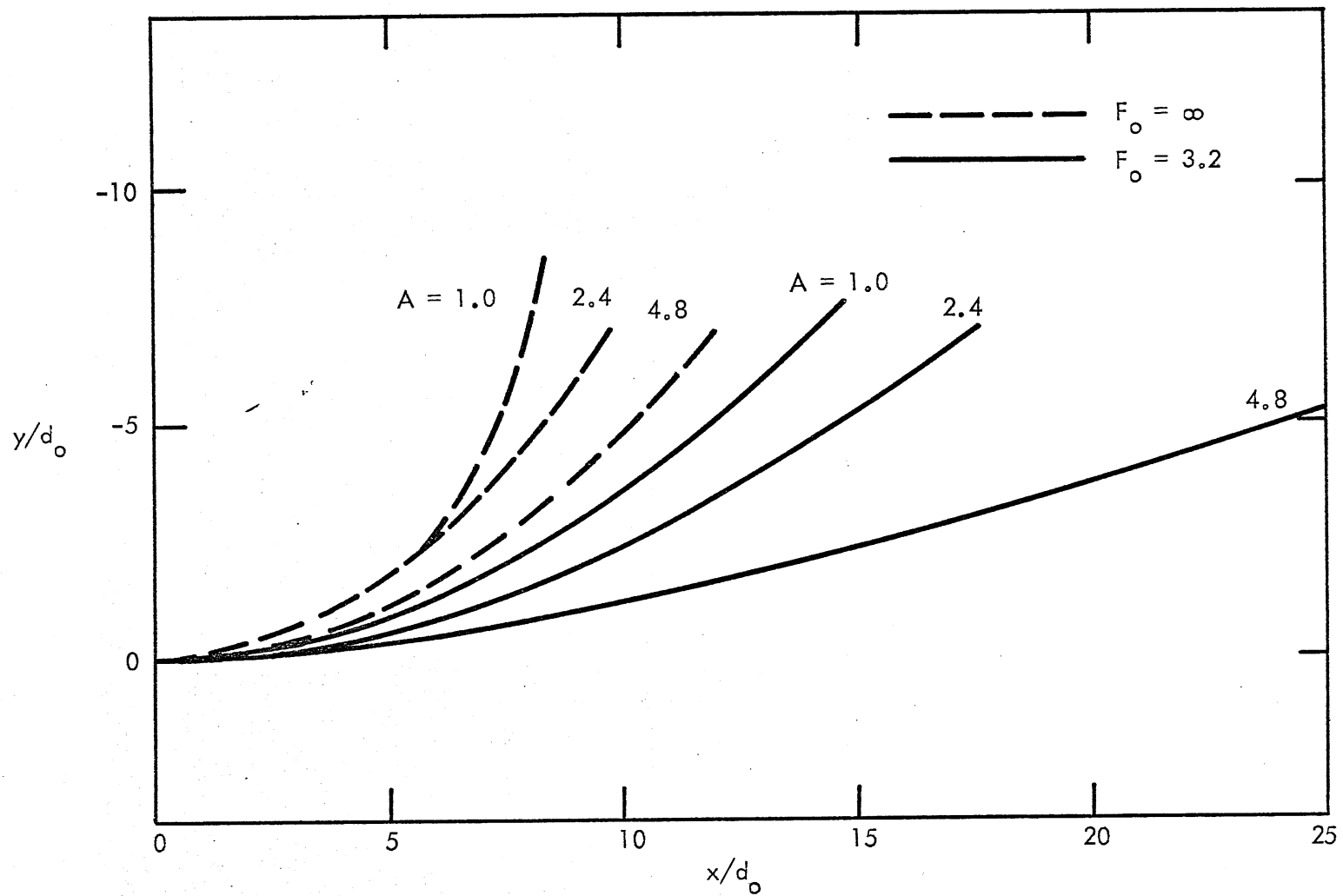


Fig. 30b - Trajectories based on maximum velocity, $A = 1.0, 2.4,$ and 4.8 ; $F_0 = 3.3$ and ∞ ; and $R = 0.41$

not used to determine the ZFE length because of the high background turbulence levels both in the outlet channel and in the cross-flow. It should be recalled that the crossflow turbulence level is 26 per cent. Results are given in Figs. 31 through 33b. The development length has been taken as the distance along the plume centerline (trajectory). Note the decrease in s_o/d_o for an aspect ratio of 2.4 relative to its value for $A = 1.0$ near the outlet. This initial discrepancy disappears farther from the outlet, and by the time the 80 to 85 per cent level is reached, the variation of s_o/d_o with the aspect ratio is nearly linear on log-log paper; i.e., s_o/d_o is proportional to $(A)^n$. The dropoff in x_o/d_o values near $A = 2.4$ was observed previously for the straight discharges. It reflects a rather effective penetration of ambient cold water into the discharged warm water caused by a secondary motion around a horizontal axis, which is apparently favored by the aspect ratio. Isotherm and isoturbulence lines presented in Figs. B-7 through B-9 strongly suggest the existence of such a mechanism, at least in the case of a straight jet discharge. In the presence of a cross-flow, the isotherm pattern is significantly different, but a vortex again forms around a horizontal axis.

The effect of this early mixing at a favorable aspect ratio fades out with increasing distance from the outlet, due to the superposition of other effects, so that at lower excess temperature concentrations of 70 and 60 per cent the channel with $A = 2.4$ no longer shows a trend which is different from those of the other aspect ratios.

It is of some interest to explore whether the end of the ZFE is dominated by vertical or horizontal entrainment of ambient water. As the length of s_o/d_o increases rather drastically with the aspect ratio, one may also wonder whether this trend would come to a halt at a large enough aspect ratio.

It is obvious from the results obtained and from direct observation that at small aspect ratios, horizontal entrainment of cold water by large eddies shed in the free shear zone between the discharged jet and the ambient current is responsible for the ZFE. Figure 27 shows

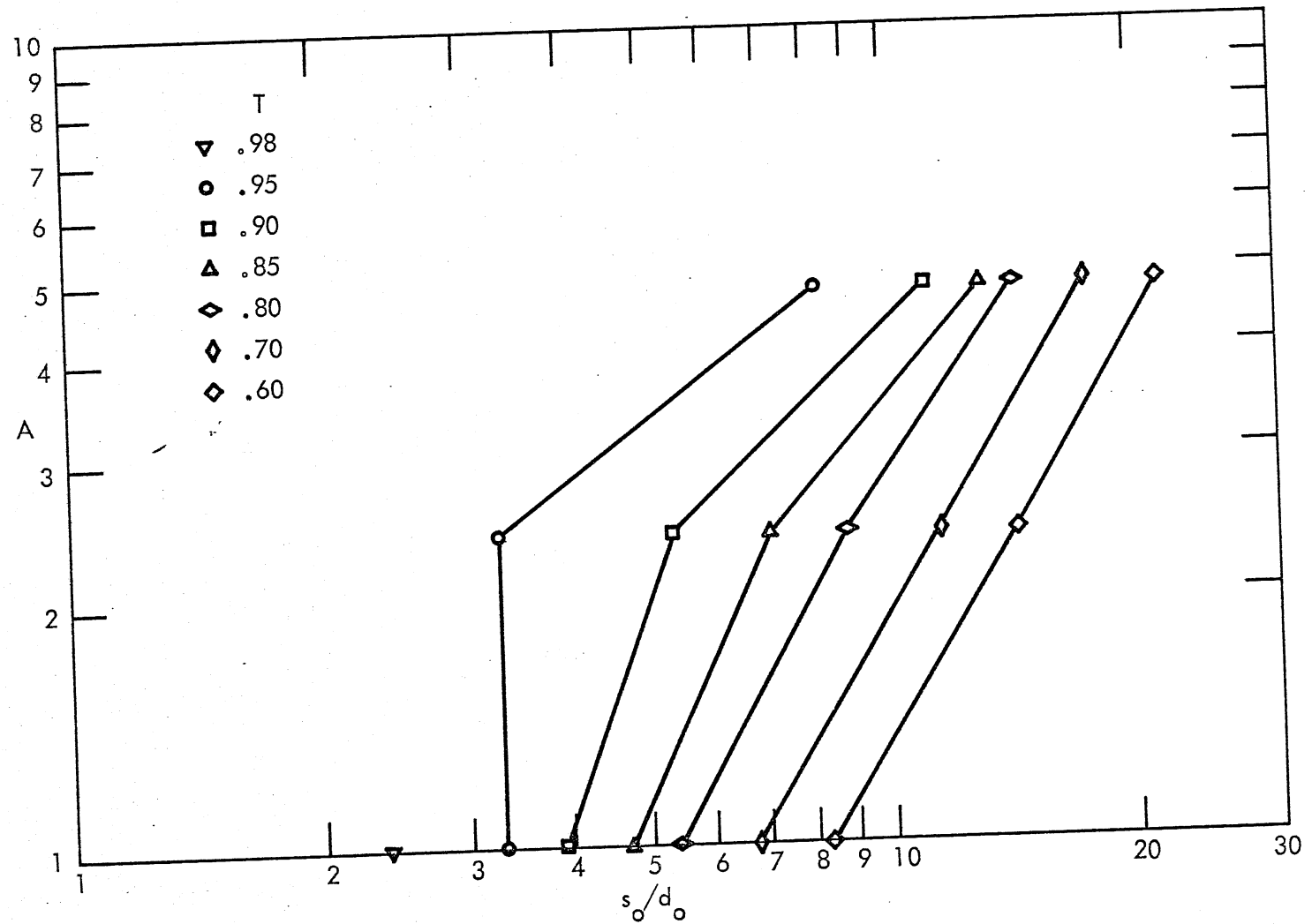


Fig. 31 - s_o/d_o versus A at $F_o = 3.2$, $R = 0.41$, and $T = 0.95, 0.90, 0.85, 0.80, 0.70,$
and 0.60

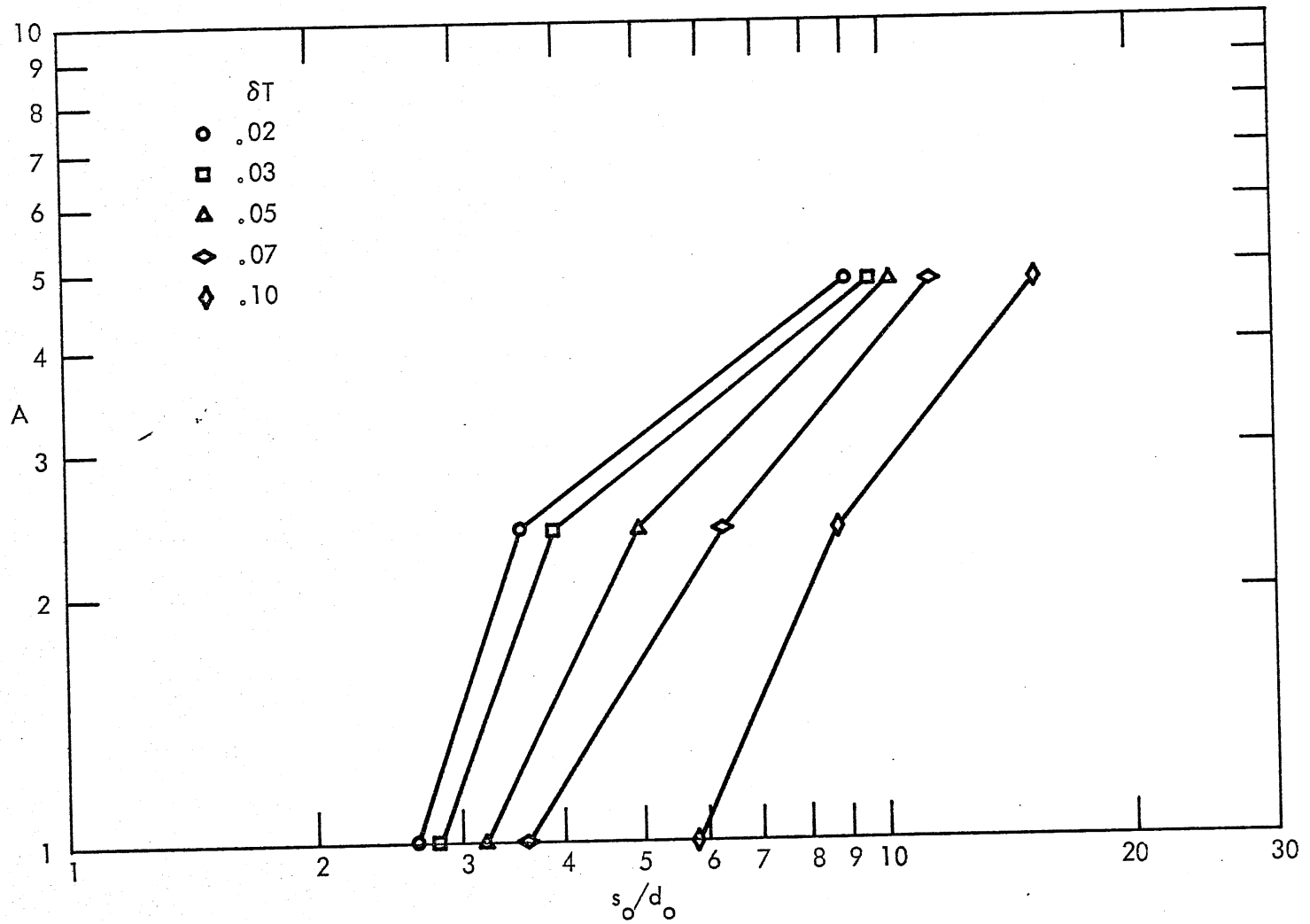


Fig. 32 - s_o/d_o versus A at $F_o = 3.2$, $R = 0.41$, and $\delta T = 0.02, 0.03, 0.05, 0.07$, and 0.10

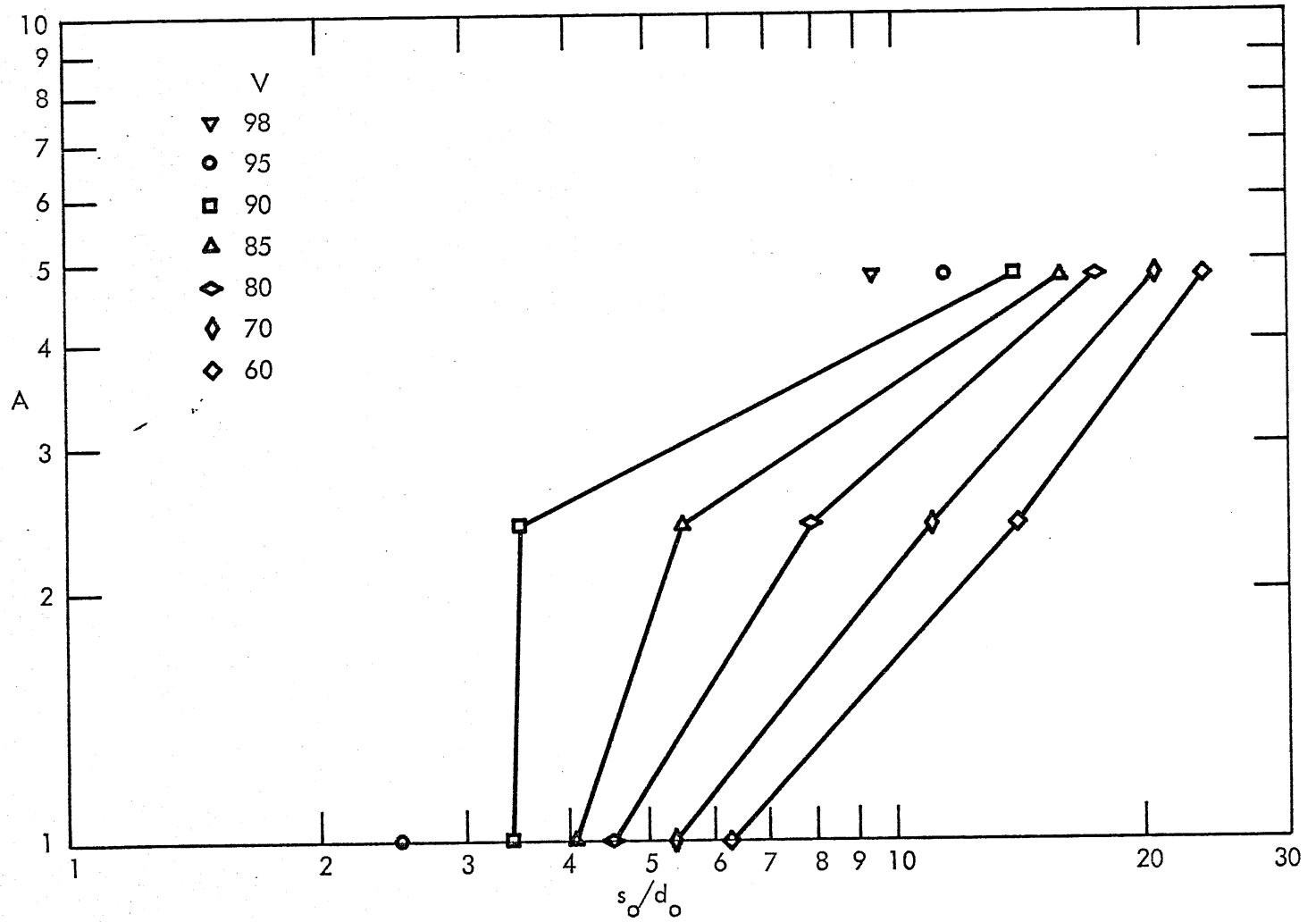


Fig. 33a - s_o/d_o versus A at $F_o = 3.2$, $R = 0.41$, and $V = 0.90, 0.85, 0.80, 0.70$, and 0.60

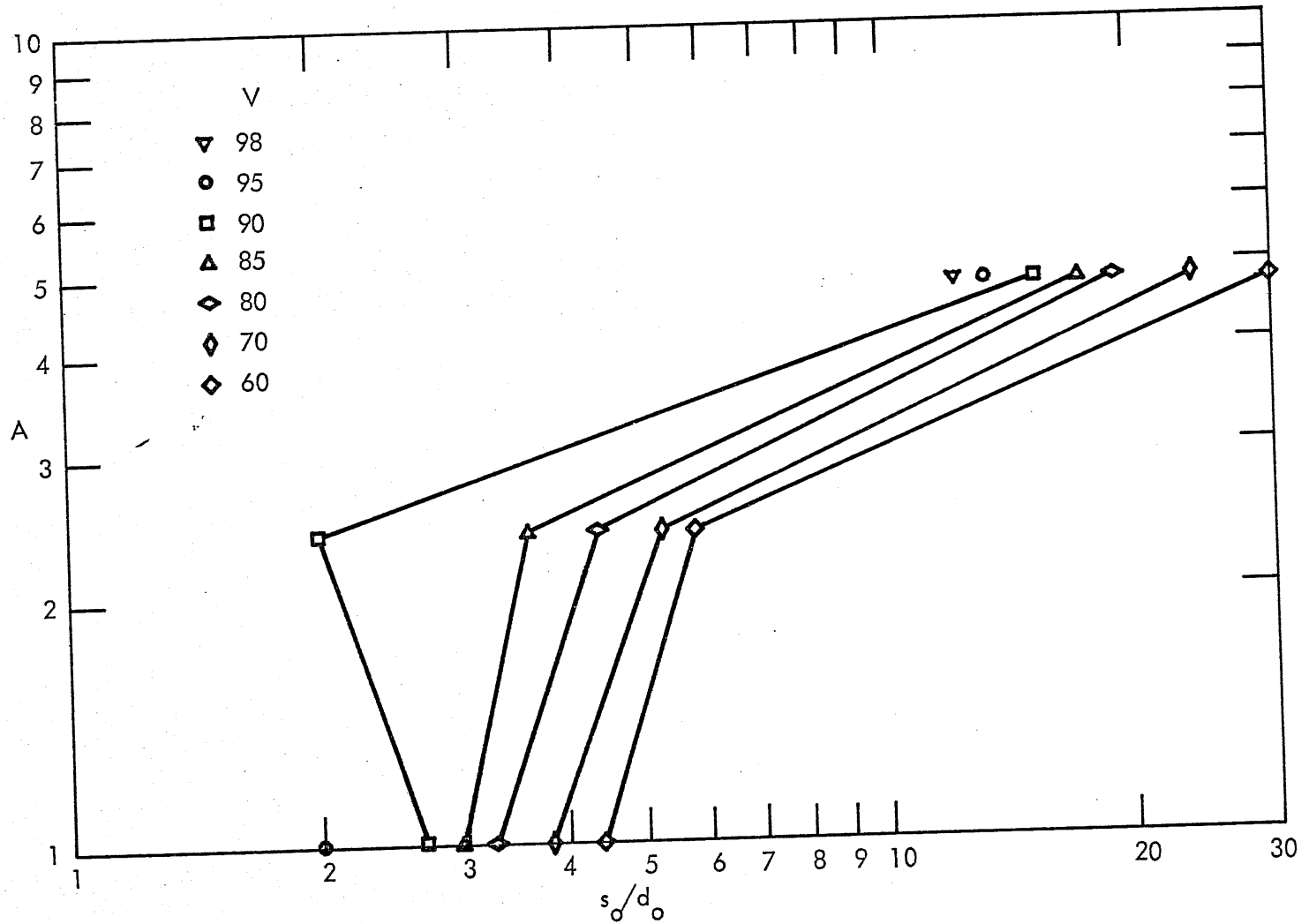


Fig. 33b - s_o/d_o versus A at $F_o = \infty$, $R = 0.41$, and $V = 0.90, 0.85, 0.80, 0.70,$ and 0.60

the formation of these eddies. The axis of these eddies is not vertical, but bent over and entrained by the cross-flow underneath the discharged jet as shown in Fig. 34 (photo), so that horizontal and vertical entrainment and mixing are linked by the same eddies. It can therefore be expected that at small aspect ratios and closer to the outlet--i.e., for $T = 0.95$ or 0.90 or 0.85 --the horizontal entrainment is the limiting mechanism. Farther downstream, vertical entrainment is very important as well. Whether there is a limit to the value of s_o/d_o cannot really be determined on the basis of the available data. It should also be pointed out that the cross-flow has two opposing effects on s_o ; one is to lengthen the ZFE by adding a transverse (lateral) velocity component to the flow, and the other is to increase the mixing intensity. The end of the ZFE usually falls into the fairly straight portion of the trajectory, and therefore the effect of the cross-flow on the length of the ZFE will be seen to be essentially a slight shortening effect.

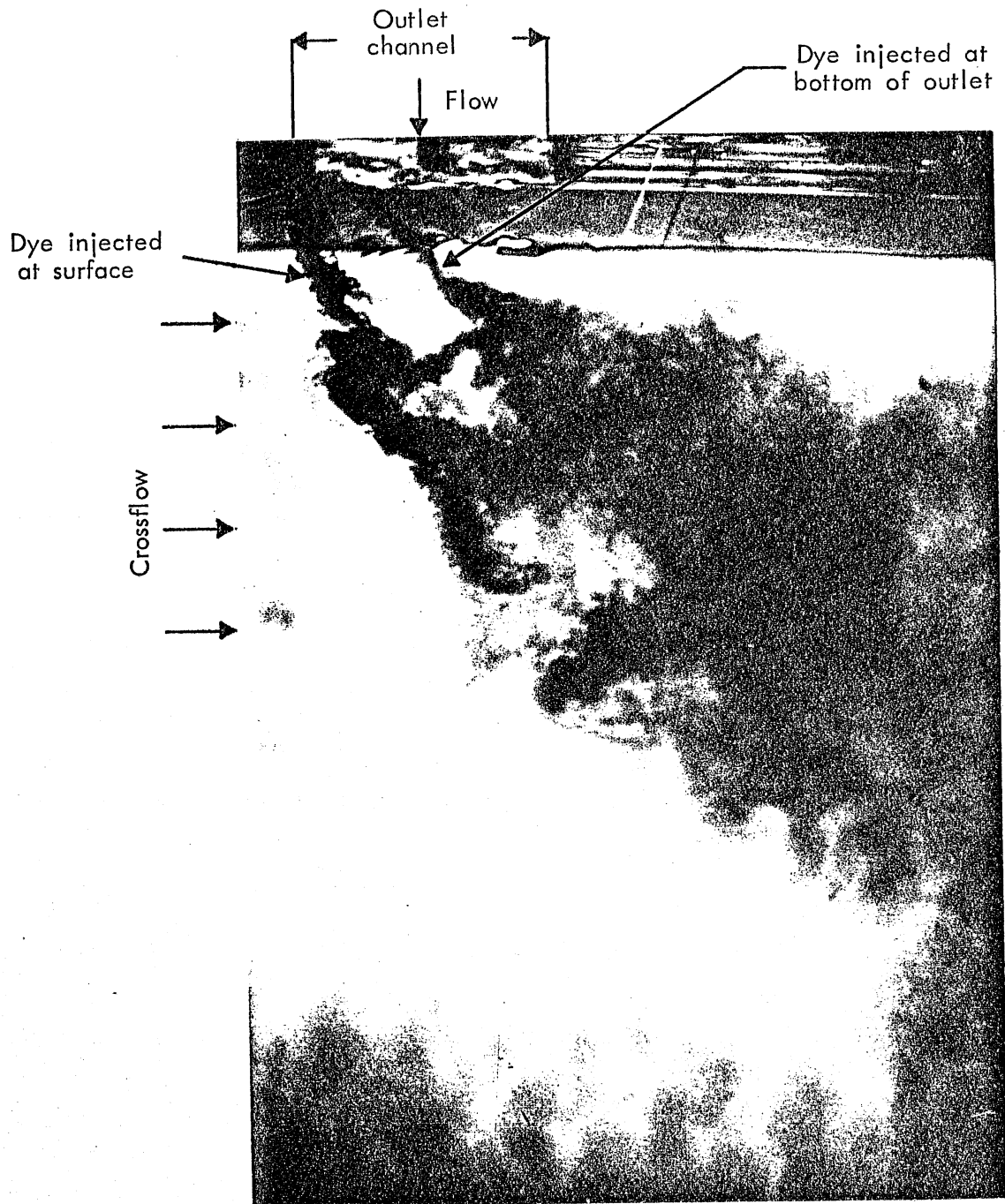


Fig. 34 - Photograph of dye patterns near the outlet of a discharge into a crossflow - $A = 2.4$, $F_o = \infty$, $R = 0.41$

SECTION VII
 ANALYTICAL EXPRESSIONS FOR ESTABLISHMENT LENGTH
 AND INITIAL FLOW RATES

LENGTH OF THE ZONE OF FLOW ESTABLISHMENT

The relationship sought is of the basic form

$$f\left(\frac{s_o}{d_o}, F_o, A, T, R\right) = 0 \quad (11)$$

The function f has been studied by several investigators. Motz and Benedict² expressed it in the form

$$\frac{x_o}{d_o} = 2.2 A \quad (12)$$

where x_o is the x-projection of the distance s_o measured along the trajectory. Prych⁴ simply used the relationship

$$x_o = 4D_o \quad (13)$$

where D_o is the equivalent diameter of a semicircular outlet channel. The relationship was rewritten by Shirazi and Davis⁵ as

$$\frac{s_o}{d_o} = 6.38 A^{1/2} \quad (14)$$

Shirazi and Davis⁵ proposed the relationship

$$\frac{x_o}{d_o} = 5.4 A^{2/3} F_o^{-1/3} \quad (15)$$

Equation (15) can be used only for $F_o < 10$. It gives $x_o = 0$ when $F_o \rightarrow \infty$.

The effect of a cross-flow on s_o was expressed by Fan¹² for circular, fully submerged jets, previously investigated by Gordier¹³, as

$$\frac{s_o}{D_o} = 6.2 \exp(-3.32 R) \quad (16)$$

Shirazi¹⁴ specified a function f of the form

$$f(o) = \exp^a \left(\frac{x}{d_o} \right)^b R^c F_o^d A^e \lambda^f \alpha^g \quad (17)$$

where $f(o)$ is a desired plume characteristic--for example, T ; λ is the slope of the beach over which the discharge is made; and α is the discharge angle with respect to the current. Laboratory and field data, taken from different sources and covering some of the independent variables in a not-very-coherent way, were assembled. Multiple regression analysis was applied to individual data separately and to one or more sets in combination to obtain the constants. Results based on excess temperature T were as follows⁸:

Group I: Discharge into deep stagnant pool

$$T = \exp^a \left(\frac{x}{d_o} \right)^{-0.57} R^0 F_o^{-0.32} A^{0.53} \quad (18)$$

$$-0.1 < a < 2.5$$

Group II: Discharge into a stagnant pool over a sloping shore

$$T = \exp^a \left(\frac{x}{d_o} \right)^{-0.47} R^0 F_o^{-0.22} A^{0.372} \lambda^{0.33} \quad (19)$$

$$0.77 < a < 1.46$$

Group III: Discharge into a deep moving flow

$$T = \exp^a \left(\frac{x}{d_o} \right)^{-0.45} R^{0.37} F_o^{-0.36} A^{0.23} \alpha^{-0.35} \quad (20)$$

$$0.36 < a < 4.06$$

The data previously obtained in the same tank as was used for this study and reported by Stefan, Hayakawa, and Schiebe³ gave, for Group I and $A = 3.07$,

$$T = \exp^a \left(\frac{x}{d_o} \right)^{-0.51} F_o^{0.03} \quad (21)$$

In the analysis of the experimental data collected under the present study it seemed advisable to again use separation of the variables. However, enough data had been collected to attempt formulations which would fit a scheme of the form

$$f_1\left(\frac{s_o}{d_o}\right) f_2(T) f_3(A) f_4(F_o) f_5(R) = 0 \quad (22)$$

or even more complicated functions of several independent variables. In pursuing this idea, it was found that the strongest dependence of s_o/d_o values at specified levels of T seemed to be with respect to A . A plot of $\log A$ versus $\log(s_o/d_o)$ such as that shown in Fig. 31 for $R = 0.41$ shows an approximately linear relationship, particularly at $T = 0.8$ and below. A similar plot for the straight jet data ($R = 0$) was made using the data from Figs. 14a, b, c, and d, and the result was found to be nearly the same. An appropriate functional relationship therefore seemed to be

$$\frac{s_o}{d_o} = KA^n \quad (23)$$

From the graphs $n \approx 0.5$ was found to best fit time-averaged water temperature data for both straight and curvilinear jets at $T = 0.9$; $n \approx 0.6$ for $T = 0.80$. Water temperature fluctuation data at $T = 0.10$ produced a value of $n \approx 0.6$. While values of n seemed fairly independent of R , K values differed by a factor of approximately 1.4 when R was changed from 0 to 0.41. The straight flow produced the larger K , and thus the greater development length. Subsequently it was found that for all the data collected, a relationship existed between K and n that could be cast into the form

$$K^{1/\alpha} = \gamma/n \quad (24)$$

The data are shown in Fig. 35. α was found to be nearly constant and to equal approximately 1.3. An approximate linear fit for $\gamma(T)$ was

$$\gamma = \phi + \psi T \quad \text{for} \quad 0.8 \leq T \leq 0.95 \quad (25)$$

$$\phi = 8.2 \quad \text{and} \quad \psi = -7.0$$

as shown in Fig. 36. No significant influence of R or F_0 on γ could be established with the available data.

Substitution of the above relationships gives

$$\frac{s_0}{d_0} = f_2(T) f_3(A) = (\phi + \psi T)^\alpha A^n \quad (26)$$

The remaining functions to be specified are $f_4(F_0)$ and $f_5(R)$. We shall use $f_5(R) = \exp(\eta R)$, with η being on the order of -0.9 for $0 \leq R \leq 0.41$. The form of the function f_4 will be derived from the data for $A = 1$.

$$f_4(F_0) = 1 + \frac{\epsilon F_0 + \beta}{\exp(\delta F_0)} \quad \text{for} \quad F_0 \geq 1 \quad (27)$$

The coefficients $\epsilon = 0.5$, $\beta = -1.5$, and $\delta = 0.4$ provide an acceptable fit to the data. Equation (27) has a maximum at $F_0 = \frac{-\beta}{\epsilon} + \frac{1}{\delta}$. The asymptotic values of f_4 are $f_4(1) = 1 + \frac{\epsilon + \beta}{\delta}$ and $f_4(\infty) = 1$.

The format of the complete empirical equation, then, is

$$\frac{s_0}{d_0} = (\phi + \psi T)^\alpha A^n e^{\eta R} \left(1 + \frac{\epsilon F_0 + \beta}{\exp(\delta F_0)} \right) \quad (28)$$

derived from data in the following ranges:

$$0.8 \leq T \leq 0.98$$

$$2.0 \leq F_0 \leq 15.0$$

$$0 \leq R \leq 0.41$$

$$1.0 \leq A \leq 9.6$$

As already indicated, the coefficients ϕ , ψ , n , α , β , ϵ , δ , and η were first read from graphs. They were improved upon through non-linear curve-fitting analysis. The numerical values obtained were

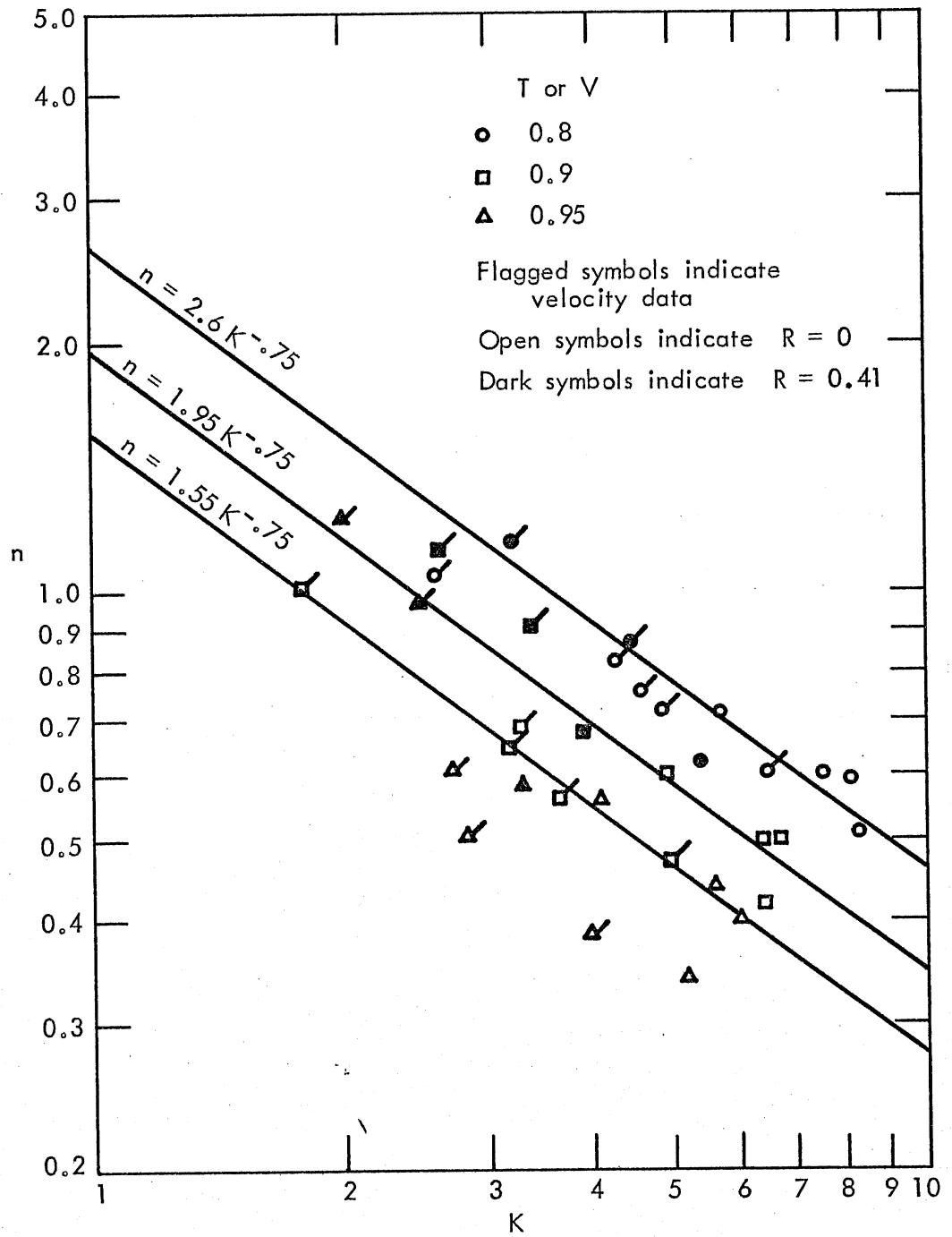


Fig. 35 - n versus K

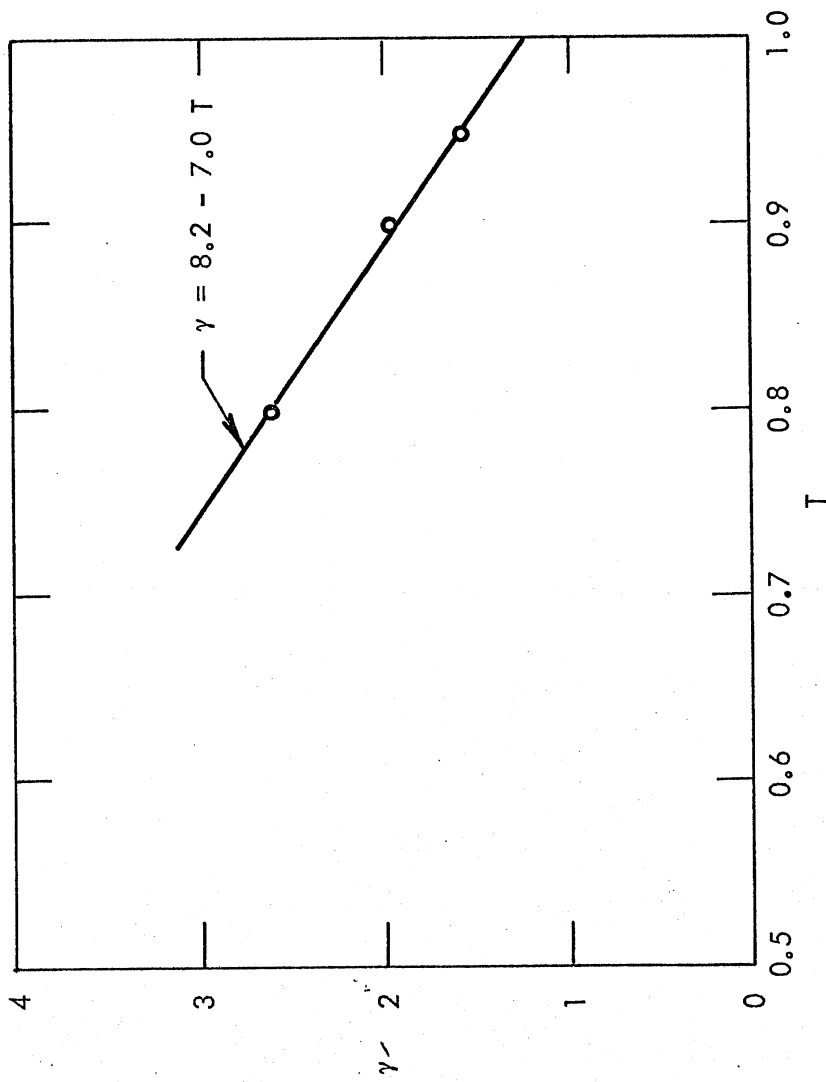


Fig. 36 - γ versus T

$\phi = 16.0$, $\psi = -12.8$, $n = 0.46$, $\alpha = 1.2$, $\beta = -1.50$, $\epsilon = 0.50$,
 $\delta = 0.40$, and $\eta = -0.9$. Here n is not really a constant, but is somewhat dependent on the temperature level T . A modified version of Eq. (28) in which $n = \text{constant}$ was replaced by

$$n = n_1 + n_2 T$$

was also investigated. The numerical coefficients obtained by non-linear curve-fitting for the modified Eq. (28) were $n_1 = 0.85$ and $n_2 = -0.44$.

The modified Eq. (28) no longer fits the general format of Eq. (22). At that level of approximation, many different solutions are possible. Substituting the above numbers in Eq. (28) gives the final dimensionless equation for the length of the zone of flow establishment:

$$\frac{s_o}{d_o} = (16.0 - 12.8 T)^{1.2} A^{0.85 - 0.44T} e^{-0.9R} \left(1 + \frac{0.50 F_o - 1.50}{0.4 F_o} \right) \quad (29)$$

A value of $T = 0.90$ is thought to represent a meaningful choice to designate the end of the ZFE. For this value the above equation becomes

$$\frac{s_o}{d_o} = 6.05 A^{0.46} e^{-0.9R} \left(1 + \frac{0.50 F_o - 1.50}{0.4 F_o} \right) \quad (30)$$

Approximations beyond Eq. (28) produce only minor improvements unless vast amounts of data are available. The non-linear curve-fitting program was conducted with 85 data points. Such a number does not justify higher order approximations beyond Eqs. (22) and (28).

INITIAL ENTRAINMENT FOR STRAIGHT JETS

Empirical flow rate equations are needed only for the ZFE, since the fully developed flow region can be handled readily by mathematical models. The available data justify the derivation of empirical equations only for straight jets. The relationships given by Albertson, et al.⁶ may serve as a guide in formulating the equations. Outlet shape (aspect ratio A)

and outlet densimetric Froude number (F_o) must be incorporated into the formulations. For fully submerged axisymmetric and slot jets, respectively, Albertson, et al.⁶ have given the following relationships for the volumetric flow rates:

$$\text{within the ZFE: } \frac{Q}{Q_o} = 1 + 0.083 \frac{x}{2d_o} + 0.0128 \left(\frac{x}{2d_o}\right)^2 \quad (31a)$$

$$\frac{Q}{Q_o} = 1 + 0.080 \frac{x}{2d_o} \quad (31b)$$

in the fully established flow region:

$$\frac{Q}{Q_o} = 0.32 \frac{x}{2d_o} \quad (32a)$$

$$\frac{Q}{Q_o} = 0.62 \left(\frac{x}{2d_o}\right)^{0.5} \quad (32b)$$

For rectangular outlets of variable aspect ratio A , a format of the equation is sought that will degenerate into those given above when $A \rightarrow 2$ or $A \rightarrow \infty$. Because of free surface and shape effects, the coefficients should be expected to be different from those given in the above equations.

The F_o effect can be cast into a coefficient of the form $(1 - \frac{c_3}{F_o^q})$ where $c_3 \approx 0.5$ and $q \approx 0.4$. With this provision, the data shown in Fig. 25 will replot on a single line. The effect of A will be incorporated in the coefficients c_1 , c_2 , and p in the equation

$$\frac{Q}{Q_o} = 1 + [c_1 \left(\frac{x}{2d_o}\right) + c_2 \left(\frac{x}{2d_o}\right)^p] \left(1 - \frac{c_3}{F_o^q}\right) \quad (33)$$

Values of c_1 , c_2 , and p must be derived from the data. Using a non-linear curve-fitting technique, the following coefficients were found to provide a good match of the data: $c_1 = 0$; $c_2 = 0.087$; and $p = \frac{2.35 + 0.75A}{0.90 + A}$. The final empirical equation for volumetric flow

rates of straight jets near the outlet is

$$\frac{Q}{Q_0} = 1 + \left[0.087 \left(\frac{x}{2d_0} \right)^{\frac{2.35 + 0.75A}{0.90 + A}} \right] \left[1 - \frac{0.52}{F_0^{0.41}} \right] \quad (34)$$

Experimental data from which the above relationship was derived covered the ranges $1 \leq A \leq 9.6$ and $F_0 \geq 1.8$. The equation is valid near the outlet, within the ZFE, and somewhat beyond the ZFE.

REFERENCES

1. Stolzenbach, K. D. and D. R. F. Harleman. An Analytical and Experimental Investigation of Surface Discharges of Heated Water. Water Pollution Control Research Series, U.S. Environmental Protection Agency, 16130 DJV 02/71. (Also: Stolzenbach, K. D. and D. R. F. Harleman. Three-Dimensional Heated Surface Jets. Water Resources Research. Vol. 9, No. 1, February 1973, p. 129-137.)
2. Motz, L. H. and B. A. Benedict. Heated Surface Jet Discharged into a Flowing Ambient Stream. Water Pollution Control Research Series, U.S. Environmental Protection Agency, 16130 FDQ 03/71. March 1971.
3. Stefan, H., N. Hayakawa, and F. R. Schiebe. Surface Discharge of Heated Water. Water Pollution Control Research Series, U.S. Environmental Protection Agency, 16130 FSU 12/71. (Also: Stefan, H. and P. Vaidyaraman. Jet-Type Model for the Three-Dimensional Thermal Plume in a Cross-Current and Under Wind. Water Resources Research. Vol. 8, No. 4, 1972. p. 998-1014.)
4. Prych, E. A. A Warm Water Effluent Analyzed as a Buoyant Surface Jet. Sveriges Meteorologiska och Hydrologiska Institut, Stockholm. Report No. 21. 1972.
5. Shirazi, M. A. and L. R. Davis. Workbook of Thermal Plume Prediction - Vol. 2 - Surface Discharge. Environmental Protection Technology Series, U.S. Environmental Protection Agency, R2-72-005b, May 1974.
6. Albertson, M. L., Y. B. Dai, R. A. Jensen, and H. Rouse. Diffusion of Submerged Jets. Transactions, ASCE. Vol. 115, 1950. p. 639-697.
7. Hirst, E. Zone of Flow Establishment for Round Buoyant Jets. Water Resources Research. Vol. 8, No. 5, October 1972. p. 1234-1246.
8. Shirazi, Mostafa A. A Critical Review of Laboratory and Some Field Experimental Data on Surface Jet Discharge of Heated Water. Pacific Northwest Environmental Research Laboratory, Corvallis, Oregon. Working Paper No. 4. 1973.
9. Dornhelm, R., M. Nouel, and R. L. Wiegel. Velocity and Temperature in a Buoyant Jet. Jrl. Power Div. ASCE. Vol. 98, No. P01, June 1972. p. 29-47.
10. Tamai, N., R. L. Wiegel, and G. F. Tornberg. Horizontal Surface Discharge of Warm Water Jets. Jrl. Power Div., ASCE. October 1969. p. 253.
11. Jen, Y., R. L. Wiegel, and I. Mobarek. Surface Discharge of Horizontal Warm Water Jet. Jrl. Power Div., ASCE. Vol. 92, No. P02, April 1966. p. 1-28.

12. Fan, Loh-Nien. Turbulent Buoyant Jets into Stratified or Flowing Ambient Fluids. W. M. Keck Laboratory of Hydraulics and Water Resources, California Institute of Technology. Technical Report No. KH-R-15. June 1967. 196 p.
13. Gordier, R. L. Studies on Fluid Jets Discharging Normally into Moving Liquid. St. Anthony Falls Hydraulic Laboratory, University of Minnesota. Technical Paper No. 28-B. 1959. 48 p.
14. Shirazi, M. A. Some Results from Experimental Data on Surface Jet Discharge of Heated Water. Proceedings, First World Congress on Water Resources, International Water Resources Association, Chicago, October 1973.
15. Schuyf, J. P. The Measurement of Turbulent Velocity Fluctuations with a Propeller-Type Current Meter. Journal of Hydraulic Research. Vol. 4, No. 2. 1966.

RESULTING PUBLICATIONS

1. Experimental Heated Surface Jet Studies, by H. Stefan, E. Mroska, and L. Bergstedt. Presented at 55th Annual Meeting of the American Geophysical Union, Washington, D.C., April 1974 (oral presentation only).

PAST PUBLICATIONS RELATING TO THE SUBJECT

1. Modeling Spread of Heated Water over Lake, by H. Stefan. Jrl. Power Div., ASCE. Vol. 96, No. PO3, June 1970. p. 469-482.
2. Stratification of Flow from Channel into Deep Lake, by H. Stefan. Jrl. Hydr. Div., ASCE. Vol. 96, No. HY7, July 1970. p. 1417-1434.
3. Heated Discharge from Flume into Tank, by H. Stefan and F. R. Schiebe. Jrl. San. Engr. Div., ASCE. Vol. 96, No. SA6, December 1970. p. 1415-1433.
4. Physical (Hydraulic) Modeling of Heat Dispersion in Large Lakes, A Review of the State of the Art, by E. Silberman and H. Stefan. St. Anthony Falls Hydraulic Laboratory, University of Minnesota. Project Report No. 115. 1970.
5. Dilution of Buoyant Two-Dimensional Surface Discharges, by H. Stefan. Jrl. Hydr. Div., ASCE. Vol. 98, No. HY1, January 1972. p. 71-86.
6. Mixing Induced by an Internal Hydraulic Jump, by H. Stefan and N. Hayakawa. Water Resources Bulletin, American Water Resources Association. Vol. 8, No. 3, June 1972. p. 531-545.
7. Jet Type Model for the Three-Dimensional Thermal Plume in a Cross-current and Under Wind, by H. Stefan and P. Vaidyaraman. Water Resources Research. Vol. 8, No. 4, August 1972. p. 998-1014.
8. Impact of Cooling Water on Lake Temperatures, by H. Stefan, C.-S. Chu, and W. Ho. Jrl. Power Div., ASCE. Vol. 98, No. PO2, October 1972. p. 253-272.

SYMBOLS AND UNITS

- A = aspect ratio
- c_1)
 c_2) = coefficients related to various functions for entrainment
 c_3) coefficient
- D_h = hydraulic diameter of discharge channel [ft]
- D_o = diameter of outlet channel [ft]
- d_o = depth of discharge channel [ft]
- F_o = densimetric Froude number
- g = acceleration of gravity [32.2 ft sec⁻²]
- Q = volumetric flow rate [ft³ sec⁻¹]
- R = cross-flow velocity ratio
- Re_o = Reynolds number
- r = distance from and perpendicular to main trajectory [ft]
- s = distance from outlet along main trajectory [ft]
- s_o = length of zone of flow establishment along main trajectory [ft]
- T = time-averaged excess temperature ratio
- T_o = discharge temperature at the outlet [°F]
- T_a = ambient water temperature in the lake or reservoir [°F]
- U_a = average ambient crossflow velocity [ft sec⁻¹]
- U_o = average discharge velocity [ft sec⁻¹]
- U = flow velocity [ft sec⁻¹]
- V = time-averaged velocity ratio
- w_o = width of discharge channel [ft]
- x = coordinate parallel to outlet centerline [ft]
- x_o = length of zone of flow establishment [ft]
- y = coordinate perpendicular to outlet centerline [ft]
- z = depth [ft]

SYMBOLS AND UNITS (Continued)

α = discharge angle with respect to cross-flow

σ = standard deviation

ν = kinematic viscosity [$\text{ft}^2 \text{sec}^{-1}$]

λ = slope of beach

ρ = density of water [slugs ft^{-3}]

ϕ = lateral spread angle of shear zone [degrees]

n

α

γ

Φ

η

β

δ

ψ

} = coefficients related to various functions for length of zone of flow establishment

Subscripts

a = ambient water

c = cross-flow

l = local

m = maximum

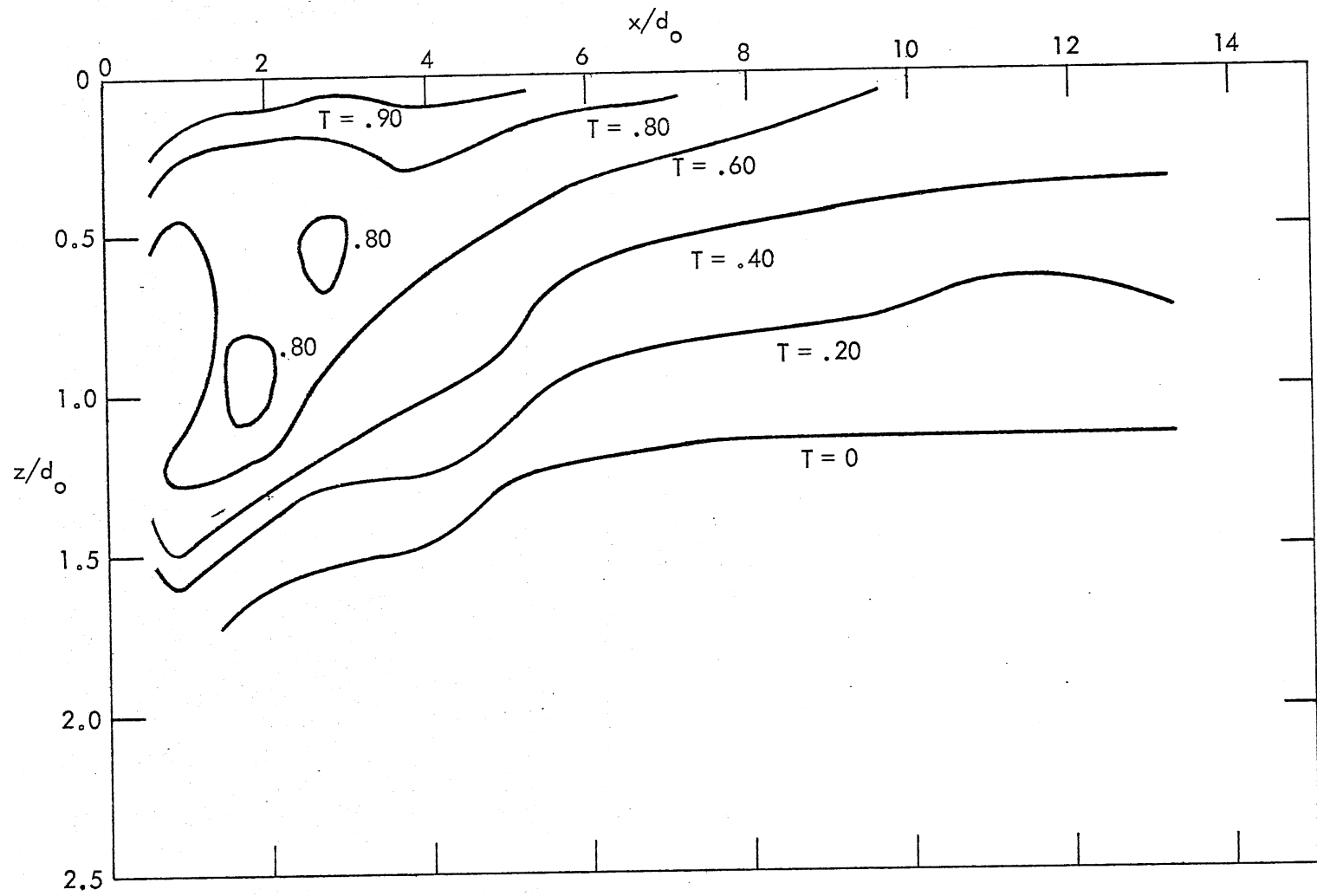
o = initial value, outlet

Appendix A

ISOTHERMS $T = \text{constant}$ and $\delta T = \text{constant}$
IN VERTICAL SECTIONS ALONG JET AXIS OR PERPENDICULAR TO IT,
 $A = 2.4, A = 9.6, R = 0$

FIGURES -- APPENDIX A

<u>No.</u>	<u>Page</u>
A-1	117
Vertical Temperature Profile along Jet Axis - $A = 2.4$, $F_o = 2.2$, $R = 0$	
A-2	118
Vertical Temperature Profile along Jet Axis - $A = 2.4$, $F_o = 3.85$, $R = 0$	
A-3	119
Vertical Temperature Profile along Jet Axis - $A = 2.4$, $F_o = 15.8$, $R = 0$	
A-4	120
Vertical Temperature Fluctuation Profile along Jet Axis - $A = 2.4$, $F_o = 2.2$, $R = 0$	
A-5	121
Vertical Temperature Fluctuation Profile along Jet Axis - $A = 2.4$, $F_o = 3.85$, $R = 0$	
A-6	122
Vertical Temperature Fluctuation Profile along Jet Axis - $A = 2.4$, $F_o = 15.8$, $R = 0$	
A-7	123
Vertical Temperature Profile Perpendicular to Jet Axis - $A = 2.4$, $F_o = 2.2$, $R = 0$, $x/d_o = 1.8$	
A-8	124
Vertical Temperature Profile Perpendicular to Jet Axis - $A = 2.4$, $F_o = 3.85$, $R = 0$, $x/d_o = 1.8$	
A-9	125
Vertical Temperature Profile Perpendicular to Jet Axis - $A = 2.4$, $F_o = 15.8$, $R = 0$, $x/d_o = 1.7$	
A-10	126
Vertical Temperature Profile along Jet Axis - $A = 9.6$, $F_o = 2.15$, $R = 0$	
A-11	127
Vertical Temperature Profile along Jet Axis - $A = 9.6$, $F_o = 4.1$, $R = 0$	
A-12	128
Vertical Temperature Fluctuation Profile along Jet Axis - $A = 9.6$, $F_o = 2.15$, $R = 0$	
A-13	129
Vertical Temperature Fluctuation Profile along Jet Axis - $A = 9.6$, $F_o = 4.1$, $R = 0$	
A-14	130
Vertical Temperature Profile Perpendicular to Jet Axis - $A = 9.6$, $F_o = 2.15$, $R = 0$, $x/d_o = 1.9$	
A-15	131
Vertical Temperature Profile Perpendicular to Jet Axis - $A = 9.6$, $F_o = 4.1$, $R = 0$, $x/d_o = 1.9$	



117

Fig. A-1 - Vertical temperature profile along jet axis - $A = 2.4$, $F_o = 2.2$, $R = 0$

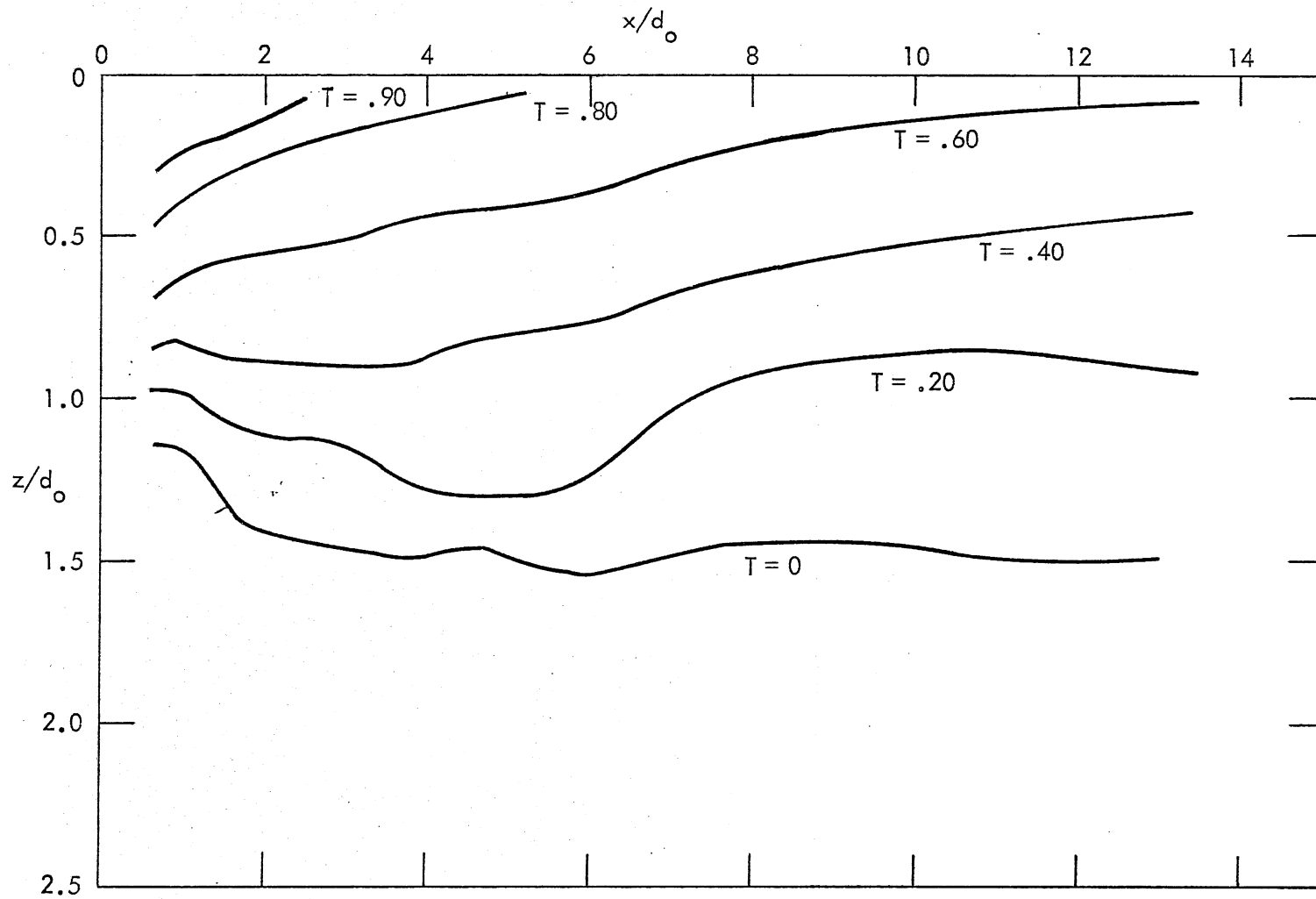


Fig. A-2 - Vertical temperature profile along jet axis - $A = 2.4$, $F_0 = 3.85$, $R = 0$

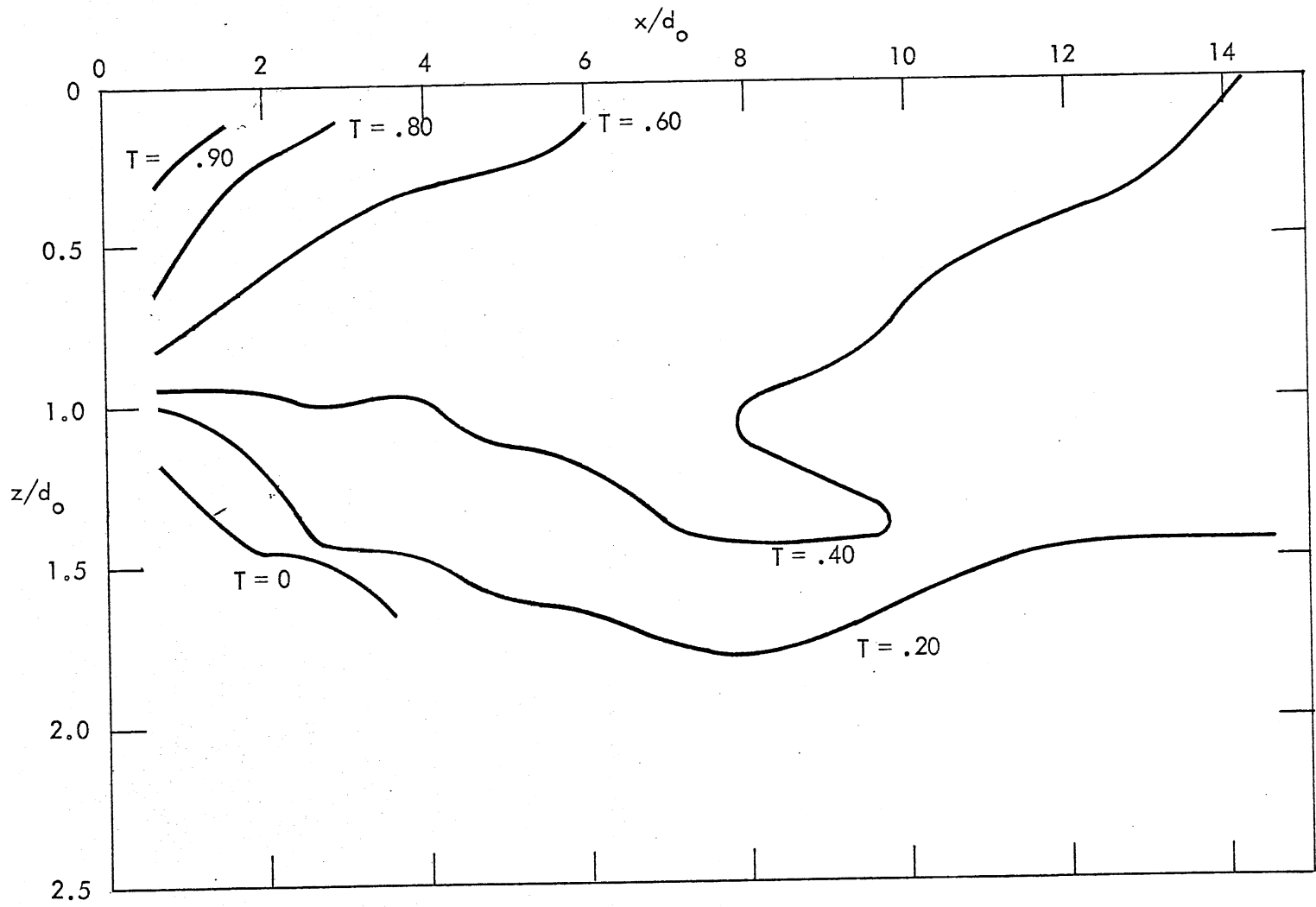


Fig. A-3 - Vertical temperature profile along jet axis - $A = 2.4$, $F_0 = 15.8$, $R = 0$

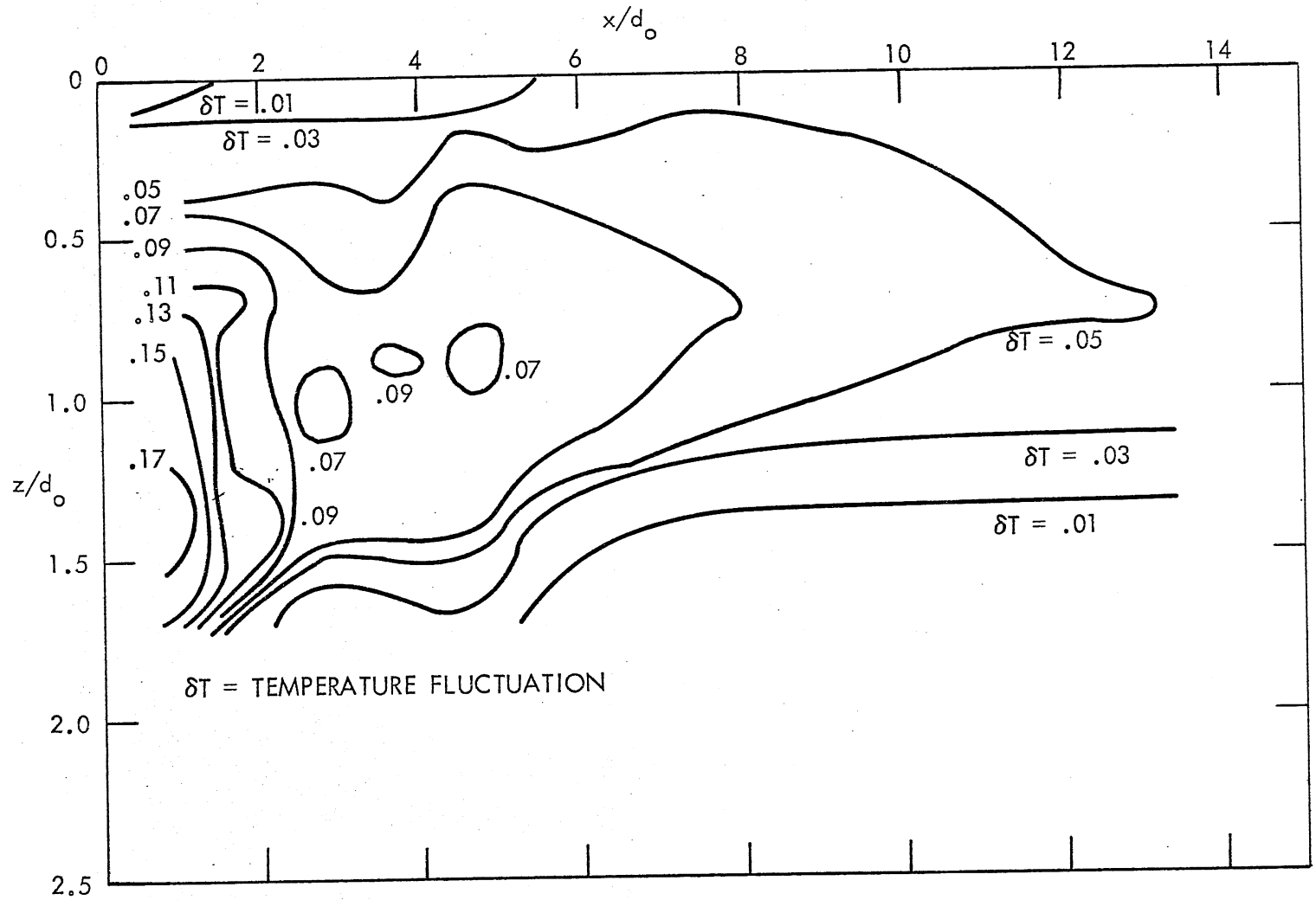


Fig. A-4 - Vertical temperature fluctuation profile along jet axis - $A = 2.4$, $F_0 = 2.2$, $R = 0$

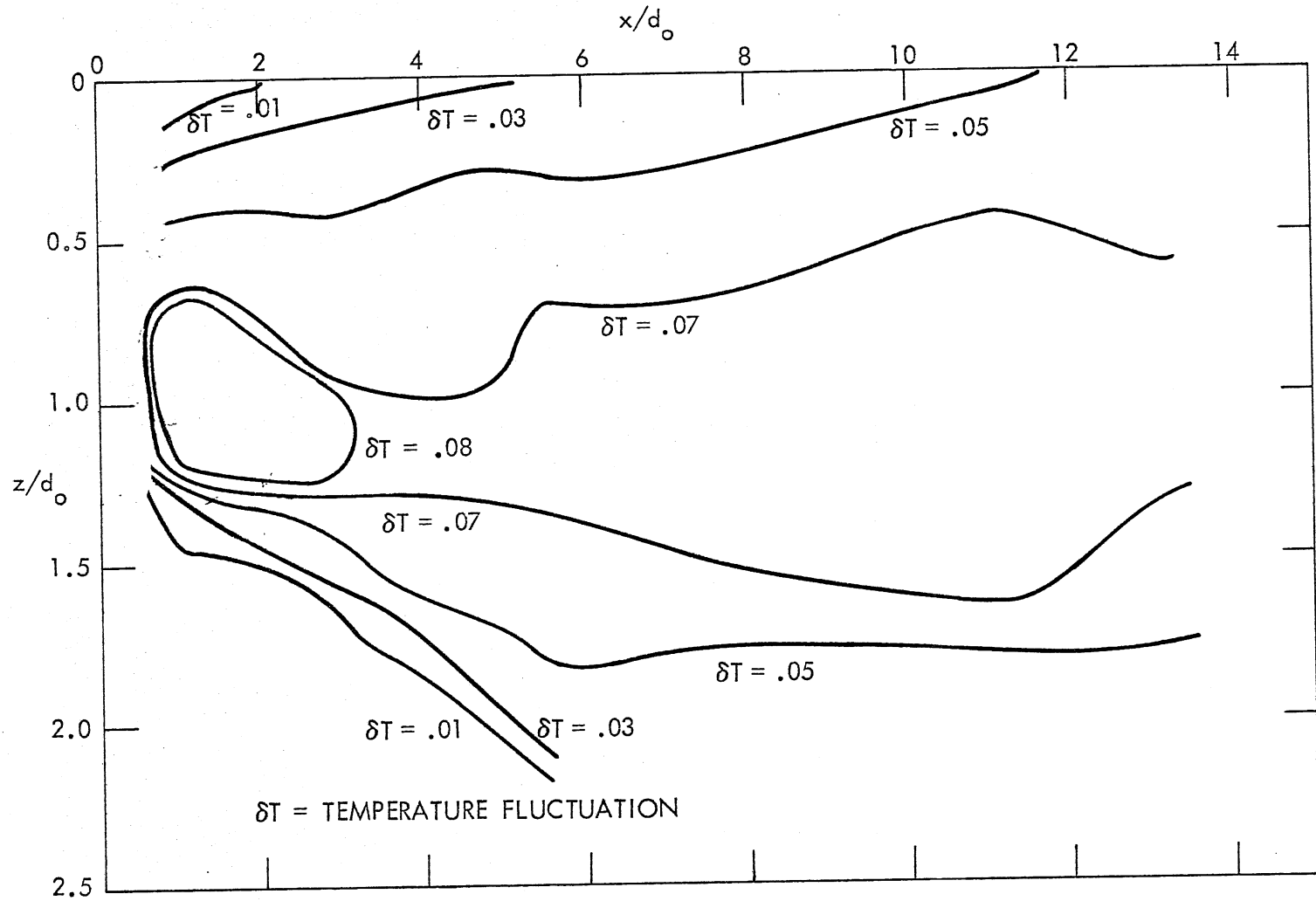


Fig. A-5 - Vertical temperature fluctuation profile along jet axis - $A = 2.4$, $F_o = 3.85$, $R = 0$

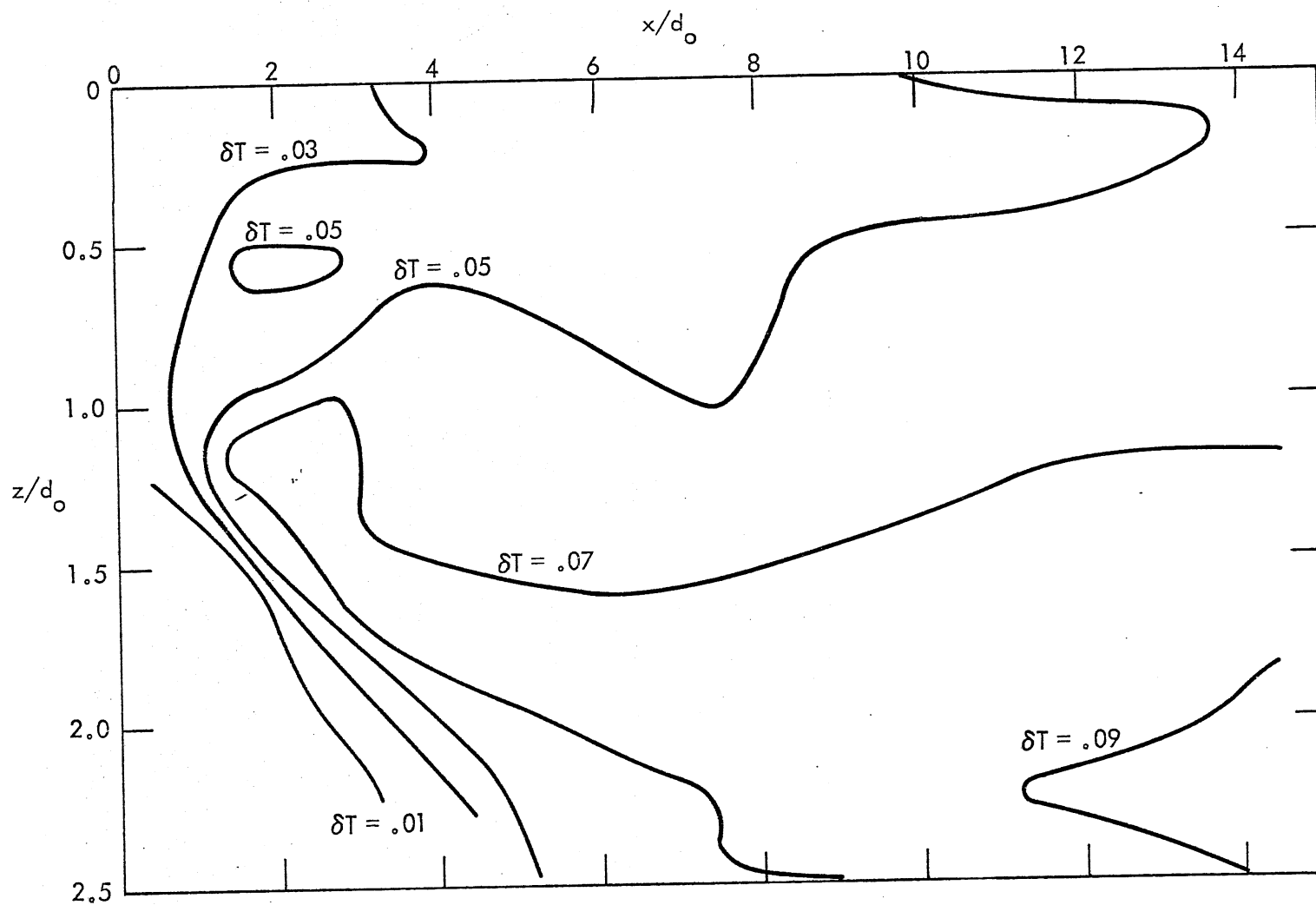
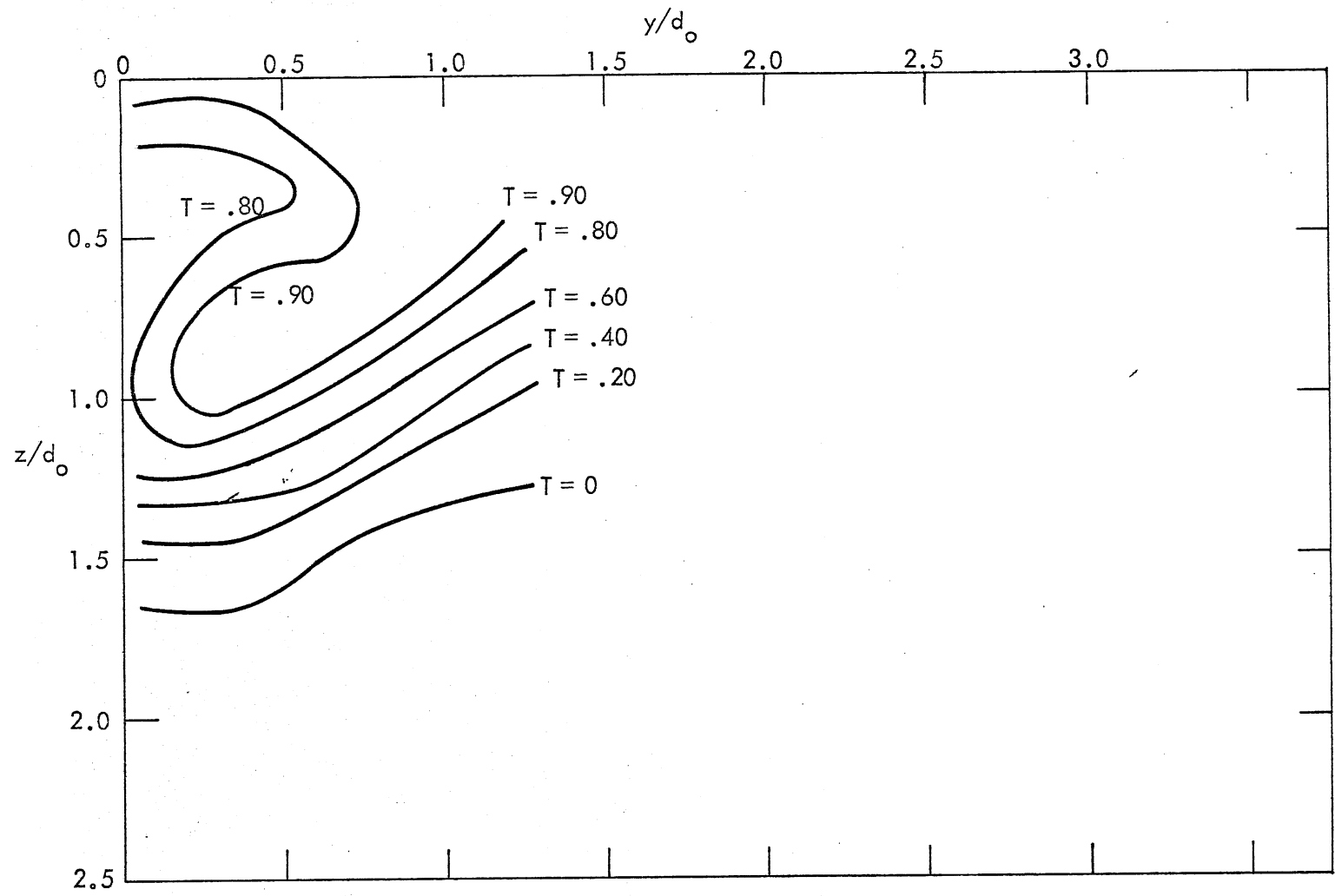


Fig. A-6 - Vertical temperature fluctuation profile along jet axis - $A = 2.4$, $F_0 = 15.8$, $R = 0$



123

Fig. A-7 - Vertical temperature profile perpendicular to jet axis - $A = 2.4$, $F_0 = 2.2$, $R = 0$,
 $x/d_0 = 1.8$

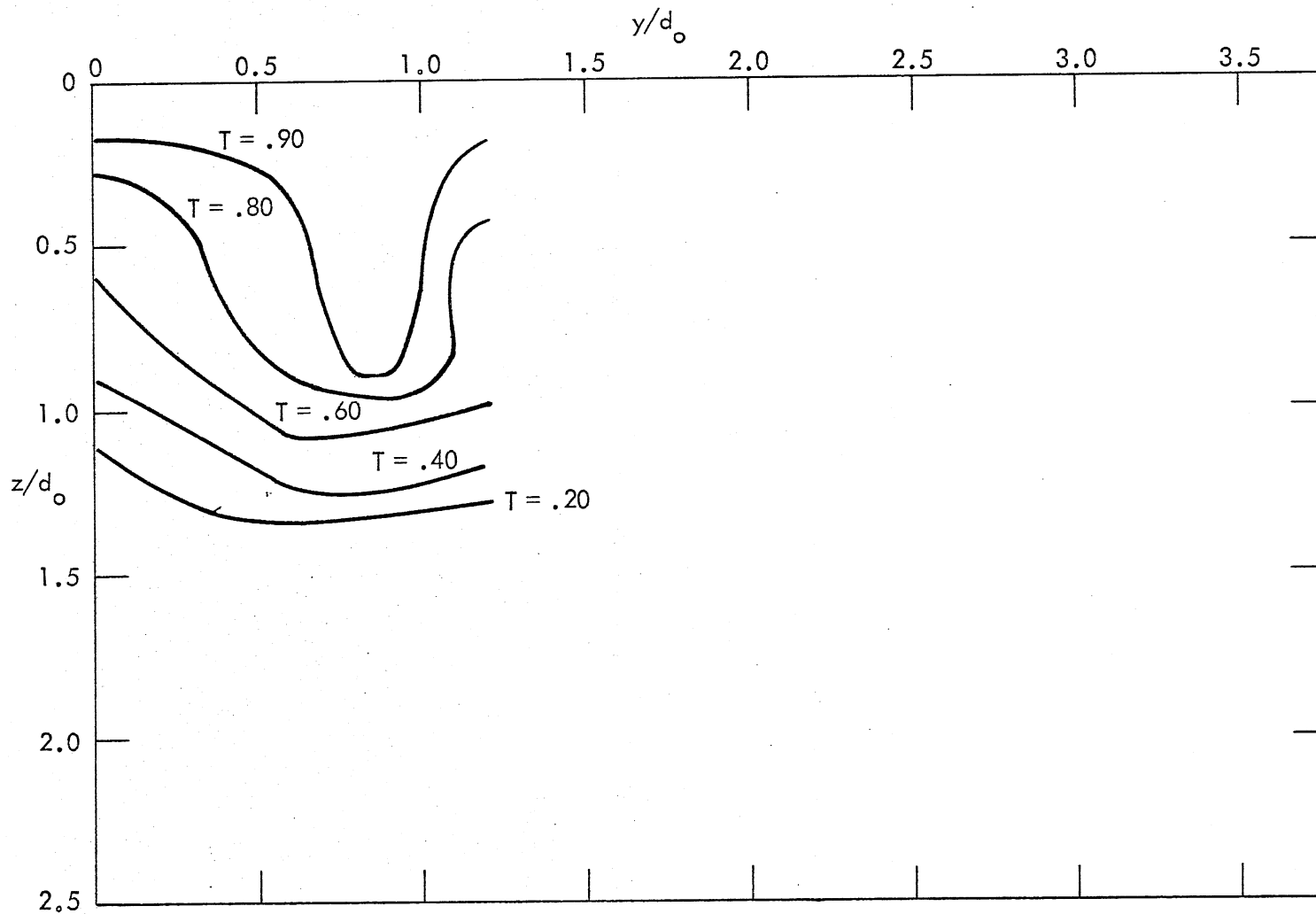


Fig. A-8 - Vertical temperature profile perpendicular to jet axis - $A = 2.4$, $F_0 = 3.85$, $R = 0$,
 $x/d_0 = 1.8$

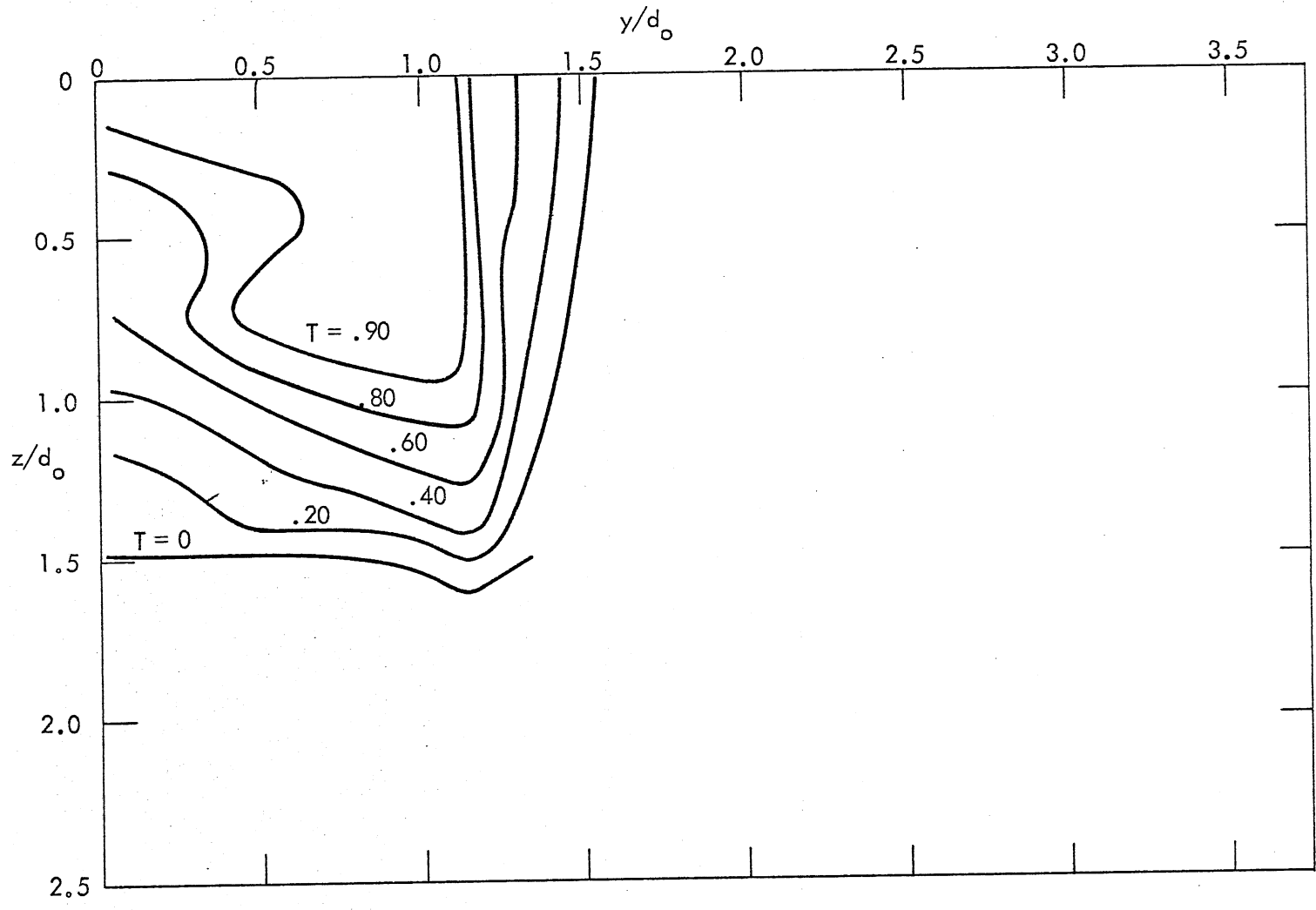


Fig. A-9 - Vertical temperature profile perpendicular to jet axis - $A = 2.4$, $F_0 = 15.8$, $R = 0$, $x/d_0 = 1.8$

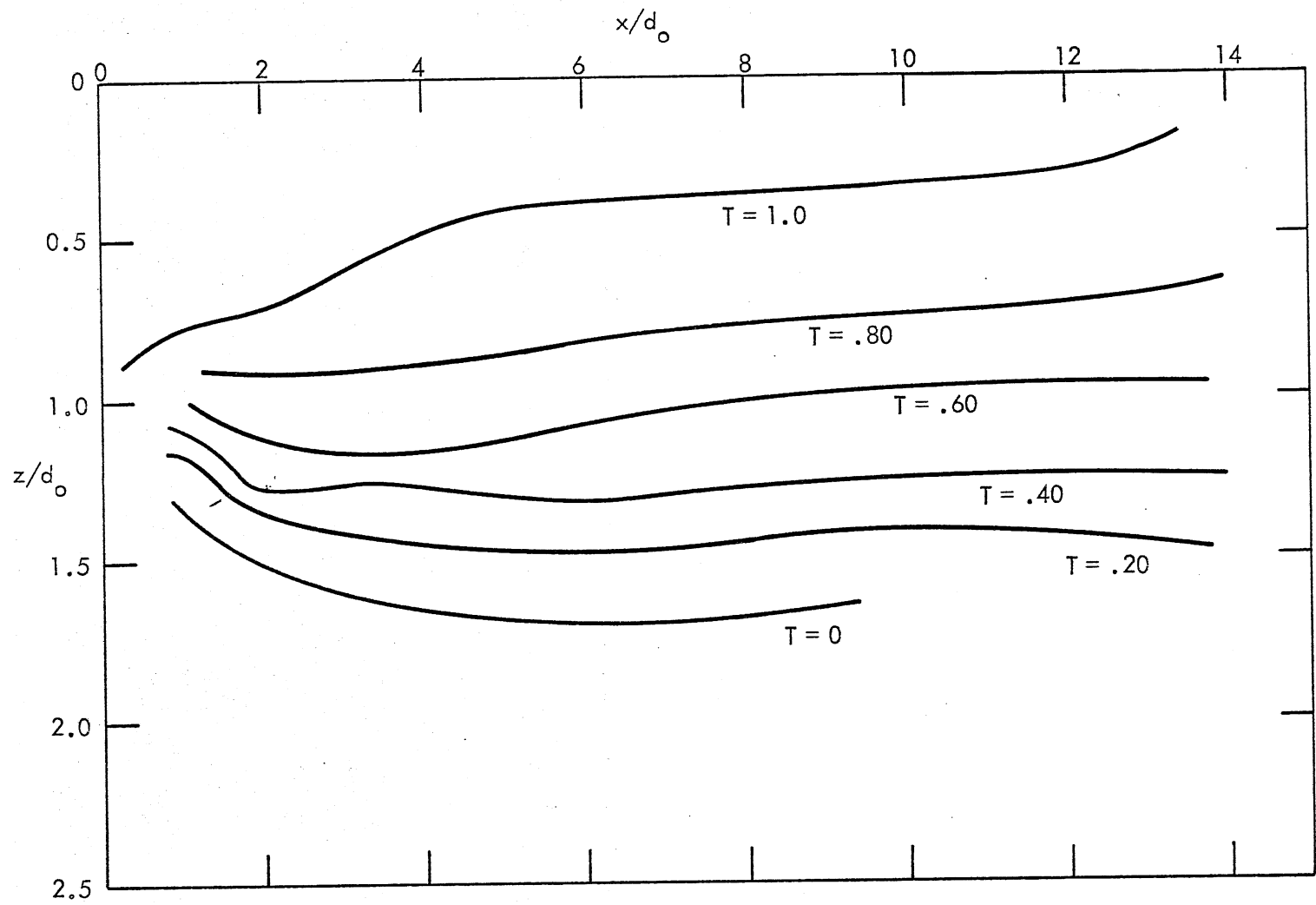


Fig. A-10 - Vertical temperature profile along jet axis - $A = 9.6$, $F_0 = 2.15$, $R = 0$

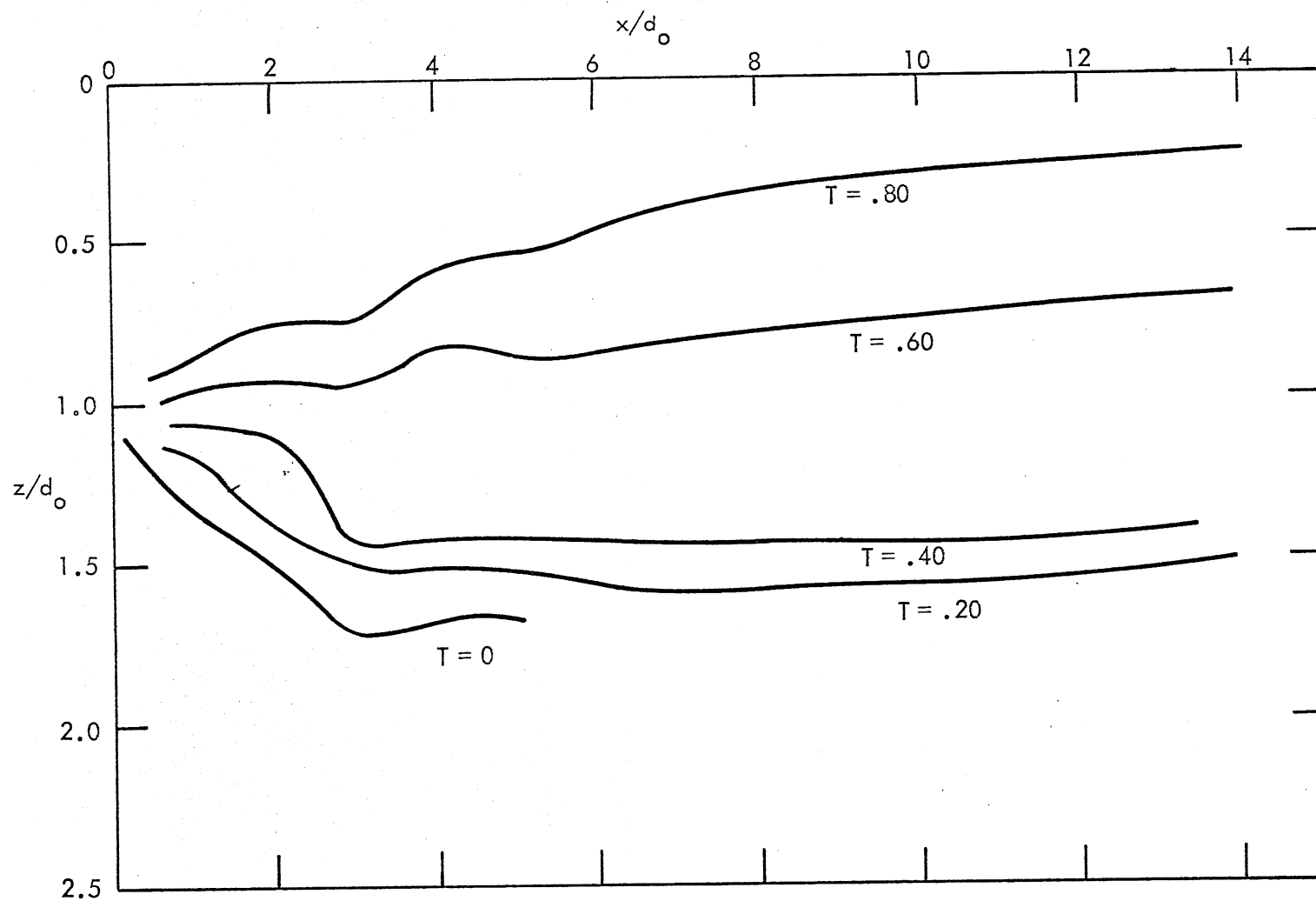


Fig. A-11 - Vertical temperature profile along jet axis - $A = 9.6$, $F_0 = 4.1$, $R = 0$

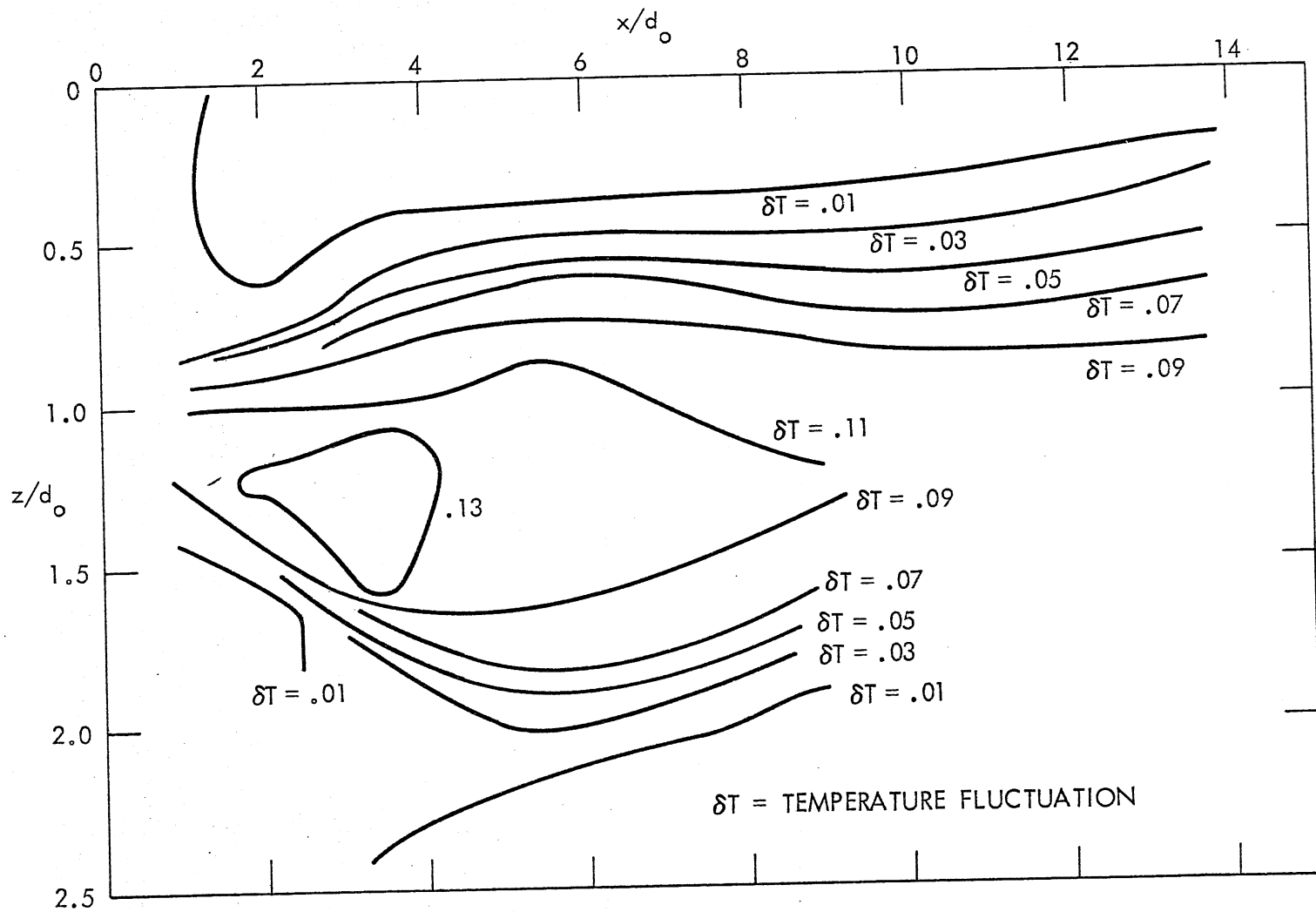


Fig. A-12 - Vertical temperature fluctuation profile along jet axis - $A = 9.6$, $F_0 = 2.15$,
 $R = 0$

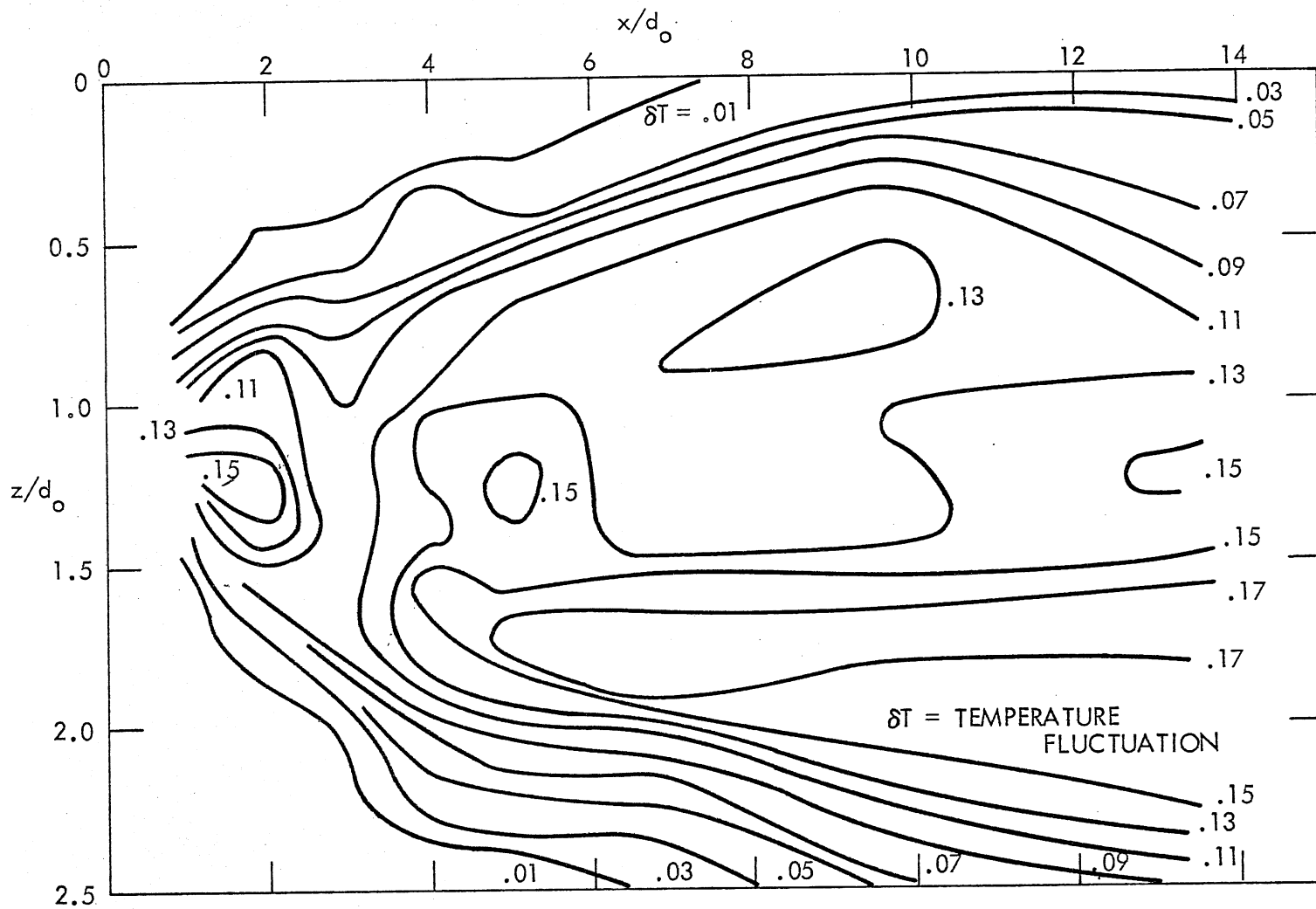


Fig. A-13 - Vertical temperature fluctuation profile along jet axis - $A = 9.6$, $F_0 = 4.1$,
 $R = 0$

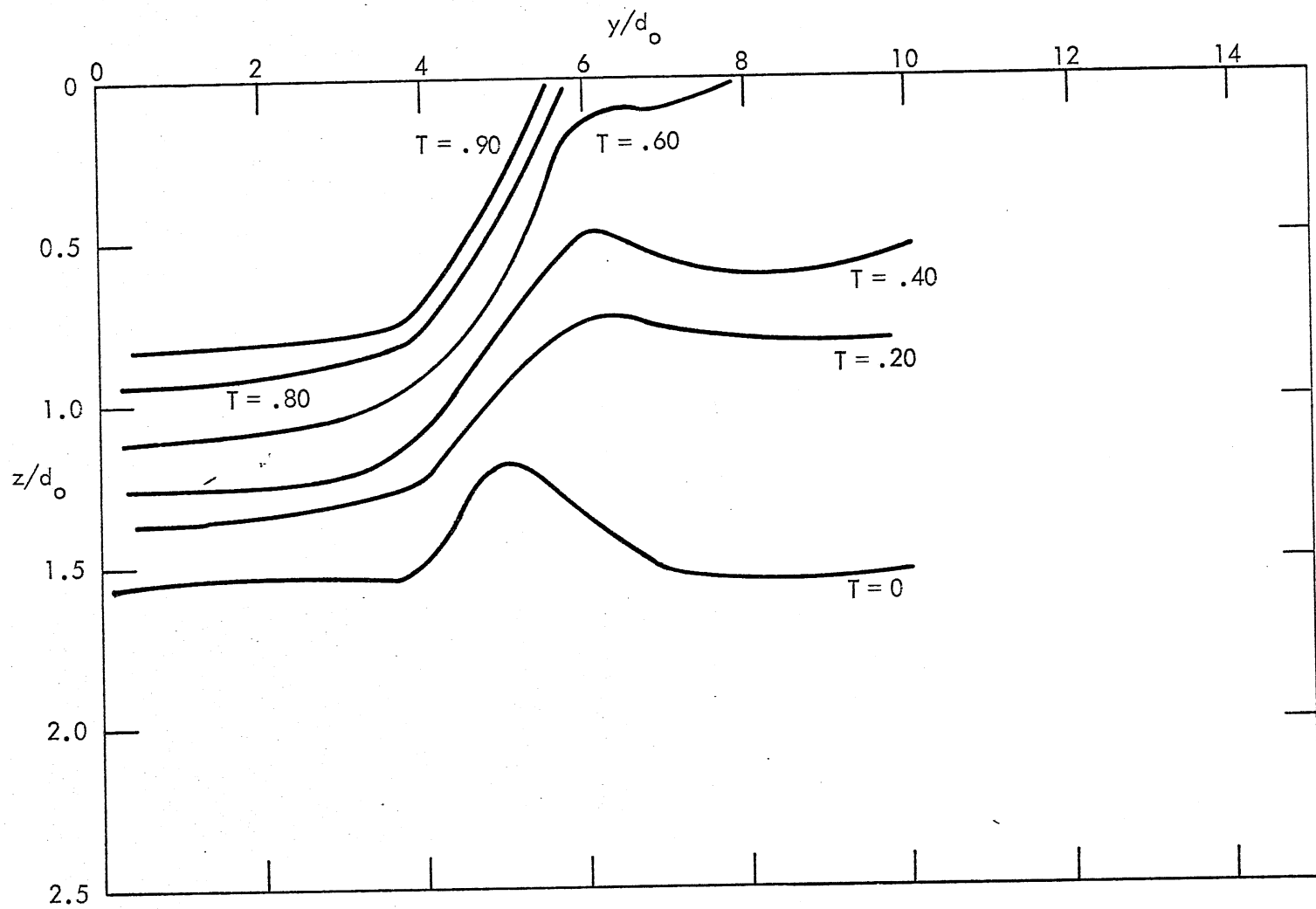
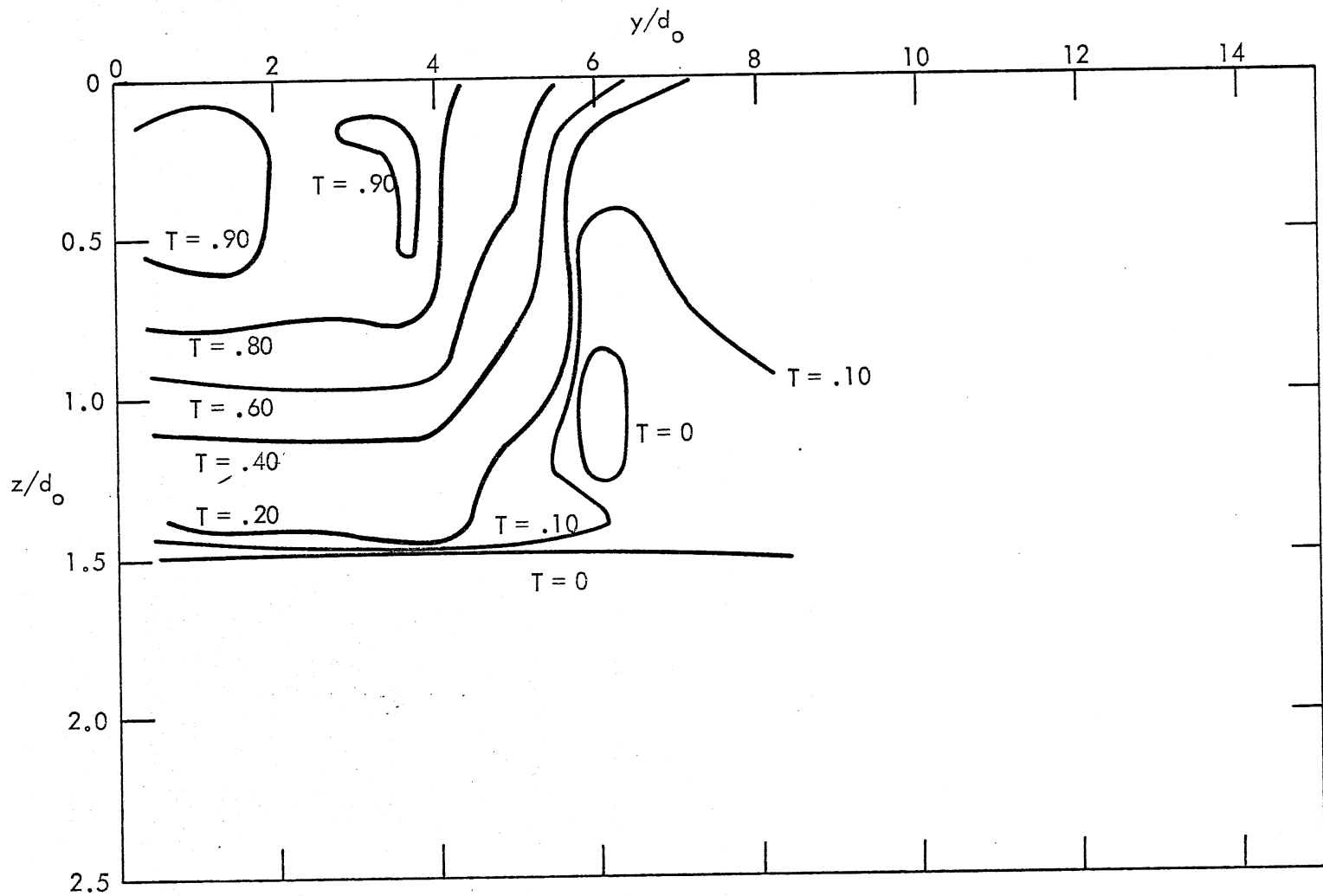


Fig. A-14 - Vertical temperature profile perpendicular to jet axis - $A = 9.6$, $F_o = 2.15$, $R = 0$,
 $x/d_o = 1.9$



131

Fig. A-15 - Vertical temperature profile perpendicular to jet axis - $A = 9.6$, $F_0 = 4.1$,
 $R = 0$, $x/d_0 = 1.9$

Appendix B

ISOTHERMS $T = \text{constant}$ and $\delta T = \text{constant}$
AND ISOVELS $V = \text{constant}$
IN VERTICAL AND HORIZONTAL SECTIONS,
 $A = 2.4$, $R = 0.41$

FIGURES -- APPENDIX B

<u>No.</u>	<u>Page</u>
B-1	134
Vertical Temperature Profile Perpendicular to Jet Axis - A = 2.4, $F_o = 3.35$, $R = 0.41$, $s/d_o = 4.1$	
B-2	135
Vertical Temperature Profile Perpendicular to Jet Axis - A = 2.4, $F_o = 3.35$, $R = 0.41$, $s/d_o = 8.5$	
B-3	136
Vertical Temperature Profile Perpendicular to Jet Axis - A = 2.4, $F_o = 3.35$, $R = 0.41$, $s/d_o = 13.3$	
B-4	137
Vertical Temperature Fluctuation Profile Perpendicular to Jet Axis - A = 2.4, $F_o = 3.35$, $R = 0.41$, $s/d_o = 4.1$	
B-5	138
Vertical Temperature Fluctuation Profile Perpendicular to Jet Axis - A = 2.4, $F_o = 3.35$, $R = 0.41$, $s/d_o = 8.5$	
B-6	139
Vertical Temperature Fluctuation Profile Perpendicular to Jet Axis - A = 2.4, $F_o = 3.35$, $R = 0.41$, $s/d_o = 13.3$	
B-7	140
Temperature and Velocity Profiles at Water Surface - A = 2.4, $F_o = 3.35$, $R = 0.41$	
B-8	141
Temperature Fluctuation Profile at Water Surface - A = 2.4, $F_o = 3.35$, $R = 0.41$	

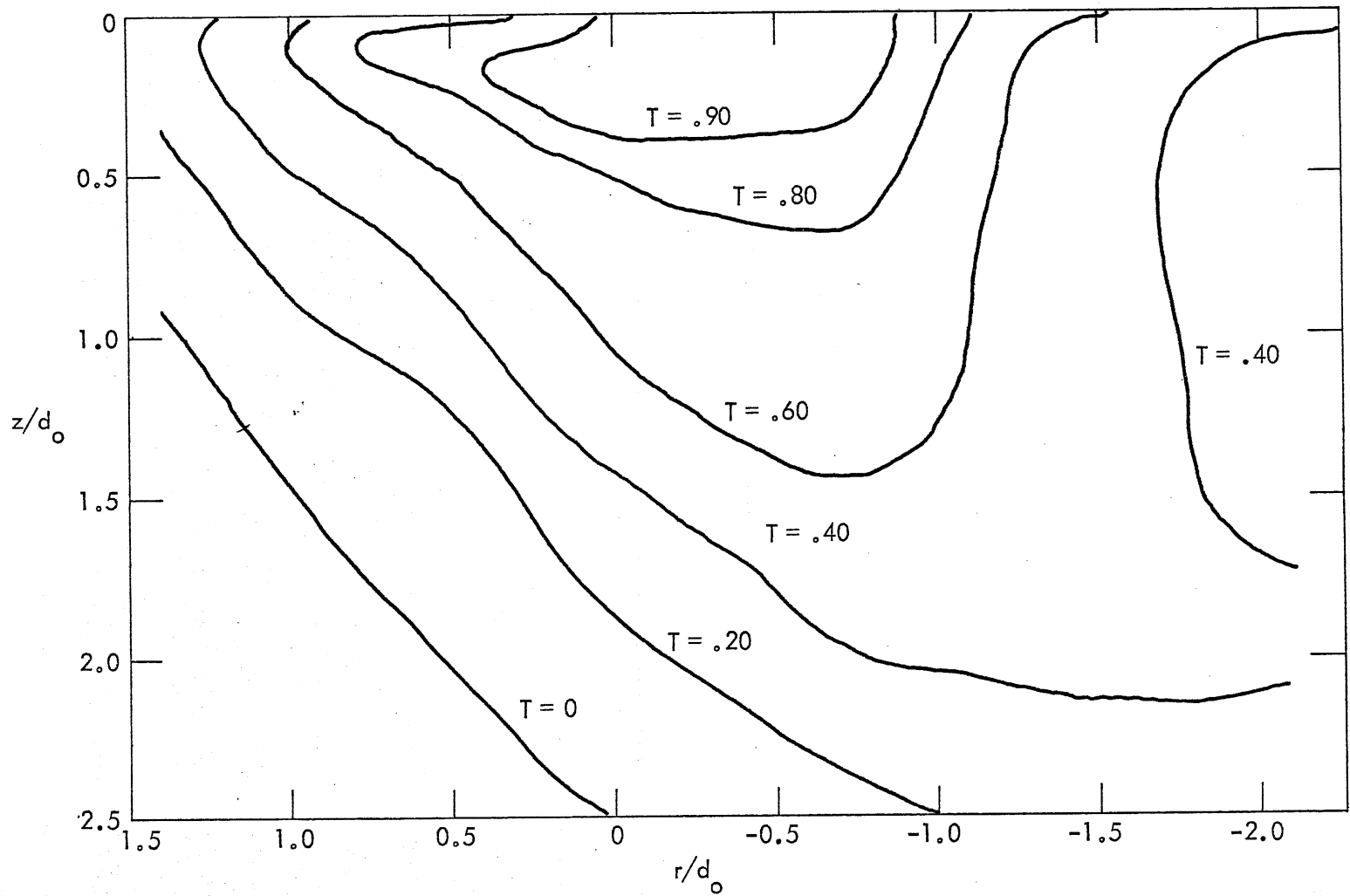


Fig. B-1 - Vertical temperature profile perpendicular to jet axis - $A = 2.4$, $F_o = 3.35$,
 $R = 0.41$, $s/d_o = 4.1$

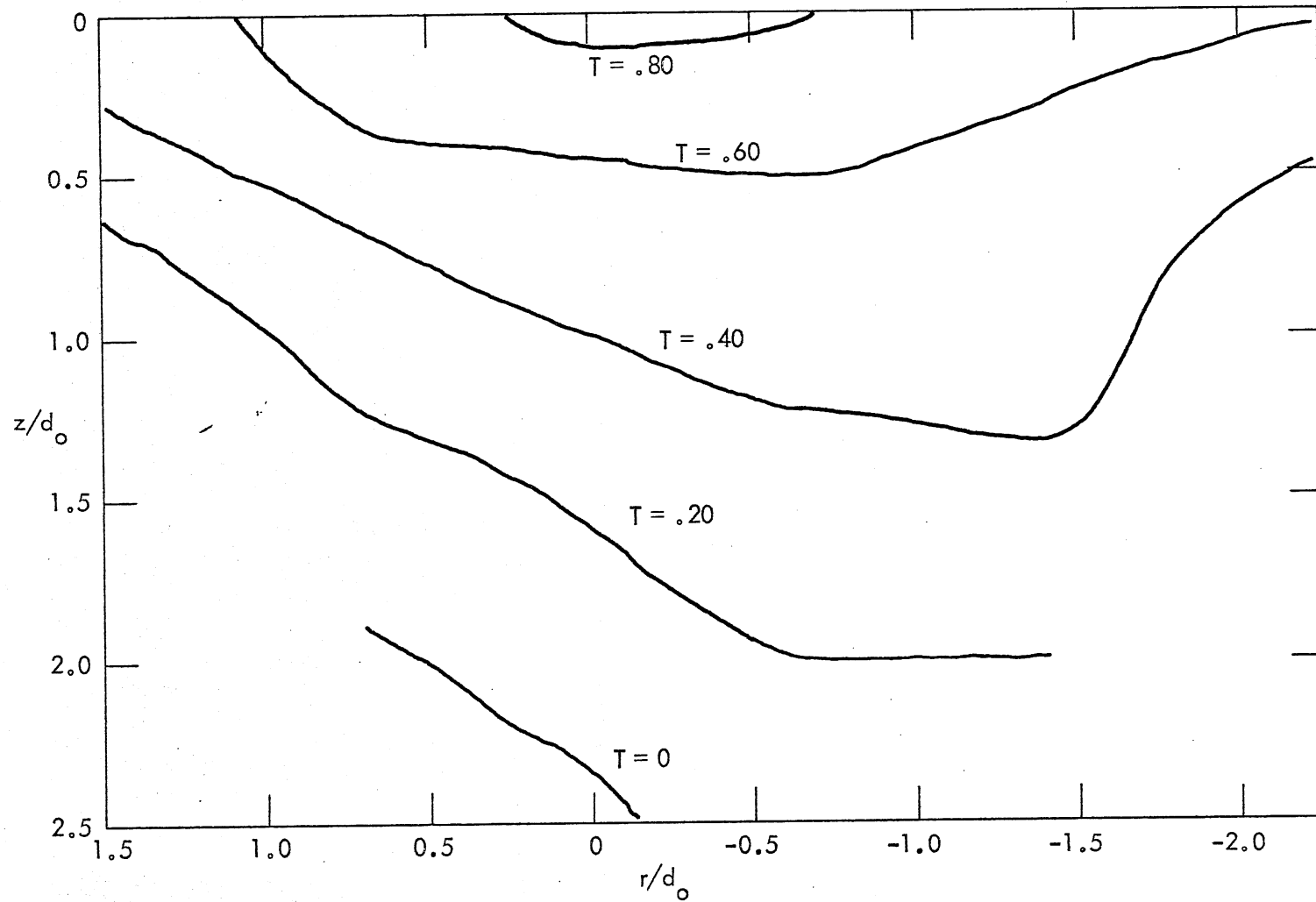


Fig. B-2 - Vertical temperature profile perpendicular to jet axis - $A = 2.4$, $F_0 = 3.35$,
 $R = 0.41$, $s/d_0 = 8.5$

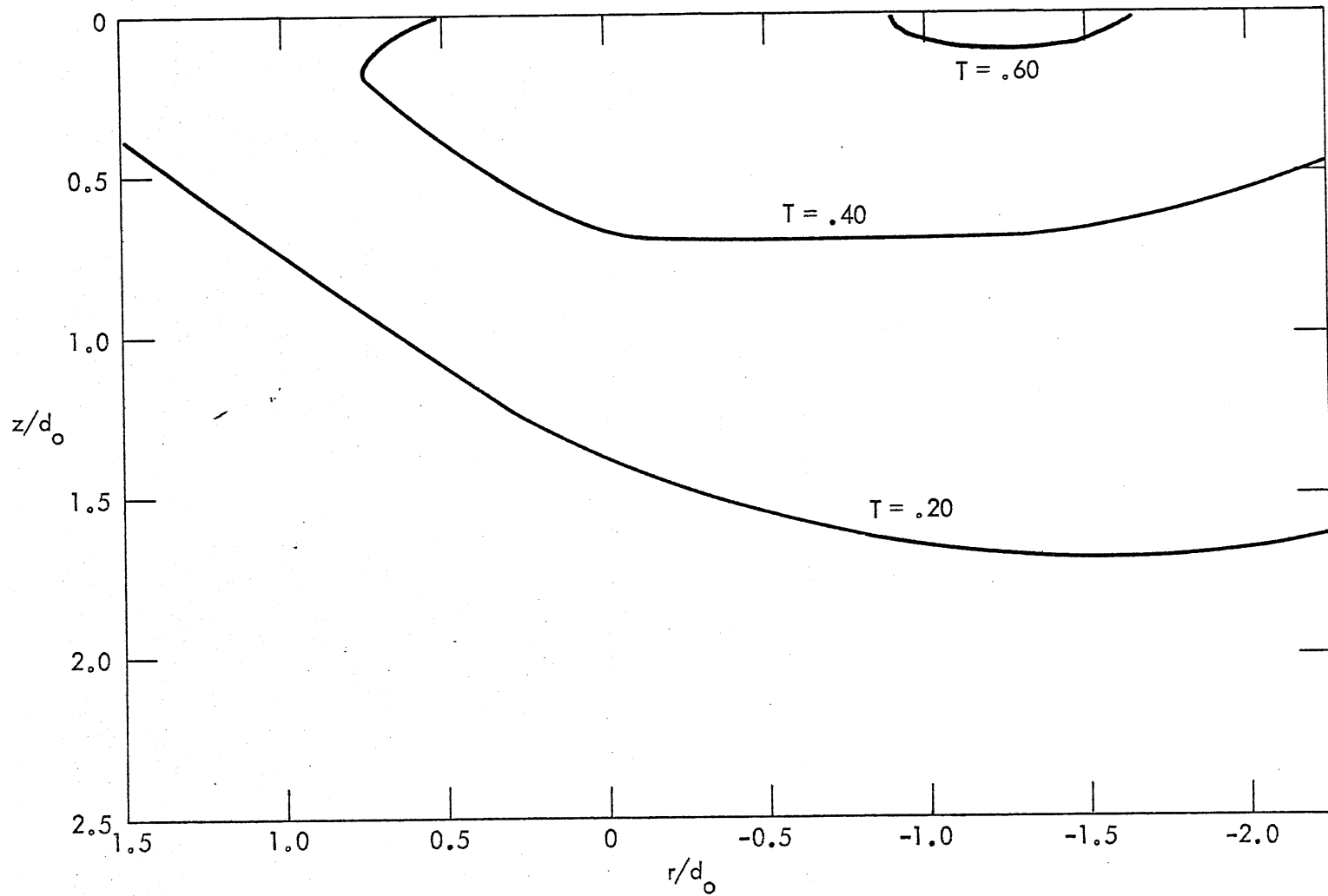


Fig. B-3 - Vertical temperature profile perpendicular to jet axis - $A = 2.4$, $F_0 = 3.35$,
 $R = 0.41$, $s/d_0 = 13.3$

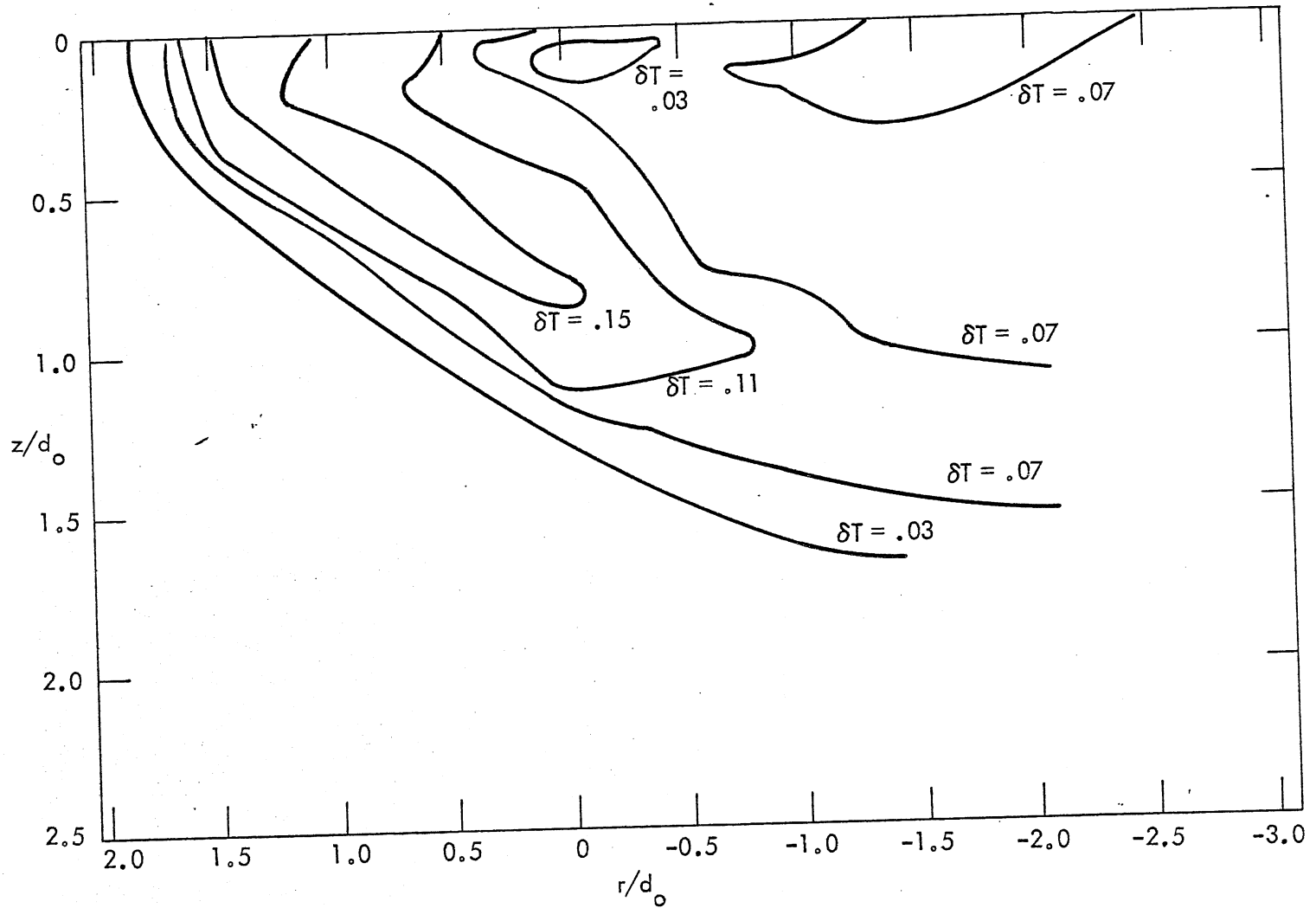


Fig. B-4 - Vertical temperature fluctuation profile perpendicular to jet axis - $A = 2.4$,
 $F_o = 3.35$, $R = 0.41$, $s/d_o = 4.1$

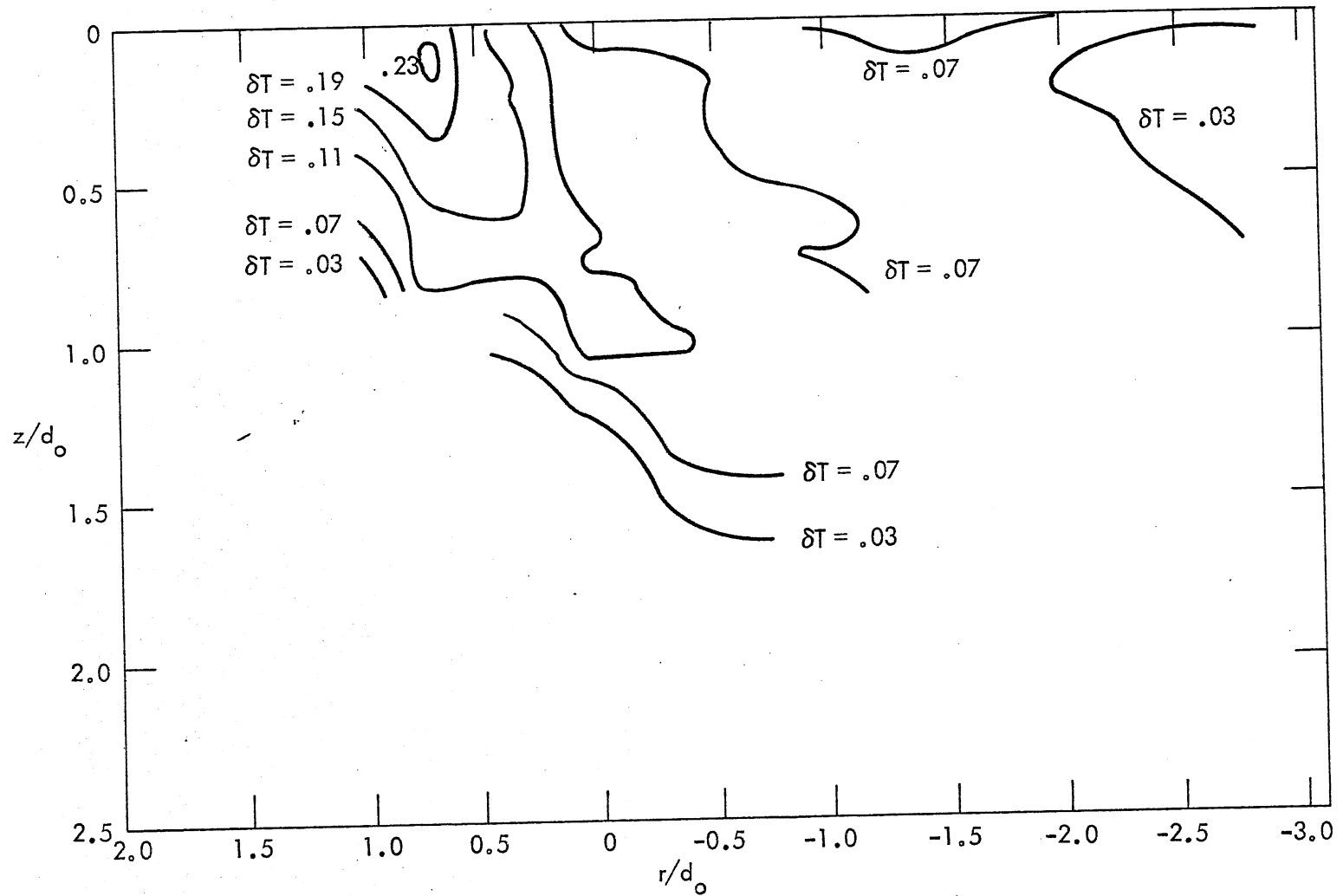


Fig. B-5 - Vertical temperature fluctuation profile perpendicular to jet axis - $A = 2.4$,
 $F_o = 3.35$, $R = 0.41$, $s/d_o = 8.5$

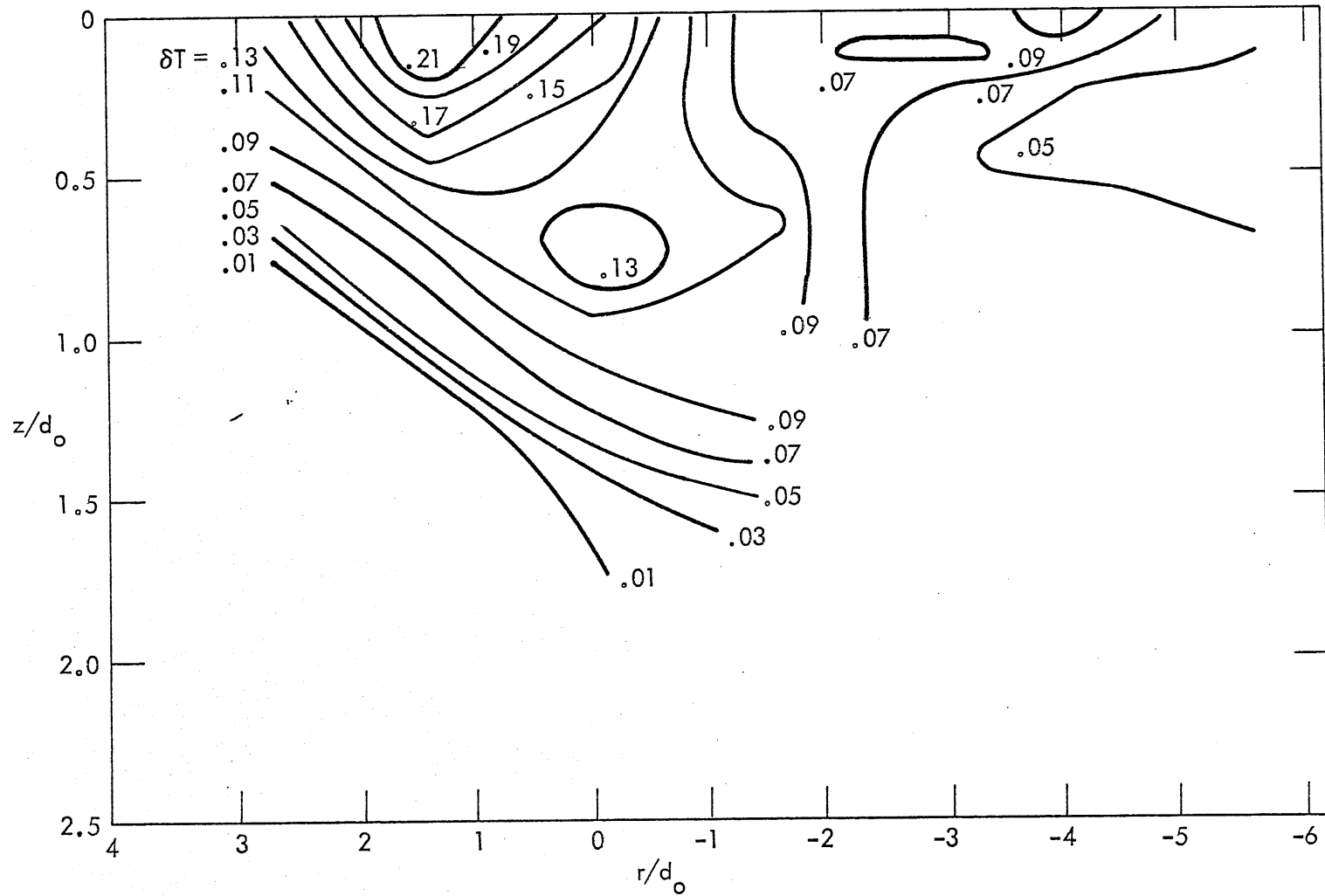


Fig. B-6 - Vertical temperature fluctuation profile perpendicular to jet axis - $A = 2.4$,
 $F_0 = 3.35$, $R = 0.41$, $s/d_0 = 13.3$

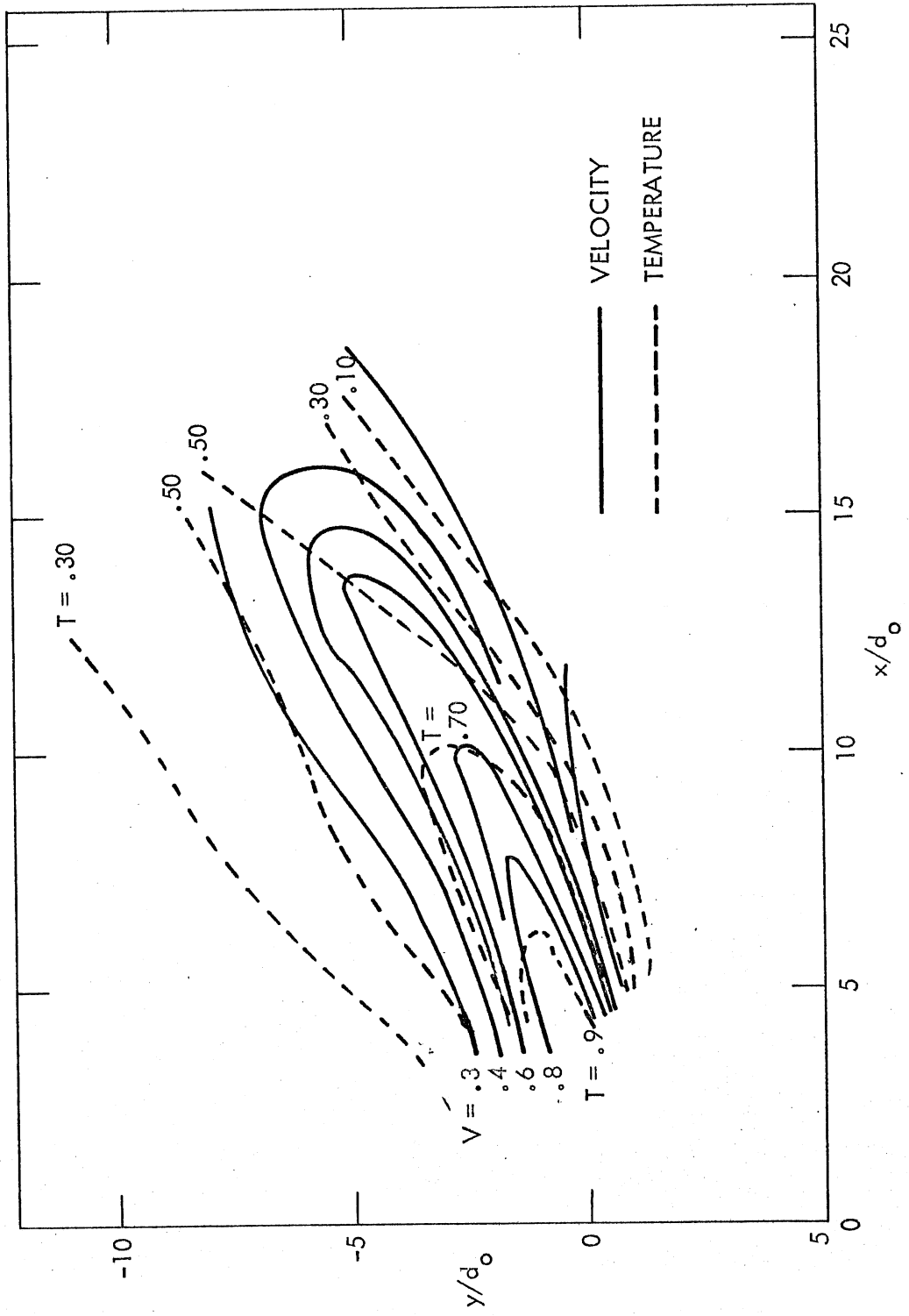


Fig. B-7 - Temperature and velocity profiles at water surface - $A = 2.4$, $F_o = 3.35$, $R = 0.41$

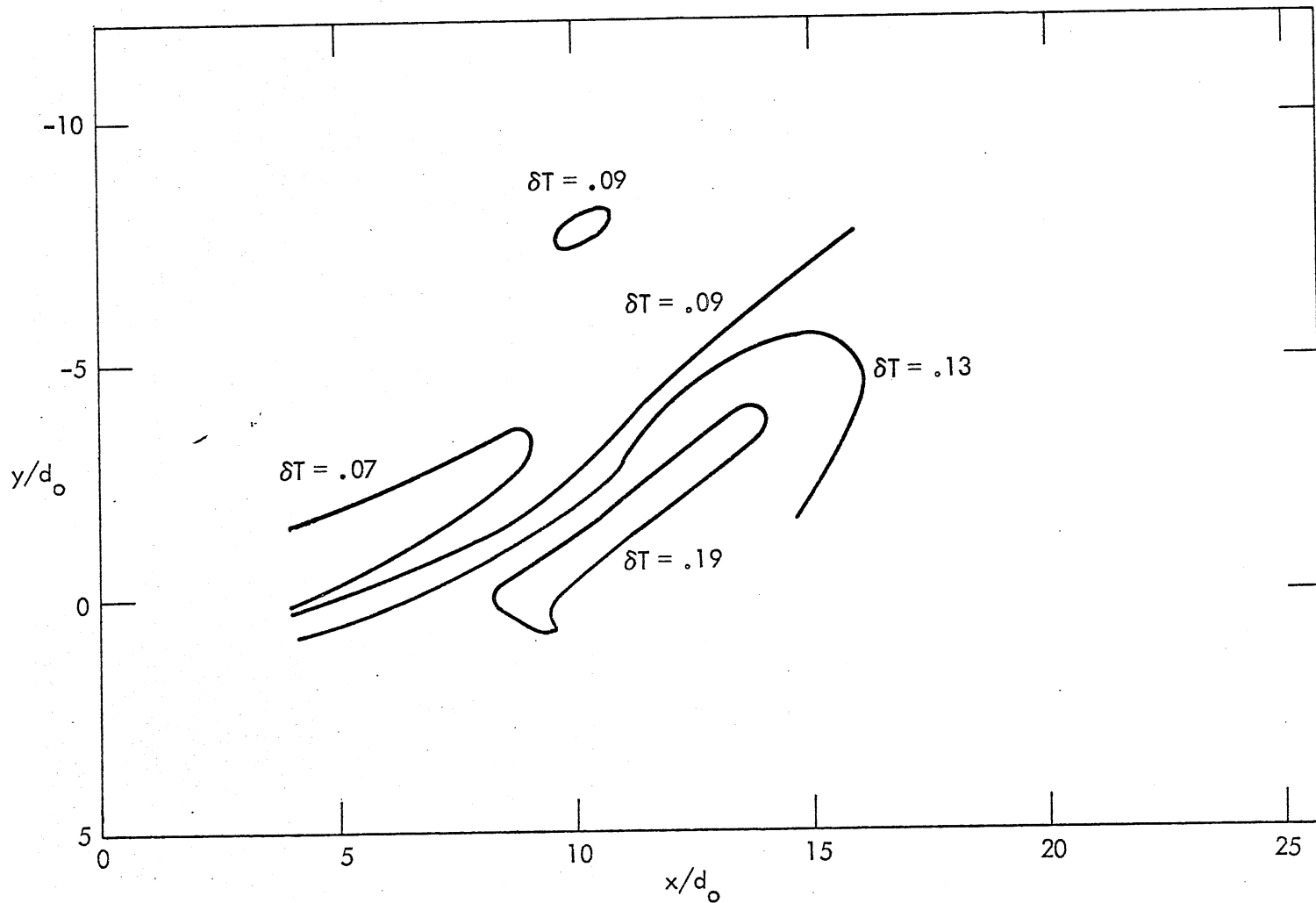


Fig. B-8 - Temperature fluctuation profile at water surface - $A = 2.4$, $F_o = 3.35$,
 $R = 0.41$

SELECTED WATER RESOURCES ABSTRACTS INPUT TRANSACTION FORM		1. Report No.	2.	3. Accession No. W
4. Title: FLOW ESTABLISHMENT AND INITIAL ENTRAINMENT OF HEATED WATER SURFACE JETS				5. January 1975 6. 8.
7. Author(s): Stefan, H.; Bergstedt, L.; Mroska, E.				10. Project No.
9. Organization: St. Anthony Falls Hydraulic Laboratory University of Minnesota Minneapolis, Minnesota				11. Contract/Grant No. R 800 435
12. Sponsoring Organization: Environmental Protection Agency				13. Type of Report and Period Covered Final
15. Supplementary Notes: Environmental Protection Agency Report Number				
16. Abstract: Mathematical modeling of the zone of flow (re-)establishment (ZFE) of heated water surface jets has been found to be difficult because of the complex dependence on outlet geometry, discharge velocity, buoyancy, and ambient currents. Laboratory experiments have therefore been conducted to provide more observations and data on flow patterns, temperatures, and flow velocities in the ZFE and some distance beyond. From this information, relationships giving the length x_0 of the ZFE, the volumetric flow rates $Q(x)$ versus distance, and the initial spreading angle ϕ_0 have been derived. The independent variables were outlet aspect ratio A , outlet densimetric Froude number, and cross-flow ratio R . The relationships provided can be used to make more accurate temperature predictions in the immediate vicinity of a heated water surface channel.				
17a. Descriptors: Thermal pollution, Discharge (water), Water quality, Water quality control, Water pollution, Water pollution control, Outfalls, Experimental data, Flow establishment, Mixing zone, Dilution, Heated water, Jet flow, Buoyant jet				
17b. Identifiers: Thermal plume, Surface discharge, Heated water jet				
18. Availability:	19. Sec. Class (Report)	21. No. of pages: 142	Send to:	
	20. Sec. Class (page)	22. Price:	WRSIC USDI Washington, D.C. 20240	
Abstractor: Dr. H. Stefan			Institution: Univ. of Minnesota, SAFHL	